ISSN 1562 - 2703

INTERNATIONAL JOURNAL AUTOMATION AUSTRIA

HEFT 2 Jahrgang 18 (2010)

INHALT *Seite*

BERICHTE

SCOPE

"International Journal Automation Austria" (IJAA) publishes top quality, peer reviewed papers in all areas of automatic control concerning continuous and discrete processes and production systems.

Only original papers will be considered. No paper published previously in another journal, transaction or book will be accepted. Material published in workshops or symposia proceedings will be considered. In such a case the author is responsible for obtaining the necessary copyright releases. In all cases, the author must obtain the necessary copyright releases before preparing a submission. Papers are solicited in both theory and applications

Before preparing submissions, please visit our instructions to authors (see back cover) or web page.

International Journal Automation Austria also is the official executive authority for publications of IFAC-Beirat Österreich.

Imprint: Propagation of Automatic Control in Theory and Practice.

Frequency: Aperiodically, usually twice a year.
Publisher: IFAC-Beirat Österreich, Peter Kopacek, Alexander Weinmann
Editors in Chief: Alexander Weinmann, Peter Kopacek

Address: 1) Institut für Automatisierungs- und Regelungstechnik (E376), TU Wien,
A-1040 Wien, Gußhausstrasse 27-29, Austria
Phone: +43 1 58801 37677, FAX: +43 1 58801 37699
email: danzinger@acin.tuwien.ac.at
Homepage: http://www.acin.tuwien.ac.at/publikationen/ijaa/

2) Intelligente Handhabungs- und Robotertechnik (E325/A6), TU-Wien,
A-1040 Wien, Favoritenstrasse 9-11, Austria
email: e318@ihrt.tuwien.ac.at

Layout: Rainer Danzinger
Printing: Kopierzentrum der TU Wien

Improved Kinematics Calibration of Industrial Robots by Neural Networks

Giovanni Legnani, Monica Tiboni

Department of Mechanical and Industrial Engineering, Brixia University, Italy
E-mail: {giovanni.legnani, monica.tiboni}@ing.unibs.it
URL: http://robotics.ing.unibs.it

Received October 15, 2009

Abstract. The paper presents a preliminary study on the feasibility of a Neural Networks based methodology for the calibration of Industrial Manipulators to improve their accuracy. A Neural Network is used to predict the pose inaccuracy due to general sources of error in the robot (e.g. geometrical inaccuracy, load deflection, stiffness and backlash of the mechanical members, etc...). The network is trained comparing the ideal model of the robot with measures of the actual poses reached by the robot. A back-propagation learning algorithm is applied. The Neural Network output can be used by the robot controller to compensate for the errors in the pose. The proposed calibration technique appears extremely simple. It does not need any information on the pose errors nature, but only the ideal robot kinematics and a set of experimental pose measures. Different schemes of calibration procedures are applied to a simulated SCARA robot and to a Stewart Platform and compared, in order to select the most suitable. Results of the simulations are presented and discussed.

Keywords. robot calibration, Neural Network, SCARA robot, Stewart Platform, compensation

1 Introduction

1.1 Kinematics calibration

A robot is a mechanical system in which constructive tolerances (geometrical inaccuracy), load deformations, stiffness and backlash of the mechanical members, etc..., cooperate to create inaccuracy in the gripper pose (position and orientation).

Industrial robots are generally quite repetitive while their accuracy is generally worse. Calibration is a methodology to improve the robot accuracy without mechanical means working only on its controller. Computer simulations and experimental verifications show that very often a proper calibration can improve the robot accuracy up to a value close to the robot repeatability [Mooring et al.(1991), Trevelyan et al.(1996)]. Calibration is possible whenever a procedure to predict the robot error can be established. Many research activities have been carried on this subject, nevertheless the search for a simple and effective calibration procedure for on-field applications is still open.

A procedure to improve the robot accuracy (which for not calibrated industrial robots is sometimes up to some millimeters) consists of two main parts:

1. the measurement of the gripper position and orientation error for a predefined set of gripper poses in the workspace;
2. the development of a mathematical technique to predict and to compensate for the measured errors.

These two problems can be considered quite independent. The authors attention in this work is focused on the second aspect: supposing given a data set of gripper pose measures, a new method to predict the gripper pose inaccuracy is proposed. This will make possible a compensation [Faglia et al. (1993), Legnani et al.(1996), Trevelyan et al.(1996)].

Classical methods are based on the well-known parametric approach and consist in two phases:

- the definition of a model of the robot considering some of the possible causes of inaccuracy (defining a priori the relating complexity);
- the identification of the unknown value of the parameters of the model.

Usually the models consider only geometrical inaccuracy. The complexity of the model and the high number of parameters involved often prevents considering other phenomena, such as the deflection of the elements, the backlash in the joints, etc.... This is the principal limit of the parametric approach.

1.2 The proposed methodology

To overlap the limits of parametric calibration we try to find a simple method, able to predict the pose errors in a way completely independent of the nature of their causes and without requiring any complex model [Tiboni et al. (2003), Fazenda et al. (2006)].

A Neural Network (NN) appeares a good instrument to achieve this goal. A robot can be considered a system that performs a transformation of the input (the joint angles) in a corresponding set of the gripper coordinates in the robot workspace (the output). The input/output transfer function in a real robot may be quite different from the theoretical one. Moreover, theory assures that a proper feed-forward Neural Network, with a back-propagation training technique is able to approximate any kind of mathematical transformation [Haykin (1999)]. The basic idea is to use a Neural Network to learn the input/output direct and inverse transfer function of the *real robot*.

This preliminary study has the aim to verify the effectiveness of this methodology comparing a number of different computational schemes involving a Neural Network and an ideal model of the robot kinematics. The methodology is applied to different serial and parallel manipulators. The network is trained and tested using simulated pose measures generated by an external program implementing the kinematics of a robot with geometrical errors, plus joint backlash and compliance. The results obtained by the different schemes are compared taking into account:

a. the accuracy in the prediction of the real pose;

b. the difficulty in the NN parameter tuning;

c. the capacity of generalization;

d. the immunity to the noise included in the measures.

Many different calibration schemes have been tested. Two of them, which will be more deeply analyzed in the paper, produced very good results. They are able to improve the accuracy up to a value comparable with the measuring error and the robot repeatability.

To have the possibility to examine different schemes with different variants, a suitable simulation procedure was adopted.

Different calibration scheme are initially compared on a simplified SCARA robot. As a second step, the more promising schemes are applied to a parallel manipulator and to a full model SCARA manipulator for their final validation.

2 The SCARA robot used for the preliminary tests

Being the aim of the first step of the research just a feasibility analysis, we consider a very simple SCARA robot. In spite of its simplicity, this robot is characterized by the same problems of more complex robots, as singularities, multiple solutions, etc.

The robot considered is formed by two links which move the gripper in the x-y plane by means of two rotoidal joints; the end-effector vertical translation is not considered. Let us denote with α and β the two joint variables, with l_1 and l_2 the link lengths, with x and y the end-effector cartesian coordinates (Fig. 1).

The nominal direct kinematic problem for this robot is solved by equations 1, the inverse one by eq. 2.

$$\begin{cases} x = l_1 \cos\alpha + l_2 \cos(\alpha+\beta) \\ y = l_1 \sin\alpha + l_2 \sin(\alpha+\beta) \end{cases} \tag{1}$$

$$\begin{cases} \alpha = \pm \arccos(\frac{x^2+y^2-l_1^2-l_2^2}{2l_1 l_2}) \\ \beta = atan2(y,x) - atan2(l_2 \sin\beta, l_1 + l_2 \cos\beta) \end{cases} \tag{2}$$

By introducing geometrical inaccuracy the direct kinematic is solved by eq. 3, where the "prefix" δ denotes small unknown errors, while Δx,Δy represent the gripper error that can be measured for given values of α and β. The errors can be constant, random or depending on the external loads. The nature of the errors is better described in sect. 3.2.

$$\begin{cases} x_r = x + \Delta x = & (l_1+\delta l_1)\cos(\alpha+\delta\alpha)+ \\ & +(l_2+\delta l_2)\cos(\alpha+\delta\alpha+\beta+\delta\beta) \\ y_r = y + \Delta y = & (l_1+\delta l_1)\sin(\alpha+\delta\alpha)+ \\ & +(l_2+\delta l_2)\sin(\alpha+\delta\alpha+\beta+\delta\beta) \end{cases} \tag{3}$$

3 Calibration methodology

3.1 The Neural Network

In a problem of system identification (nonlinear input-output mapping) a right choice for a NN is a multilayer feed-forward network, trained in a supervised manner with the back-propagation learning technique [Haykin (1999)].

The chosen network contains just one layer of hidden neurons (Fig. 2) with sigmoidal activation functions. Linear activation functions are used for the output neurones. In accordance with the *"universal approximation theorem"*, this NN can approximate an arbitrary continuous function [Haykin (1999)]. Moreover, this choice is the optimum in the sense of easy implementation, learning time and generalization.

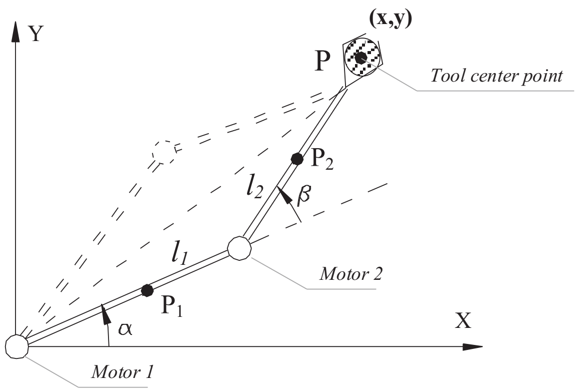

Figure 1: The SCARA robot joint variables.

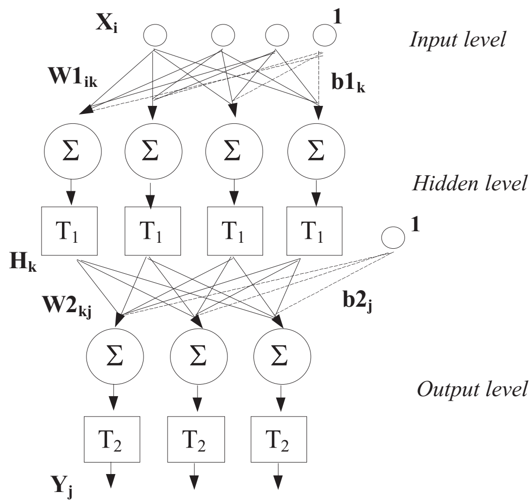

Figure 2: The feed-forward network used.

3.2 The tested calibration schemes

The authors attention has been focused first on the direct kinematic calibration and then on the inverse one.

For the direct kinematics, the idea is to create a neuro-kinematic (NK) model of the real robot (Fig. 3), merging a model of the ideal robot with a NN describing the manipulator errors. Different schemes have been analyzed (Fig. 5) to select the more effective one.

In Fig. 3 we denoted as $Q_{th} = [\alpha;\beta]^t$ the values of the joint variables measured by the joint transducers, while $S_{th} = [x;y]^t$ and $S_{re} = [x_r;y_r]^t$ are the theoretical and real gripper pose.

The NN is trained in order to reduce the quantity $E = \|S_{re} - S_{NK}\|$, which represents the error in the gripper pose prediction, where $\|\cdot\|$ is the Euclidean norm.

The schemes of NK model in Fig. 5 enable the prediction of the actual gripper pose S_{re}, knowing the joint rotations Q_{th} (direct kinematics calibration).

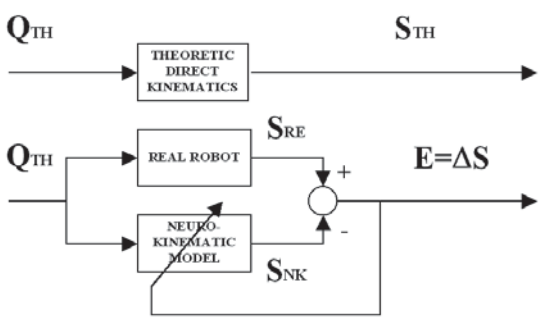

Figure 3: The direct kinematics calibration model.

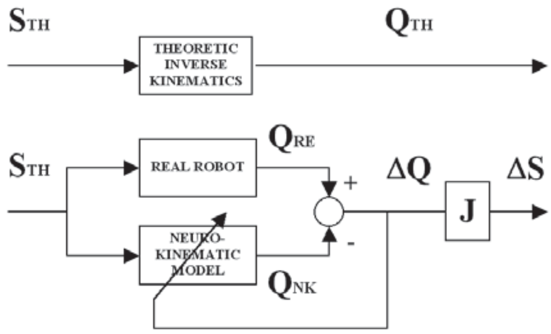

Figure 4: The inverse kinematics calibration model.

For the inverse kinematics calibration is required to predict the joint rotation Q_{re} that bring the gripper of an actual robot in a desired pose Sth. A NK inverse model has to be trained (Fig. 4); different possible schemes are shown in Fig. 6.

In order to make results comparable with those of the direct kinematics, instead of the joint error $E = ||Q_{re} - Q_{NK}||$, as performance index was used the equivalent pose error $E = ||\Delta S|| = ||J\Delta Q||$, where J is the jacobian matrix and $\Delta Q = Q_{re} - Q_{th}$

4 Comparison of the different Neuro-Kinematics schemes

4.1 Angular coordinates

The first simulations highlighted a problem related to large variations of the angles.
The robot behaviour depends on the sine and the cosine of rotation angles rather than on the angles themselves. And so a rotation of α or $\alpha \pm 2k\pi$ produces the same effect. However, since the NN activation functions are continuous and not periodical, if an angle is used as input to a NN, the output value would be different when the input is α or $\alpha \pm 2k\pi$. This fact makes the NN behaviour unreliable for large rotation of the joint angles and for the representation of the gripper attitude. After several tests, it was decided to replace each angular input of the NN with two inputs representing the sine and the cosine of the angles, that means that the joint vector $Q = [\alpha\ \beta]$ (trigonometric form) was defined as $Q = [sin\alpha\ cos\alpha\ sin\beta\ cos\beta]$ (angular form).

A second aspect of this problem was the identification of the best way to add joint rotations in the schemes like 2,3,4 and 6 of Fig. 5 and Fig. 6. This operation can be done in three different ways as described in Tab. 1. In the preliminary tests, all the considered NN performed better using the second type of angular addition.

Generalizing previous observations, every time a coordinates set X ($X = Q$ or $X = S$) contains some angular values, in order to avoid discontinuity and singularity, a transformation $T(\cdot)$ between the angular form X_a and trigonometric one X_t have to be defined:

$$X_t = T(X_a) \tag{4}$$

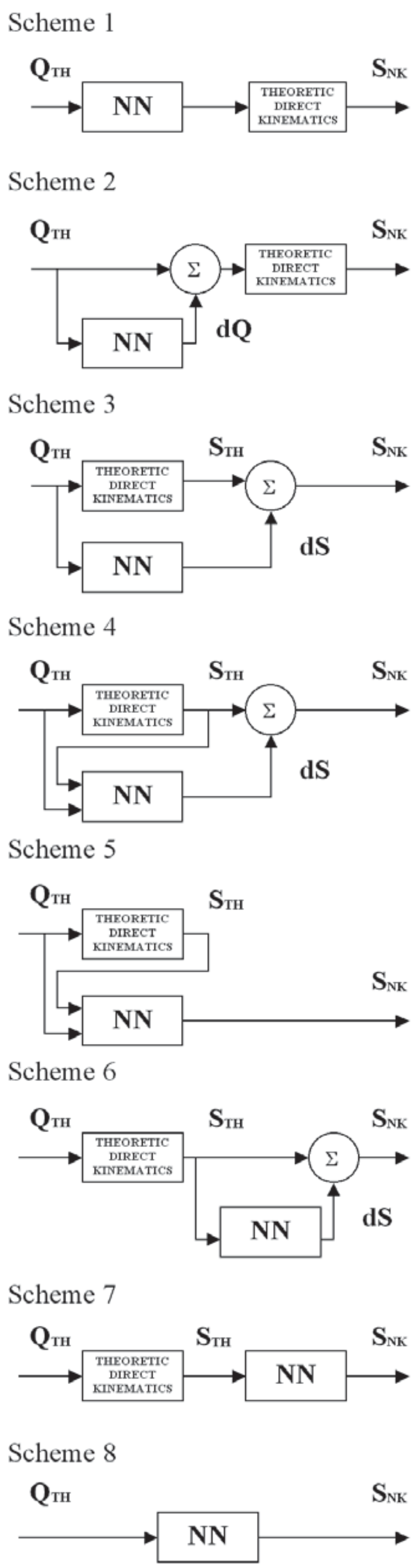

Figure 5: The direct Neuro-Kinematic models tested

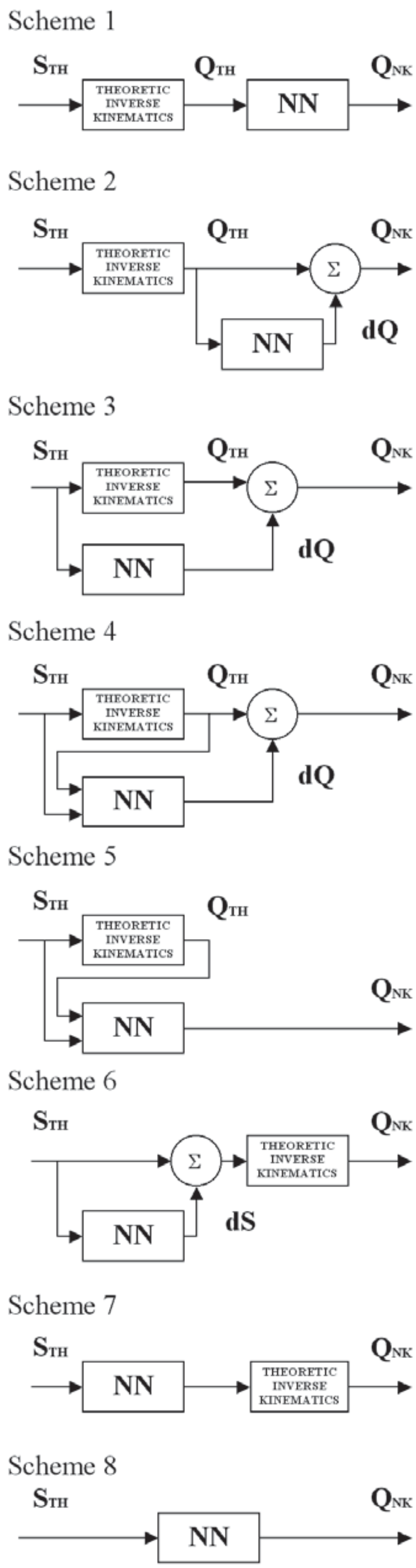

Figure 6: The inverse Neuro-Kinematic models tested

θ	$d\theta$	θ_c
θ	$d\theta$	$\theta + d\theta$
θ	$sind\theta$ $cosd\theta$	$\theta + atan2(sind\theta; cosd\theta)$
$sin\theta$ $cos\theta$	$\Delta sin\theta$ $\Delta cos\theta$	$atan2(sin\theta + \Delta sin\theta; cos\theta + \Delta cos\theta)$

Table 1: Different types of angular sum

X	dX	X_c
X_a	dX_a	$X + dX$
X_a	$T(dX_a)$	$X + T^{-1}(dX)$
$T(X_a)$	$dT(X_a)$	$T^{-1}(X + dX)$

Table 2: Different types of angular sum

The choice of the inverse transformation form $T^{-1}(\cdot)$ have to take in to account that, if X_t is redundant, some fundamental trigonometric relations may be not satisfied ($cos\alpha^2 + sin\alpha^2 \simeq 1$). The transformation chosen for the joint coordinates Q of the SCARA robot is:

$$\begin{aligned} X_a &= [\alpha \; \beta] \\ X_t = T(X_a) &= [sinX_{a1} \; cosX_{a1} \; sinX_{a2} \; cosX_{a2}] \\ &= [sin\alpha \; cos\alpha \; sin\beta \; cos\beta] \\ T^{-1}(X_t) &= [atan2(X_{t1}, X_{t2}) \; atan2(X_{t3}, X_{t4})] \\ &= [atan2(sin\alpha, cos\alpha) \; atan2(sin\beta, cos\beta)] \end{aligned}$$

Gripper coordinates S do not contain angular values, so no transformation is necessary .

Generalizing cases of Tab. 1, there are three types of angular sum shown in Tab. 2.

4.2 Preliminary tests

The simulation tests were performed as follows.

A first computing program based on Eq. 3 and simulating the real robot was used to generate a set of robot poses S_{re} starting from a given set of joint coordinates. Some of the poses and the corresponding joint coordinates were used to train the NN of the NK models, while the others were used as validation set.

Proper tests suggested the correct values for the number of hidden neurons and for the training parameters: learning rate η (0.01) and momentum α (0.9). These values proved to be suitable for all the considered NK schemes. Scheme 8 using a plain NN without robot kinematics was discharged due to its poor performances.

The first tests were performed on the direct kinematics schemes considering the sources of the pose errors described in Tab. 3, excluding random components. Compliance is modeled by torsional springs representing elasticity in the kinematics transmissions; k_1 and k_2 are their stiffness constants. Constant forces are applied to the links at points P_1 and P_2 (Fig. 1) and produce extra joint angular deflections whose amplitude depends on the robot configuration. The tests were repeated three times, simulating the real robot with the numerical values reported in Tab. 4. The considered errors are much more severe than those usually present in actual robots.

The two last lines of Tab. 4 contain the mean and maximum position error before calibration.

Forty-six poses uniformly distributed in the working area were used to train the network. The back-propagation learning phase of the NN was performed in batch-mode [Haykin (1999)] and

dl_1	error in the length of the first link
dl_2	error in the length of the second link
$d\alpha$	error in the first joint rotation
$d\beta$	error in the second joint rotation
k_1	torsional stiffness of the first joint
k_2	torsional stiffness of the second joint
F_1	force applied on point P_1 (first link)
F_2	force applied on point P_2 (second link)

Table 3: Components of error considered

	case 1	*case* 2	*case*3
l_1 [mm]	330	330	330
l_2 [mm]	330	330	330
δl_1 [mm]	5	5	0.5
δl_2 [mm]	-6	-6	-1
$\delta\alpha$ [deg]	2	2	0.15
$\delta\beta$ [deg]	-1.3	-1.3	0.05
k_1 [Nm/rad]	rigid	1000	80000
k_2 [Nm/rad]	rigid	1000	70000
$F_{1x}; F_{1y}$ [N]	[0;0]	[100;0]	[200;-100]
$F_{2x}; F_{2y}$ [N]	[0;0]	[100;0]	[-300;200]
E_{ave} [mm]	6.67	8.93	0.76
E_{max} [mm]	10.2	17.0	1.26

Table 4: Values of the components of error considered

lasted for 1000 epochs.

During and after this learning process, the NK models were used to predict the pose of 1244 robot configurations forming the validation set.

Results are presented in Tab. 5 and in Fig. 7. Last column of Tab. 5 contains the optimal number of hidden neurons of the NN for each scheme (among those tested (10,15,20)).

All the considered NK schemes (except for 6 and 7) performed well on the training set giving an error in the range $(10^{-7} \div 10^{-5})\,m$. Results on the validation set (Tab. 5) confirm the ability of some NK schemes to generalize the learning.

scheme	*case* 1	*case* 2	*case* 3	HN
1	0.03950	0.03230	0.00990	20
2	0.00019	0.00094	0.00077	20
3	0.00405	0.02880	0.00317	20
4	0.00114	0.00607	0.00105	20
5	0.02340	0.02350	0.00163	20
6	0.52100	0.50700	0.06140	15
7	0.77000	0.47300	0.06220	20

Table 5: Average error $[mm]$ on validation set after the training phase and optimal number of hidden neurons

4.3 Optimal NN selection

An analysis of the results shows that schemes 2 and 4 perform much better than the others in all the considered situations.

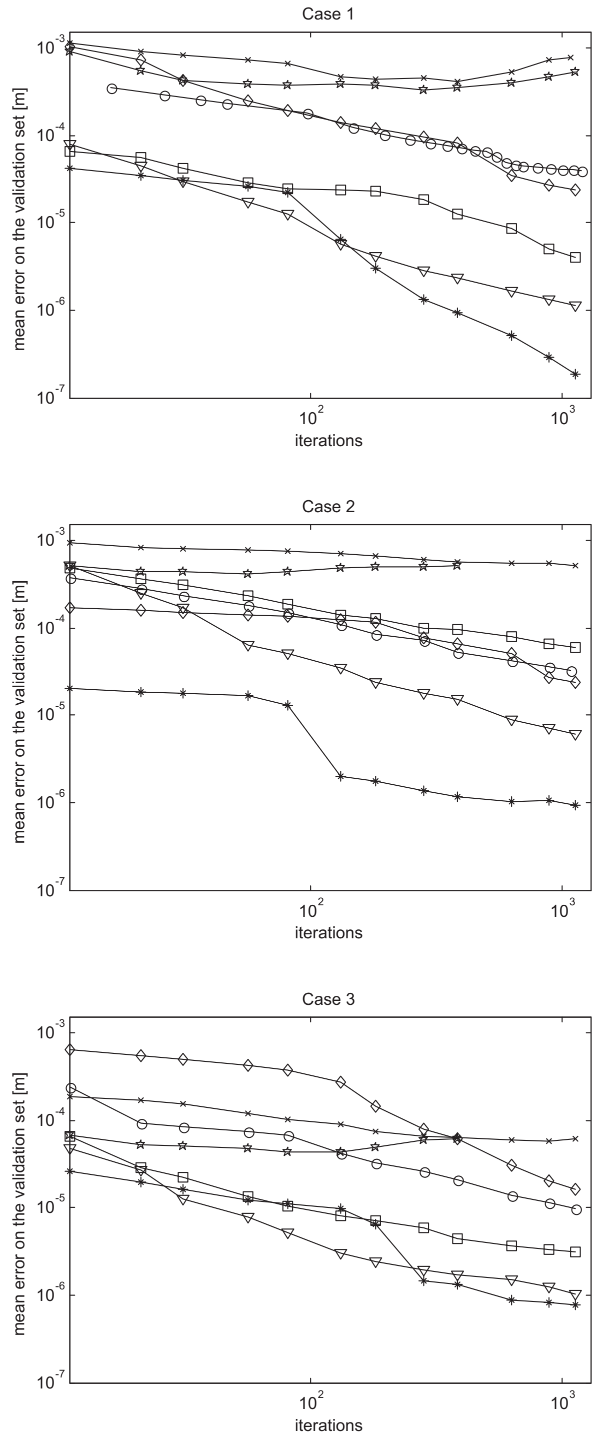

Scheme	1	2	3	4	5	6	7
Symbol	o	$*$	$\square$	$\triangledown$	$\Diamond$	$\star$	$\times$

Figure 7: Average error on the validation set, during the learning process, for the considered schemes in the 3 error cases

First at all, schemes 1 to 5 using joint coordinates Q as input for the NN performed better with respect to those based only on gripper coordinates S, probably because the same gripper position can be reached with different values of the joint coordinates resulting in different pose errors.

Moreover, the parallel schemes (2,3,4,5 and 6) are preferred than the series ones (1,7); probably because the NN has to learn just the difference between the nominal and the actual robot kinematics.

As already mentioned a scheme adopting only a NN without a nominal kinematic model was rejected after the preliminary tests because its performances were clearly worse.

After all the tests the NK models 2 and 4 confirmed to be a good tool to predict the kinematic behaviour of the actual robot. Few neurons were sufficient to reproduce the direct kinematics even in presence of load deflecting the joints. These two schemes were selected for further tests.

4.4 Tests with random errors

After having identified the more efficient NK schemes, further tests permitted to verify the NN behaviour in presence of noise or random errors like backlash.

All the poses constituting the training set were corrupted adding random errors with the maximum amplitude described in Tab. 6. E is the average pose error while the random component of the pose error E_r is computed as difference between the pose reached by the robot with constant and random errors and the pose reached by the robot with only the constant part of the errors.

Then the NN of the NK models 2 and 4 were trained using the corrupted set following the procedure denoted as ”early stopping method” [Haykin (1999)].
The number of training poses was dropped to 36 and the number of the neurons was experimentally minimized in order to avoid the overfitting risk while keeping good convergence on the corrupted training set.

Finally the average and maximum pose error were evaluated with respect to the validation set. Results are reported in Tab. 7 for the direct kinematics and in Tab. 8 for the inverse one.

In this case for the NK schemes two performance indexes were evaluated: the ”actual error” and the ”apparent error”. The actual error (E_{ac}) is the error evaluated comparing the gripper pose predicted by the NK model with the pose of the validation set not affected by random noise. The apparent error (E_{ap}) is the difference between the predicted poses and the poses of the validation set corrupted by the random noise. It is important to note that $E_{ac} < E_{ap}$. In other words, the NN reduces the effect of the random noise filtering it. With reference to the symbols of Tab. 6, 7 and 8, we evaluated the filtering index as:

$$FI = \frac{E_{ac}}{E_r} \tag{5}$$

Depending on the NK scheme, the filtering index was in the range $30\% \div 80\%$.

This result means that if the NN is trained using data having a certain amount of random error E_r, the apparent error in the validation set would be nearly equal to E_r, but the actual error would probably be much lower ($30\% \div 80\%$) because the NN produces an ”average” effect on the data. This is quite desirable.

The same considerations can be made for the inverse NK schemes: using the same values of the errors of Tab. 6, the results obtained (Tab. 7, Tab. 8) show that schemes 2 and 4 are suitable for inverse kinematic calibration too.

parameters	*const*	*rand*
δl_1 [mm]	5	± 0.1
δl_2 [mm]	-6	± 0.12
$\delta\alpha$ [deg]	2	± 0.04
$\delta\beta$ [deg]	-6	± 0.026
δx [mm]	0	± 0.01
δy [mm]	0	± 0.01
pose error	*ave.*	*max.*
E [mm]	12.6	20.0
E_r [mm]	0.17	0.49

Table 6: Parameters for tests with random noise and corresponding pose error before calibration.

scheme	2		4	
HN	8		2	
error	*ave.*	*max.*	*ave.*	*max.*
E_{ap} [mm]	0.21	0.67	0.17	0.44
E_{ac} [mm]	0.14	0.43	0.05	0.17
FI	86%		32%	

Table 7: Results of the tests with random errors on validation set after direct kinematics calibration

scheme	2		4	
HN	7		5	
error	*ave.*	*max.*	*ave.*	*max.*
E_{ap} [mm]	0.18	0.54	0.19	0.66
E_{ac} [mm]	0.08	0.28	0.10	0.38
FI	49%		62%	

Table 8: Results of the tests with random errors on validation set after inverse kinematics calibration

4.5 Considerations

Schemes 2 and 4 proved to perform well even in presence of random errors and guarantee a final actual error close to the robot repeatability. Of course in experimental application only the apparent error can be estimated, but it is reassuring that the actual error would be a little better than it.

This good results encouraged the adoption of similar calibration techniques to more complicated robot models.

5 Application to a simulated Stewart platform

The main feature of the NN based calibration is that it does not require any kind of information about the causes of inaccuracy of the robot. This quality becomes fundamental when the robot has a complex structure.

The authors applied the proposed methodology to a Stewart platform robot having the configuration of Fig. 8.

The spherical hinges of the base (B_i) and the platform (P_i) are placed at the vertices of a regular hexagon and an equilateral triangle inscribed in a circle with a radius of 1 m and 0.5 m respectively. Their position with respect to the base and the platform frames are

$B_i = [x_{bi}\ y_{bi}\ z_{bi}]^t$

$P_i = [x_{pi}\ y_{pi}\ z_{pi}]^t$

Six translational joints (Q_i) link the platform to the base and control its position and orientation (6 dof).

Three frames are used: frame $\{b\}$ fixed to the base, frame $\{p\}$ fixed to the platform and frame $\{g\}$ fixed to the gripper (translated with respect to $\{p\}$ of $z_{pg} = 0.2$ m). The gripper pose is defined by the vector $S = [x_g\ y_g\ z_g\ \psi\ \theta\ \phi]$ (using Tait Brian orientation angles); the length of the six "legs" are used as joint coordinates $Q = [l_1\ l_2\ l_3\ l_4\ l_5\ l_6] = [Q_1\ Q_2\ Q_3\ Q_4\ Q_5\ Q_6]^t$.

The pose of the gripper with respect to the base is represented by the position matrix

$$
\begin{aligned}
& M_{bg} = Trans(X, x_g) \cdot Trans(Y, y_g) \cdot Trans(Z, z_g) \cdot \\
& Rot(X, \psi) \cdot Rot(Y, \vartheta) \cdot Rot(Z, \phi) = \\
& = \begin{bmatrix} c_\theta c_\psi & -c_\theta s_\psi & s_\theta & x_g \\ s_\theta c_\phi + c_\psi s\phi & -s_\psi s_\theta s_\phi + c_\psi c_\phi & -s_\psi c_\theta & y_g \\ -c_\psi s_\theta c_\phi + s_\psi s_\phi & c_\psi s_\theta s_\phi + s_\psi c_\phi & c_\psi c_\theta & z_g \\ 0 & 0 & 0 & 1 \end{bmatrix}
\end{aligned}
$$

the position of the mobile platform with respect to the gripper is

$$
M_{gp} = \begin{bmatrix} 1 & 0 & 0 & 0 \\ 0 & 1 & 0 & 0 \\ 0 & 0 & 1 & -z_{pg} \\ 0 & 0 & 0 & 1 \end{bmatrix}
$$

The inverse kinematic problem is easily solved: the positions of platform hinges $[x'_{pi} y'_{pi} z'_{pi}]^t$ with respect to the base frame $\{b\}$ are computed using the transformation matrix M_{bp} which represents the position of the platform frame with respect to the base one

$M_{bp} = M_{bg} M_{gp}$

$$
\begin{bmatrix} x'_{pi} \\ y'_{pi} \\ z'_{pi} \\ 1 \end{bmatrix} = M_{bp} \begin{bmatrix} x_{pi} \\ y_{pi} \\ z_{pi} \\ 1 \end{bmatrix}
$$

the leg's length are computed as

$$
\begin{aligned}
l_i &= \sqrt{(x_{bi} - x'_{pi})^2 + (y_{bi} - y'_{pi})^2 + (z_{bi} - z'_{pi})^2} \\
i &= 1 \ldots 6
\end{aligned}
\tag{6}
$$

The direct kinematic problem is solved using iterative numerical methodologies (extended Newton-Raphson method).

Three different types of structural errors were added to this simulated robot:

- position error of the hinges of the base and the platform ($\delta x_i\ \delta y_i\ \delta z_i$);
- length error of the legs (δl_i);

- position (δx_g δy_g δz_g) and orientation ($\delta\psi$ $\delta\theta$ $\delta\phi$) error of the gripper with respect to the platform.

The actual value of the geometrical parameters of the robot L is obtained adding three components:

$$L = L_n + \delta L_c \pm \delta L_r \tag{7}$$

where L_n is the nominal (theoretic) value, dL_c is the constant part of the error and dL_r is the random component which varies in each pose. Random component represents backlash and the measurement tool uncertainty. For each geometrical parameter a value of the constant error L_c in the ranges specified in Tab. 9 was randomly chosen.

	δL_c	δL_r
δx_i δy_i δz_i [mm]	± 1	± 0.02
δl_i [mm]	± 3	± 0.02
δx_g δy_g δz_g [mm]	± 0.1	± 0.01
$\delta\psi$ $\delta\theta$ $\delta\phi$ [mrad]	± 0.25	± 0.02

Table 9: Ranges of the constant (δL_c) and the random (δL_r) geometrical error values.

Inside the work space of the robot, defined as

$$\begin{array}{rcl} -0.2\,m & < x_g < & 0.2\,m \\ -0.2\,m & < y_g < & 0.2\,m \\ 1.0\,m & < z_g < & 1.4\,m \\ -30\,deg & < \psi < & 30\,deg \\ -30\,deg & < \theta < & 30\,deg \\ -30\,deg & < \phi < & 30\,deg \end{array}$$

50 poses (randomly distributed) for learning set (lea) and 100 for validation (val) were selected.

As a consequence of the (small) geometrical errors, the theoretical gripper pose differs from the actual pose. The homogeneous matrix M that describes the roto-translation between them has the following form

$$M \simeq \left[\begin{array}{ccc|c} 1 & -\Delta\phi & \Delta\theta & \Delta x \\ \Delta\phi & 1 & -\Delta\psi & \Delta y \\ -\Delta\theta & \Delta\psi & 1 & \Delta z \\ \hline 0 & 0 & 0 & 1 \end{array}\right] \tag{8}$$

Calibration has the aim of minimizing the difference between predicted and actual pose, i.e. minimizing the extra diagonal elements of M. To measure the pose prediction quality two different error index were computed, the first for position, the second for orientation:

$$E_{xyz} = \sqrt{\Delta x^2 + \Delta y^2 + \Delta z^2} \tag{9}$$

$$E_{ang} = \sqrt{\Delta\psi^2 + \Delta\theta^2 + \Delta\phi^2} \tag{10}$$

[mm]	set	E	δL_r		$\delta L_r/2$		$\delta L_r = 0$	
			ave	*max*	*ave*	*max*	*ave*	*max*
δL_c	lea	*xyz*	5.98	14.3	5.98	20.7	5.98	20.6
		ang	9.60	17.1	9.34	20.5	9.34	20.5
		xyz_r	0.10	0.26	0.04	0.14	0	0
		ang_r	0.08	0.17	0.03	0.10	0	0
	val	*xyz*	5.99	28.8	6.47	50.0	6.48	50.1
		ang	9.62	26.0	9.93	59.9	9.96	60.1
		xyz_r	0.11	0.60	0.05	0.40	0	0
		ang_r	0.09	0.56	0.04	0.31	0	0
$\delta L_c/2$	lea	*xyz*	3.22	13.5	2.87	7.03	3.24	13.5
		ang	4.88	12.3	4.62	7.12	4.88	12.3
		xyz_r	0.10	0.38	0.05	0.18	0	0
		ang_r	0.08	0.27	0.04	0.13	0	0
	val	*xyz*	2.93	9.91	3.10	25.3	2.93	9.76
		ang	4.70	10.5	4.86	24.7	4.70	10.1
		xyz_r	0.10	0.46	0.05	0.24	0	0
		ang_r	0.08	0.38	0.04	0.23	0	0

Table 10: Pose errors for the Stewart platform before calibration (mm or mrand).

Average and maximum values on the validation set before calibration are shown in Tab. 10; to highlight the effects of constant and random errors, simulation tests were repeated 6 times with different combinations of the constant $(\delta L_c, \delta L_c/2)$ and of the random $(\delta L_r, \delta L_r/2, 0)$ errors. In Tab. 10 values labelled by *xyz* and *ang* are the average linear and angular error, while xyz_r and ang_r are the random components.

Contrary to serial robots, in parallel ones a joint configuration Q can bring the robot gripper in several different poses with different pose errors. This means that the robot configuration is completely defined only when the pose vector S is known. However, in actual uses of parallel robots, only one of the possible joint configuration is used because the change of the configuration implies the crossing of a singularity (where the structure is under-constrained). With this restriction even vector Q gives full information. For this reason, the calibration schemes that can be used are 2, 4 and 6.

Scheme 4 and 6 involve an angular sum on gripper coordinates S (orientation angles ψ,θ and ϕ). In order to avoid singularities of Tait Brian angles ($\theta = \pm\pi/2$) and discontinuity across $\pm\pi$ the transformation $T(\cdot)$ was built choosing eight elements of matrix M_{bp} and defining the angular S_a and the trigonometric S_t form of S:

$$\begin{aligned}
S_a &= [x\ y\ z\ \psi\ \theta\ \phi]^t \\
S_t = T(S_a) &= [x\ y\ z\ c_\theta c_\psi\ \ -c_\theta s_\psi \\
&\quad s_\theta\ \ -s_\psi c_\theta\ \ c_\psi c_\theta]^t \\
&= [S_{t1}\ S_{t2}\ S_{t3} \therefore S_{t8}]^t \\
S_a = T^{-1}(S_t) &= [S_{t1}\ S_{t2}\ S_{t3}\ atan2(-S_{t7}, S_{t8}) \\
&\quad asin(S_{t6})\ \ atan2(-S_{t5}, S_{t4})]^t
\end{aligned}$$

Pose error after calibration of the inverse kinematics are shown in Tab. 11. The average actual error on the validation set was strongly reduced but not enough to reach the repeatability of the robot E_r: for this reason the filter index FI is greater than 100%.

The proposed calibration methodology applied to a 6 dof robot had worse performance than the

2 dof SCARA. It is important to notice that NN's learning is, practically, an interpolation procedure so the density of the poses in the training set is a main factor for a good performance. If the robot has several dof, a great number of measured poses are necessary to cover the n-dimensional work-space of the robot (with n=dof).
Some comments are: the pose errors after calibration in the validation set is 2 or 3 times that of the calibration set having the same initial value of constant and random error. The two considered schemes have in average the same performances: the average accuracy error is reduced from some millimeters to about 0.1 mm. The presence of the random error significantly degrades the calibration performance.

[mm]	set	E	δL_r		$\delta L_r/2$		$\delta L_r = 0$	
			ave.	*max.*	*ave.*	*max.*	*ave.*	*max.*
δL_c	lea	xyz ap	.074	.203	.054	.118	.026	.078
		ang ap	.160	.504	.111	.299	.061	.190
		xyz ac	.066	.182	.054	.110	.026	.078
		ang ac	.142	.501	.108	.338	.061	.190
	val	xyz ap	.133	1.03	.112	1.49	.087	.737
		ang ap	.327	3.40	.282	5.15	.225	2.47
		xyz ac	.123	.924	.111	1.55	.087	.737
		ang ac	.304	3.01	.280	5.32	.225	2.47
	FI	xyz	132%		217%		-	
		ang	386%		669%		-	
$\delta L_c/2$	lea	xyz ap	.040	.114	.019	.036	.010	.023
		ang ap	.101	.320	.041	.106	.025	.077
		xyz ac	.039	.098	.021	.049	.010	.023
		ang ac	.084	.280	.044	.121	.025	.077
	val	xyz ap	.096	.384	.045	.258	.032	.115
		ang ap	.198	1.19	.107	.755	.086	.465
		xyz ac	.083	.046	.040	.246	.032	.115
		ang ac	.173	1.50	.097	.689	.086	.465
	FI	xyz	217%		86%		-	
		ang	669%		258%		-	

Table 11: Pose errors after inverse kinematics calibration of the Stewart platform using scheme 2.

6 Full SCARA model

The set of structural errors used for the SCARA robot simulated in the previous case was not complete. This means that not all possible geometrical inaccuracy were considered for the simulated robot. In order to test the NN based calibration methodology with a full robot model, a 3 dof SCARA manipulator was used.

The kinematics model is shown in Fig. 9: reference frames are positioned on the robot using Denavit & Hartenberg conventions.

In a generic serial robot the number of geometrical errors is

$$N = 6 + 4R + 2P \tag{11}$$

were R is the number of rotational joint and P the number of translational one. However, depending on the measuring instrumentation, just some of them can be estimated. Assuming that G

[mm]	set	E	δL_r		$\delta L_r/2$		$\delta L_r = 0$	
			ave.	*max.*	*ave.*	*max.*	*ave.*	*max.*
δL_c	lea	xyz ap	.039	.087	.025	.057	.021	.053
		ang ap	.080	.178	.056	.182	.051	.174
		xyz ac	.039	.092	.026	.054	.021	.053
		ang ac	.085	.286	.061	.155	.051	.174
	val	xyz ap	.115	.659	.068	.648	.081	.832
		ang ap	.287	2.01	.161	2.24	.183	2.41
		xyz ac	.103	.600	.064	.559	.081	.832
		ang ac	.264	1.62	.153	1.94	.183	2.41
	FI	xyz	110%		125%		-	
		ang	336%		366%		-	
$\delta L_c/2$	lea	xyz ap	.033	.108	.030	.076	.010	.033
		ang ap	.084	.382	.066	.417	.022	.110
		xyz ac	.032	.066	.030	.087	.010	.033
		ang ac	.068	.227	.067	.256	.022	.110
	val	xyz ap	.073	.259	.071	.213	.041	.303
		ang ap	.143	.750	.160	1.28	.095	1.05
		xyz ac	.061	.160	.061	.383	.041	.303
		ang ac	.113	.505	.149	1.18	.095	1.05
	FI	xyz	60%		131%		-	
		ang	137%		395%		-	

Table 12: Pose errors after inverse kinematics calibration of the Stewart platform using scheme 4.

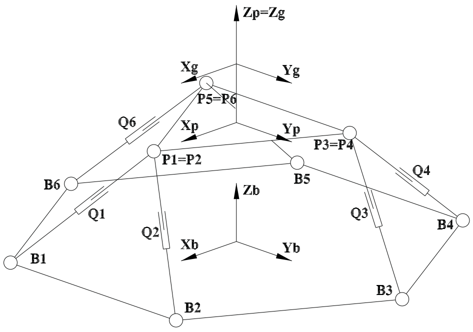

Figure 8: Simulated Stewart platform.

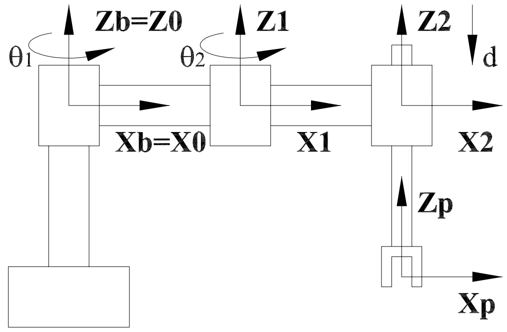

Figure 9: Simulated 3 DOF SCARA.

coordinates of the gripper pose can be measured the number of the identifiable parameters is

$$N = G + 4R + 2P \tag{12}$$

Eq. 11 and Eq. 12 are obtained generalizing the concepts described in [Mooring et al.(1991)]. Since we assumed that only the position ($x\ y\ z$) of the gripper could be measured (and not its orientation), the number of geometrical error parameters which have to be defined to describe the robot geometry is $N = 3 + 4 \cdot 2 + 2 \cdot 1 = 13$.

A complete set of parameters describing the 3 dof SCARA geometry and compliance was selected [Omodei et al. (2000), Legnani et al.(2001)]. Nominal values and errors of the geometrical and compliance parameters are shown in Tab. 13 and Tab. 14 respectively.

A force F, whose components are function of the pose coordinates was applied to the gripper causing joint and gripper deflections (Tab. 15).

$$F_x = c_1 x + c_2 xy + c_3 z$$

L		L_n	δL_c	δL_r
X_0	trans(X_b) [mm]	0	2.5	± 0.02
Y_0	trans(Y_b) [mm]	0	-2.2	± 0.02
χ_0	rot(X_b) [mrad]	0	2.3	± 0.02
ψ_0	rot(Y_b) [mrad]	0	-1.7	± 0.02
θ_1	rot(Z_0) [mrad]	Q_1	-1.7	± 0.02
a_1	trans(X_0) [mm]	330	0.4	± 0.02
α_1	rot(X_0) [mrad]	0	0.1	± 0.02
ψ_1	rot(Y_0) [mrad]	0	-0.3	± 0.02
θ_2	rot(Z_1) [mrad]	Q_2	0.7	± 0.02
a_2	trans(X_1) [mm]	330	-0.4	± 0.02
α_2	rot(X_1) [mrad]	0	0.2	± 0.02
ψ_2	rot(Y_1) [mrad]	0	1.7	± 0.02
d	trans(Z_2) [mm]	Q_3	0.1	± 0.02

Table 13: Geometrical parameters of the 3 dof SCARA.

L	L_n	δL_c	δL_r
K_{xy} [m/N]	*rigid*	10^{-5}	$\pm 10^{-6}$
K_z [m/N]	*rigid*	10^{-5}	$\pm 10^{-6}$
$K_{\theta 1}$ [rad/Nm]	*rigid*	10^{-5}	$\pm 10^{-6}$
$K_{\theta 2}$ [rad/Nm]	*rigid*	10^{-5}	$\pm 10^{-6}$
K_d [m/N]	*rigid*	10^{-4}	$\pm 10^{-6}$

Table 14: Compliance parameters of the 3 dof SCARA.

	L_n	δL_c	δL_r
c_1	0	3	± 2
c_2	0	-6	± 2
c_3	0	12	± 2
c_4	0	-15	± 2
c_5	0	30	± 2
c_6	0	3	± 2
c_7	0	6	± 2
c_8	0	-18	± 2

Table 15: Coefficients of Eq. 13: forces in [N] distances in [m].

$$\begin{aligned} F_y &= c_4 x_2 + c_5 xz \\ F_z &= c_6 + c_7 z + c_8 xy \end{aligned} \tag{13}$$

Inside the work space (which has a torus shape $R_{int} = 0.13$ m, $R_{ext} = 0.53$ m, 0 m $< z <$ 0.3 m) 72 uniformly distributed poses for the learning set (lea) and 430 for the validation set (val) were selected. The pose error is computed using Eq. 9. Average and maximum values of the pose error E and the random component E_r before calibration are shown in Tab. 16. To better analize the properties of the calibration technique in different situations, the algorithms have been tested with different combinations of constant (δL_c) and random (δL_r) errors values.

Apparent and actual pose error after direct kinematics calibration using scheme 3 and 4 are shown in Tab. 17 and Tab. 18 respectively. Gripper coordinates don't include angular values, so no transformation $T(\cdot)$ is needed.

Results reported in Tab. 16, Tab. 17 and Tab. 18 show that the calibration procedure proposed

[mm]	set	E	δL_r		$\delta L_r/2$		$\delta L_r = 0$	
			ave	*max*	*ave*	*max*	*ave*	*max*
δL_c	lea	E	3.44	4.61	3.51	4.44	3.50	4.50
		E_r	0.28	0.65	0.15	0.29	0	0
	val	E	3.51	4.93	3.51	4.85	3.50	4.74
		E_r	0.30	0.65	0.14	0.32	0	0
$\delta L_c/2$	lea	E	1.80	2.60	1.77	2.36	1.76	2.28
		E_r	0.26	0.54	0.13	0.28	0	0
	val	E	1.76	2.85	1.76	2.35	1.74	2.42
		E_r	0.27	0.64	0.14	0.32	0	0

Table 16: Pose errors for the 3 dof SCARA before calibration.

[mm]	set	E	δL_r		$\delta L_r/2$		$\delta L_r = 0$	
			ave	*max*	*ave*	*max*	*ave*	*max*
δL_c	lea	ap	0.27	0.52	0.21	0.45	0.07	0.16
		ac	0.18	0.39	0.16	0.38	0.07	0.16
	val	ap	0.38	1.01	0.23	0.60	0.12	0.48
		ac	0.23	0.70	0.18	0.44	0.12	0.48
		FI	76%		131%		-	
$\delta L_c/2$	lea	ap	0.29	0.65	0.12	0.25	0.04	0.10
		ac	0.21	0.60	0.10	0.20	0.04	0.10
	val	ap	0.37	0.96	0.17	0.39	0.05	0.18
		ac	0.24	0.80	0.10	0.34	0.05	0.18
		FI	89%		74%		-	

Table 17: Pose errors after direct kinematics calibration of 3 dof SCARA using scheme 3.

[mm]	set	E	δL_r		$\delta L_r/2$		$\delta L_r = 0$	
			ave	*max*	*ave*	*max*	*ave*	*max*
δL_c	lea	ap	0.29	0.57	0.19	0.50	0.03	0.08
		ac	0.19	0.34	0.15	0.41	0.03	0.08
	val	ap	0.36	0.96	0.21	0.53	0.05	0.30
		ac	0.21	0.54	0.15	0.41	0.05	0.30
		FI	69%		109%		-	
$\delta L_c/2$	lea	ap	0.25	0.58	0.12	0.25	0.006	0.02
		ac	0.14	0.31	0.09	0.18	0.006	0.02
	val	ap	0.30	0.63	0.17	0.43	0.01	0.10
		ac	0.14	0.37	0.10	0.30	0.01	0.10
		FI	51%		74%		-	

Table 18: Pose errors after direct kinematics calibration of 3 dof SCARA using scheme 4.

is very effective in the reduction of the positioning error. By using both scheme 3 and 4 the error is reduced to values close. For the considered manipulator the best results are achieved by scheme 4.

As observed for the 2 DOF SCARA robot, the NN partially filters the random errors.

7 Conclusions

The paper presents a preliminary study on an innovative Neural Network based calibration procedure. Different schemes of a Neuro-Kinematic model were tested in direct and inverse kinematic calibration both on serial and parallel simulated robots. Three of them obtained good performances: in all considered cases accuracy error was reduced nearly to robot repeatability. It was also shown that the NK model is able to filter part of the noise component present in the measures.

The NN based procedure seems to be suitable to the calibration of all robot types and extremely simple to use: only the nominal kinematic model of the robot is needed, the procedure is able to compensate for all type of ripetitive errors present in the robot (geometrical, load deflections, ...) without modelling them.

Similarly to other procedures, a proper (quite large) number of measured poses distributed in the workspace (or in a part of it) is needed. The results obtained in the simulated cases encouraged the authors to apply the proposed procedure to actual robots.

References

[Nowrouzi et al.(1988)] Nowrouzi A., Kavina Y.V., Kochekali H., Whitaker R.A., An overview of robot calibration techniques, Ind Robot, pp. 229-232, 15(4), 1988.

[Zierteg and Datseris (1989)] Zierteg J., Datseris P., Basic considerations for robot calibration, Int J Robot Aut 4(3), 1989, pp.158-166.

[Mooring et al.(1991)] Mooring B.W., Roth Z.S., Driels M.R., Fundamentals of manipulator calibration, New York, 1991.

[Kovac and Frank (1992)] Kovac I., Frank A., A novel industrial robot calibration device, Proc. of First RAA, Porotoz, Slovenia, pp. 162-167, 1992.

[Faglia et al. (1993)] Faglia R., Legnani G., Magnani P.L., Docchio F., Minoni U., Calibration of a SCARA robot by optical measurements: Methodology and experimental results, ISMCR'92 2nd Int Symp on Measurement and Control in Robotics, Sept. 21-24, 1993.

[Legnani et al.(1996)] Legnani G., Mina C., Trevelyan J.P., Static calibration of industrial manipulators: Design of an optical instrumentation and application to SCARA robots, J Robot Syst, 13(7), 1996.

[Trevelyan et al.(1996)] Legnani G., Trevelyan J.P., Static calibration of industrial manipulators: a comparison between two methodologies, Robotics Toward 2000 Twenty-Seventh Int Symp on Industrial Robots, pp. 111-116, Oct. 6-8, 1996.

[Khoshzaban et al.(1996)] Khoshzaban M., Sassani F., Lawrence P.D., Kinematic calibration of industrial hydraulic manipulators Robotica v.14, pp. 541-551, 1996.

[Haykin (1999)] Haykin S., Neural networks: a comprehensive foundation, Prentice hall, 1999.

[Omodei et al. (2000)] Omodei A., Legnani G., Adamini R., Three Methodologies for the Calibration of Industrial Manipulators: Experimenthal Results on a SCARA Robot J. of Robotic System 17(6), pp. 291-307, Wiley, 2000.

[Legnani et al.(2001)] Legnani G., Adamini R., Jatta F., Calibration of a SCARA Robot by Force-Controlled Contour Tracking of an Object of Known Geometry, 32nd ISR, Korea, Apr. 19-21, 2001.

[Tiboni et al. (2003)] M. Tiboni, G. Legnani, P. L. Magnani and D. Tosi, A closed-loop neuroparametric methodology for the calibration of a 5 DOF measuring robot, Proceedings of the IEEE Int. Symp. on Computational Intelligence in Robotics and Automation, July 2003, Kobe Japan, pp 1482- 1487.

[Fazenda et al. (2006)] Fazenda N., Lubrano E., Rossopoulos S., Clavel R. Calibration of the 6 DOF High-Precision Flexure Parallel Robot Sigma 6, Proceed. of the 5th Chemnitz Parallel Kinematics Seminar, Chemnitz, April 25-26, 2006.

Innovative accession to the ring measurement in the control process using the machine vision

M. Šimic, N. Herakovič, Faculty of Mechanical Engineering, Laboratory for Handling, Assembly and Pneumatics, Ljubljana, Slovenia

F. Trdič, J. Skvarč, FDS Research, Trzin, Slovenia

Abstract
In this paper the development of an intelligent control system with integrated robot vision is considered to enable the solving of complex assembly and quality control tasks with high accuracy and speed. The application of machine vision is a multilayer problem which demands a great amount of expert knowledge, experiences and innovations. The developed algorithm, presented in the paper, is used for the diameter and the roundness measurement of welded rings. Three different quality range systems are presented and discussed at the end of the paper. The results enable the successful replacement of manual (carried out by operators) quality control of the welded ring by a machine-vision control, which ensures better efficiency and accuracy of the ring's quality-control process over an unlimited time period, independently of various subjective and objective disturbances.

1 Introduction

Robot welding is well known operation in many industrial applications despite of its problems appearing during the process. The welding process is confronted with one of its major problems, the contraction or extension of a welding area, i.e. the heating zone. Therefore the products are not the same size before and after the welding process. The other, even more complex problem is to bend a ring into a perfect circle and keep it in that shape after the welding process is finished. To assure the appropriate dimensions of the welded ring at the end of the welding process, the process itself must be carried out adequately and the quality control at the end of the welding process must be carried out accurately and with high speed without interrupting the assembly process too much.

Development of an intelligent control system with integrated robot vision for the above mentioned task, presented in this paper, is successfully accomplished at the end by the industrial application. In spite of numerous research works done in the past, every new application of the robot vision is faced with a multilayer problem which demands a great amount of expert knowledge, experiences and innovations (Trdič, F., 2006; West, P., 2006).

Introducing machine vision control into assembly process demands in the beginning the clarification of the purpose of the application, which is usually not only the problem of measuring of one or more product parameters in a very short time but also the fault detection, usually detected in manual assembly by workers, based on adequate sample. The control system, considered in this paper, must work also in the industrial environment, where the available control time expenses are limited.

In many assembly processes the control process is still done by workers. They are capable to make estimation and judgment about a product or a part accuracy and shape fault using personal skinless of quick and accurate decisions based on human vision system. The tasks are usually complex and the accuracy and speed depends on worker's psychical and physical condition. The consequences are untrustworthy results and huge possibility of overlooking the faults. The reliability of human decisions is decreased also by monotony and tiredness.

Today's machine vision systems are more and more reliable and robust and therefore convenient for industrial applications and are becoming indispensable in assembly process (Braggins, D., 2006). Control systems, based on machine vision, are capable of performing control process even more efficient than the human, if the conditions for an appropriate usage of technical benefits of machine vision are assured.

The machine vision system, being used in industrial environment for tasks such as inspection, measurement and fault detection, has to be a robust and very reliable system. For that reason the development process of the measurement equipment using machine vision has to follow the fixed procedure (Trdič, F., 2006; West, P., 2006). Usually the procedure is split into precise determination of tasks (measuring, fault detection) and goals, into machine vision component selection and working conditions (illumination, position determination), component selection of machine vision (camera, computer, lenses and optics), and finally development of an automatic part robot handling system.

This paper is focused on the development of a mathematical algorithm, which is adapted in a computer software program as a numerical algorithm. The chosen mathematical algorithm is a starting point for the development of an automatic control system. At the end of the paper the analysis of a system's quality is presented and discussed, where three different kinds of control systems: theoretical, experimental and industrial application are compared and discussed.

2 Control goals determination

In the industrial ring welding process, the final product quality control represents the measuring of diameter and roundness of a welded ring, which is then taken into the further assembly operation.

Control process of the ring diameter and roundness follows the previous production processes like cutting the raw material, bending and welding the ring. In all mentioned production processes inaccuracy and faults can occur. Since customer demands high accuracy and repeatability of a measurement, the *100* percent control process should be introduced.

Existent quality control procedure of the welded ring involves visual observing of inner surface on welded ring, where the laser ray is pointed. Using the calibre for dimension checking can cause wrong interpretation of the ring's accuracy. Putting the ring into calibre verifies only the minimum diameter. The maximum diameter range is not considered in this situation. These are additional reasons for introducing a non contact control methods, such as machine vision control is.

Theoretical algorithm for measuring, software program and correct installation of experimental system using the machine vision are developed for the above mentioned application and presented in this paper. The control process involves measurement of:

- diameter Dn (measuring accuracy $\pm 0.05mm$, repeatability $\pm 0.01mm$)
- roundness Ov (measuring accuracy $\pm 0.25mm$, repeatability $\pm 0.05mm$)

The meaning and explanation of measuring parameters are shown and marked in Fig. 2.1. The real shape of the ring is shown as a double thick curve, the minimum (*Dmin*) and maximum

(*Dmax*) diameters of the ring are shown as two low thick curves. The difference between maximum and minimum diameter represents roundness of the ring (*Ov*).

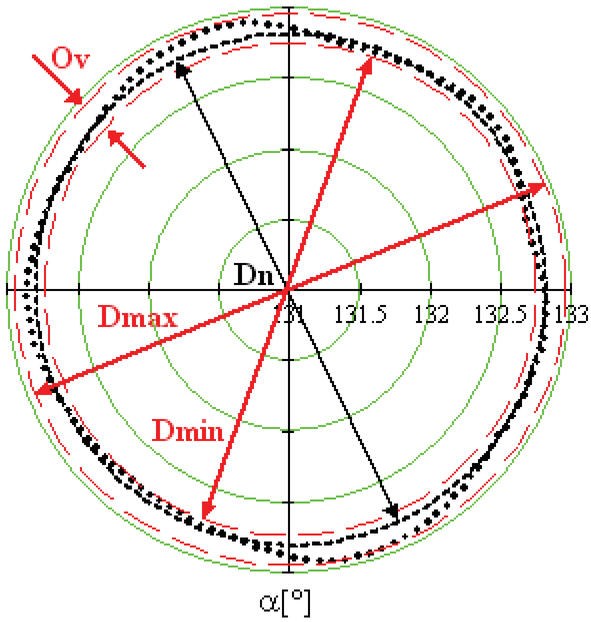

Figure 2.1. Graphical presentation of measuring ring curve.

3 Experimental setup and equipment

The measuring system is placed in a specific position alongside of the transportation line (conveyor belt). The Fig. 3.1 presents only one of the many possibilities, where measuring system is involved in totally automated control centre (Herakovic, N., 2007).

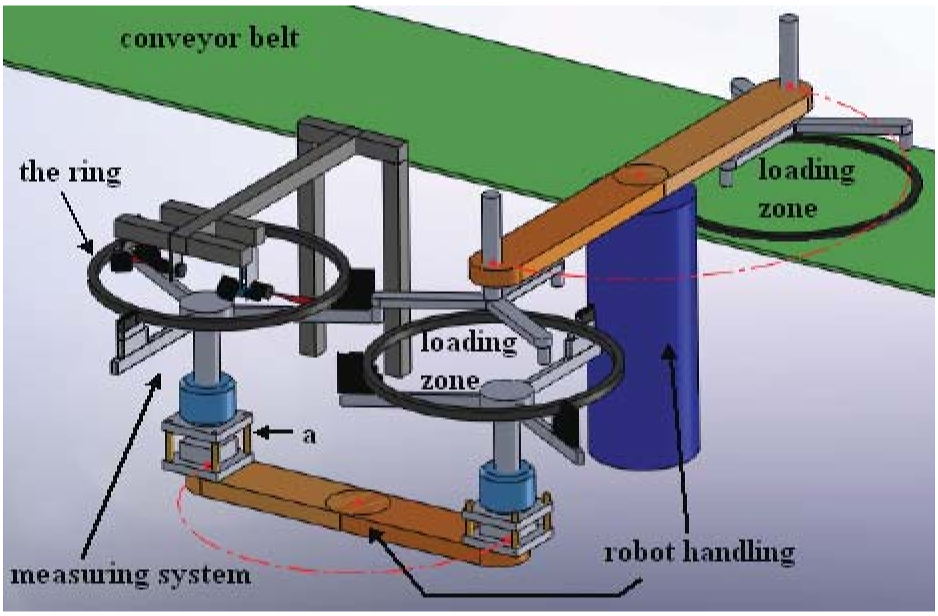

Figure 3.1. Robot handling with machine vision system.

The welded ring is handled by a robot arm from the transportation line to the rotating table on the other side (loading zone). The rotating table is placed in the precise lift up manipulator shown in Fig. 3.1 as mark a (Pauli, J., 2001; Redford, Alan H., 1986).

Main components of typical vision system, used also in presented measuring system, are (Skvarč, J., 2000):

- cameras and camera lenses,
- digitizers (digital, analogue, USB),
- light sources,
- mechanical construction – manipulation of specimens,
- I/O hardware,
- processing units,
- vision software.

The measuring principle of the diameter and the roundness of the welded ring is shown in Fig. 3.2. The construction consists of one camera and one laser source which are mounted in the fixed holder. The welded ring is fixed in the rotating table as shown in Fig. 3.2.

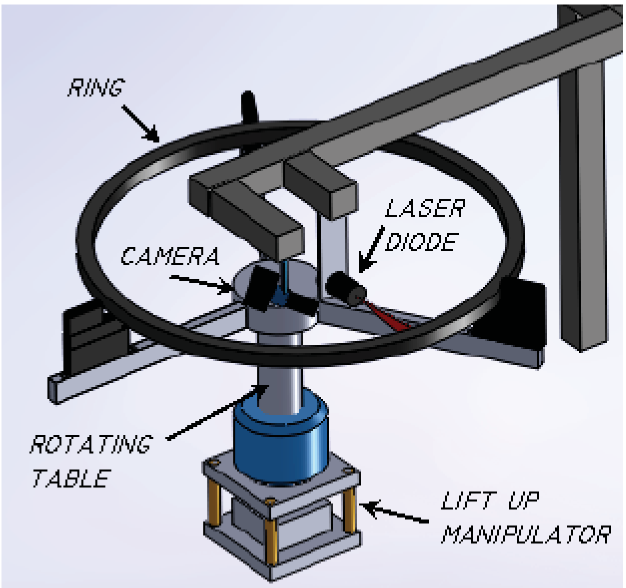

Figure 3.2. The measuring principle.

When the ring is rotating, the camera is taking a snapshot (grabbing) in every *3.6* degrees of the rotating angle, so the *100* photos are taken during one turn of the ring.

4 Theoretical description of the algorithm

4.1 Principles of the triangulation method

The basics of the laser triangulation method are represented in this chapter. The laser ray is directed to the inside of the ring surface as shown in Fig. 4.1, so it is possible to get a measuring lighting line or a point. That line or a point is observed by a camera, which has to be set up correctly. A *30* to *60* degree angle between camera and laser ray is needed to achieve optimal conditions (Gruen, A., 2001; Hecht, E., 1987). If the welded ring is rotated, the observing line or point is moving along the radius or laser ray direction. All parameters, which are needed for a triangulation method calculation, are shown in Fig. 4.1 and Fig. 4.2.

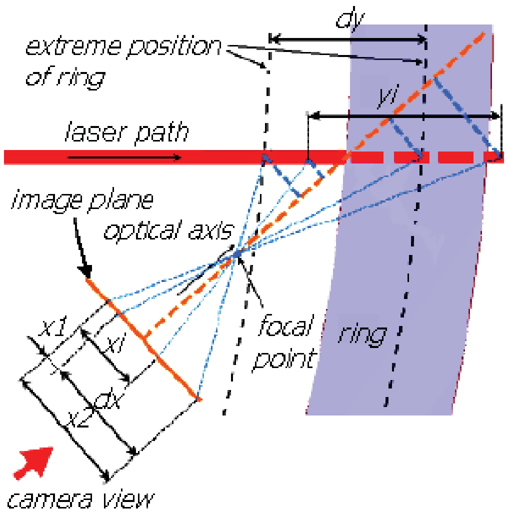

Figure 4.1. Principles of laser triangulation method.

The transformation equation for the presented triangulation method, which defines the deviation of the ring from the previously defined parameters, is given in the Eq. (1):

$$y_i = (x_i - x_1) \cdot k \tag{1}$$

Considering the Eq. (1) it is possible to calculate the movement of a ring (y_i) by knowing the parameters x_i (actual movement of a laser ray), x_1 (the extreme left position of the laser ray used for scale calibration) and transformation factor k, which can be calculated by using the Eq. (2) (see Fig. 4.2).

$$k = \frac{dy}{dx} \tag{2}$$

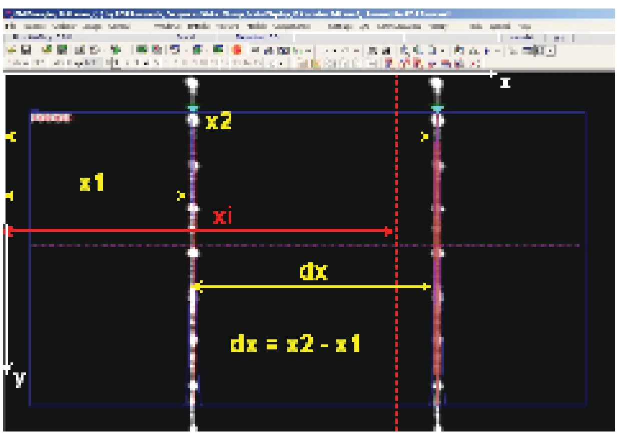

Figure 4.2. Main display: white laser lines on the ring surface captured by the camera.

The camera image, presented in the main display at the computer, is shown in Fig. 4.2. The laser ray, shown as a white vertical line, is moving right and left. For better presentation and understanding of the problem, two white lines are sketched on the screen (see Fig 4.2). They represent the extreme right and left position of the laser ray while the ring is rotating.

4.2 Theoretical description of the measuring point trajectory

The system, which is described above, needs to be ideal, which means:

- the rotating axle of rotating table is ideal without any oscillations,
- the welded ring and the rotating table are represented as rigid body.

First, the movement of the measuring point for the ideal circular ring has to be explained, where the centre of the ring is placed outside of the rotating axle. It is clear that in the industrial application it is impossible to place the welded ring exactly on the rotating axle.

When the ring is rotating, the centre of the ring is moving on the centre trajectory as shown in Fig. 4.3. For this case the laser line or the observed laser point movement on the ring is represented by Eq. (3), where $R_i(\alpha)$ represents the radii of the ring in the dependence from the rotating angle α.

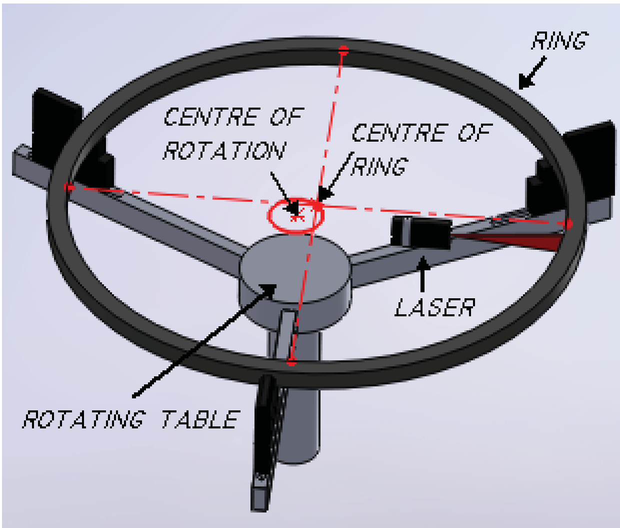

Figure 4.3. Ideal circular ring centred outside of the rotating axle.

$$R_i(\alpha) = E \cdot \cos\alpha_i + \sqrt{R_v^{\,2} - (E \cdot \sin\alpha_i)^2} \tag{3}$$

Legend: E - eccenter of ring [mm]
R_V - radius of ring [mm]
α - rotation angle [°]

In Fig. 4.4 the results of the points $R_i(\alpha)$, calculated by the Eq. (3), are presented graphically. In the next step the influence of the eccentric position of laser ray on the diameter value is explained. The critical situation appears only when the position of the laser is changed during the rotation of the ring (during the measuring process).

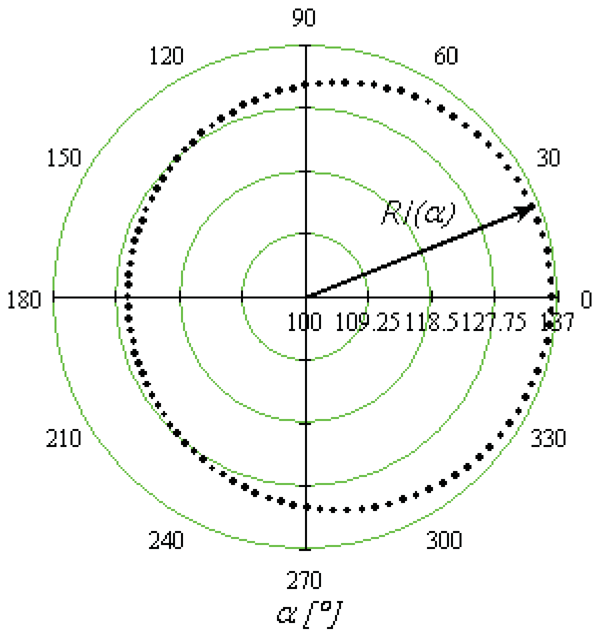

Figure 4.4. Sketched points $R_i(\alpha)$.

The eccentric position of the laser is shown in Fig. 4.5. If the laser position is changed for the distance $\pm z$, the radii value can be calculated by Eq. (4).

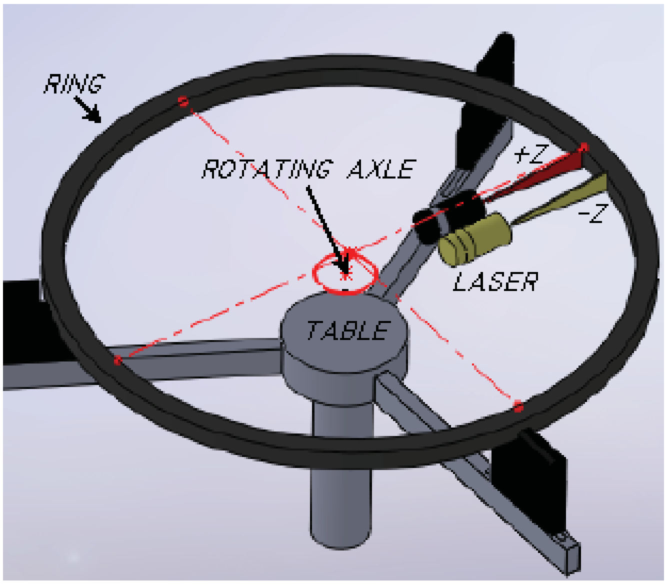

Figure 4.5. Eccentric position of the laser – influence on the diameter value.

$$R_z(\alpha) = E \cdot \cos\alpha_i + \sqrt{R_v^{\,2} - (E \cdot \sin\alpha_i - z)^2} \tag{4}$$

Legend: z - eccenter position of laser ray [mm]

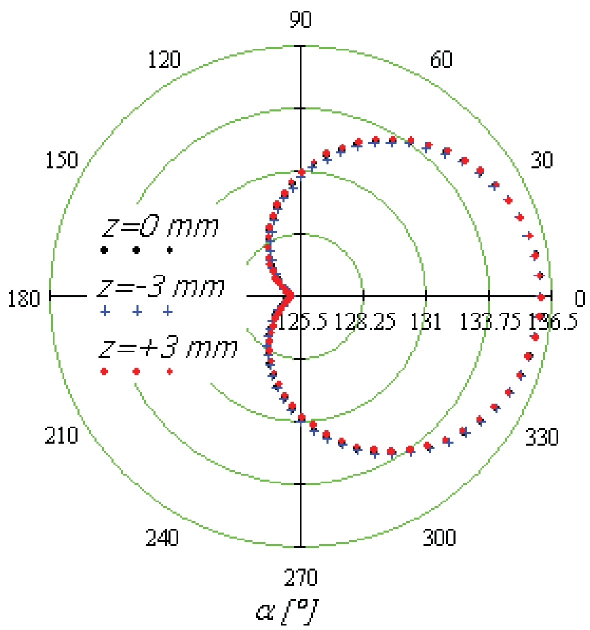

Figure 4.6. Comparison between the $R_i(\alpha)$ and the $R_z(\alpha)$.

Comparison of the calculated values of the diameter values $R_i(\alpha)$ and $R_z(\alpha)$ in the dependence on the rotating angle α is shown in Fig. 4.6.

4.3 Calculating the area and the geometrical centre of the measuring points of the ring

The main idea of the measuring algorithm is to calculate the area and the centre of this area, which is generated by measuring points, connected with lines. Knowing the velocity and the centre of the area, it is possible to eliminate the eccentric placement of the ring on the rotating table.

The curve is placed in *2D* plane, where the ∂A represents the edge of the area and A represents the inside of the observed area (see Fig. 4.7).

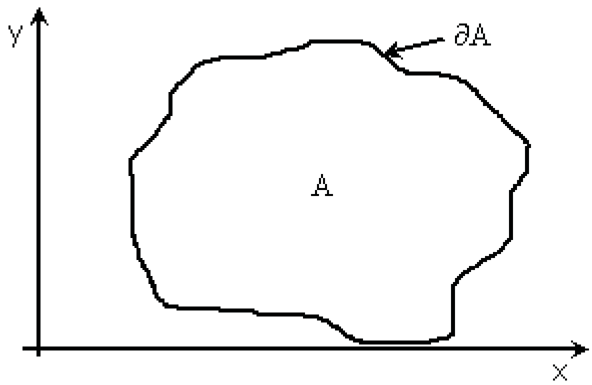

Figure 4.7. Area in x-y coordinate system.

If the area is constructed of points and connected together to create polygon (Fig. 4.8), the area A can be calculated by Eq. (5) (Marjetič, T., 2004).

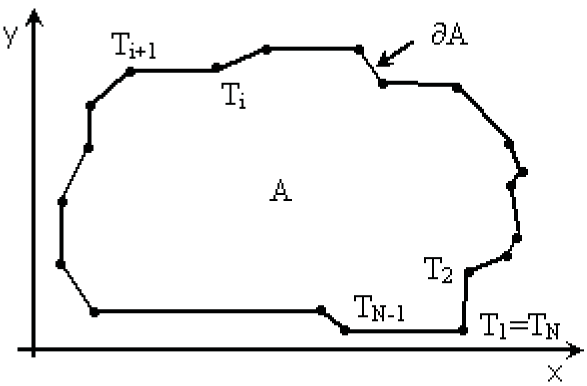

Figure 4.8. Area, constructed by lines with points on the corners.

$$A = -\frac{1}{2}\sum_{i=1}^{N-1}(x_{i+1} - x_i)(y_{i+1} + y_i) \tag{5}$$

Parameters x and y represent coordinates of the measuring point. The centre of the area (x_t , y_t) is calculated by Eq. (6) and (7) (Smith, L., 2006-2008; Borke, P., 1988).

$$y_T = \frac{S_x^*}{A} \tag{6}$$

$$x_T = \frac{S_y^*}{A} \tag{7}$$

S^*_y and S^*_x are static momentums of surface form around x and y axis, given by Eq. (8) and (9) (Smith, L., 2006-2008; Borke, P., 1988):

$$S_y^* = \frac{1}{6}\sum_{i=1}^{N-1}\left(x_{i+1}^2 + x_i \cdot x_{i+1} + x_i^2\right)\cdot\left(y_{i+1} - y_i\right) \tag{8}$$

$$S_x^* = -\frac{1}{6}\sum_{i=1}^{N-1}\left(y_{i+1}^2 + y_i \cdot y_{i+1} + y_i^2\right)\cdot\left(x_{i+1} - x_i\right) \tag{9}$$

5 Final mathematical algorithm examination

The mathematical measuring algorithm consists of six steps.

Step one: Grabbing the measuring points. The sketched points, shown in Fig. 5.1, represent the absolute movement of the laser line orientated on the ring's surface, which represents an eccentric placement and roundness of the welded ring. The equation of the laser triangulation is used:

$$y_i = \left(x_i - x_1\right)\cdot k \tag{10}$$

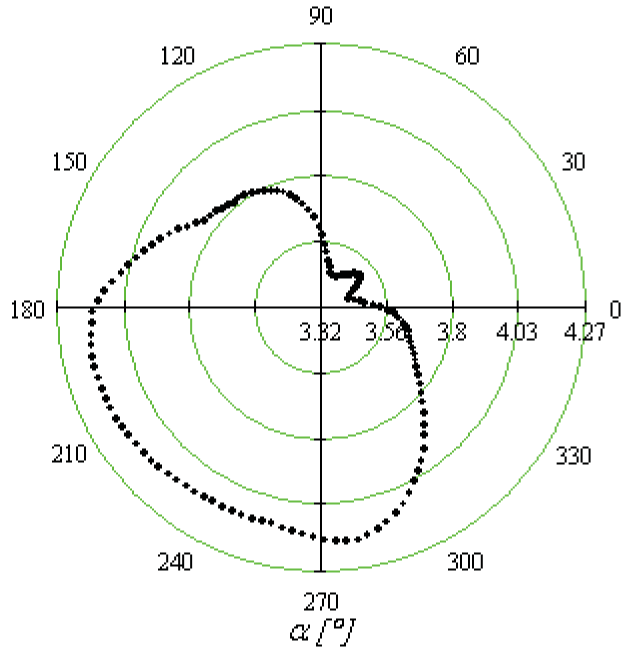

Figure 5.1. Measuring points.

Step two: The points are connected with lines and the radius correction *R*_offset is used (Eq. 11).

$$R_i = R\_offset + y_i \tag{11}$$

The correction gives us a regular value of the radius.

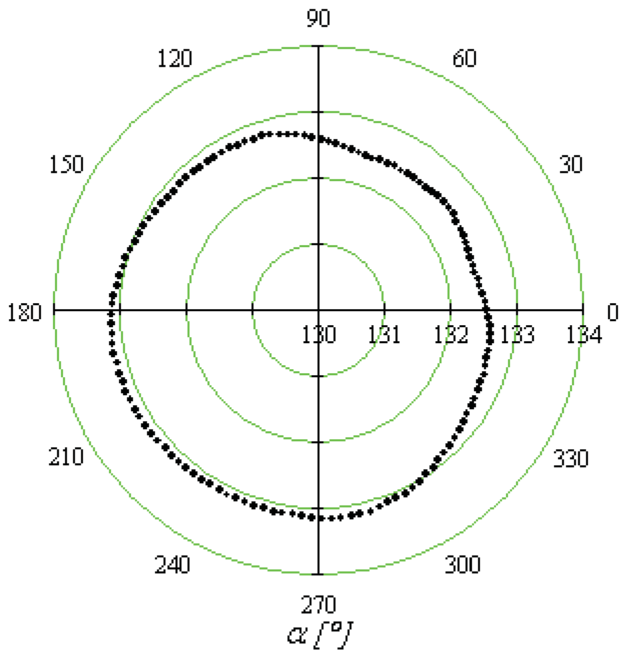

Figure 5.2. Corrected non centred points.

Step three: Calculating the centre of points by Eq. (6) and (7) given in chapter 4.3.

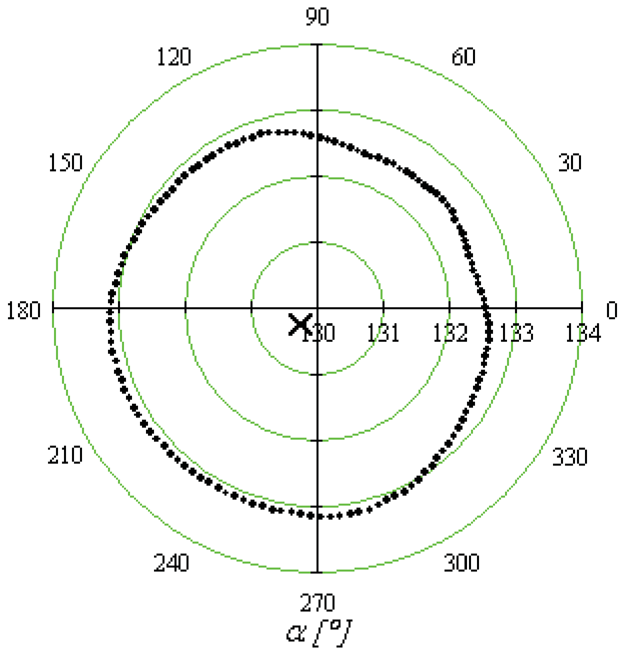

Figure 5.3. Centre of points.

Step four: Shifting the measuring points of the ring into the origin. The eccentric placement of the welded ring is herewith eliminated. Coordinates of the original point x_i and y_i are given with the following equations:

$$x_i(\alpha) = R_i \cdot \cos(\alpha_i)$$
$$y_i(\alpha) = R_i \cdot \sin(\alpha_i) \tag{12}$$

Where R_i presents radius i at the rotation angle α_i. Coordinates of the shifted points x_{vi} and y_{vi}:

$$x_{vi}(\alpha) = x_i(\alpha) - x_T$$
$$y_{vi}(\alpha) = y_i(\alpha) - y_T \tag{13}$$

Radius of the original points $R_i(\alpha)$:

$$R_i(\alpha) = \sqrt{(x_i(\alpha))^2 + (y_i(\alpha))^2} \tag{14}$$

Radius of the shifted points $R_{vi}(\alpha)$:

$$R_{vi}(\alpha) = \sqrt{(x_{vi}(\alpha))^2 + (y_{vi}(\alpha))^2} \tag{15}$$

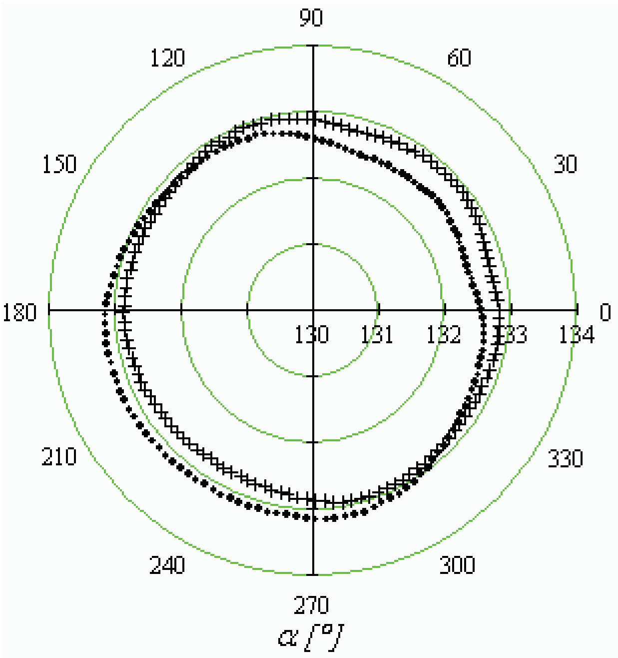

Figure 5.4. Original (cross) and shifted (point) points.

Step five: Calculating the average radius or diameter (shown as full curve in Fig. 5.5) and comparing it with measuring points transformed into curve (shown as hatched curve in Fig. 5.5).

$$R\_avg = \sqrt{\frac{A}{\pi}} \tag{16}$$

The parameter A represents the area calculated by the Eq. (5). The diameter of the ring is calculated as:

$$D_n = 2 \cdot R\_avg \tag{17}$$

Step six: Graphical presentation of ring curve and average diameter curve in one x-y graph.

Difference between the full and the hatched curve is given by Eq. (18) and is calculated for every single point of the ring circumference at the given angle α:

$$O(\alpha) = R_{vi} - R\_avg \tag{18}$$

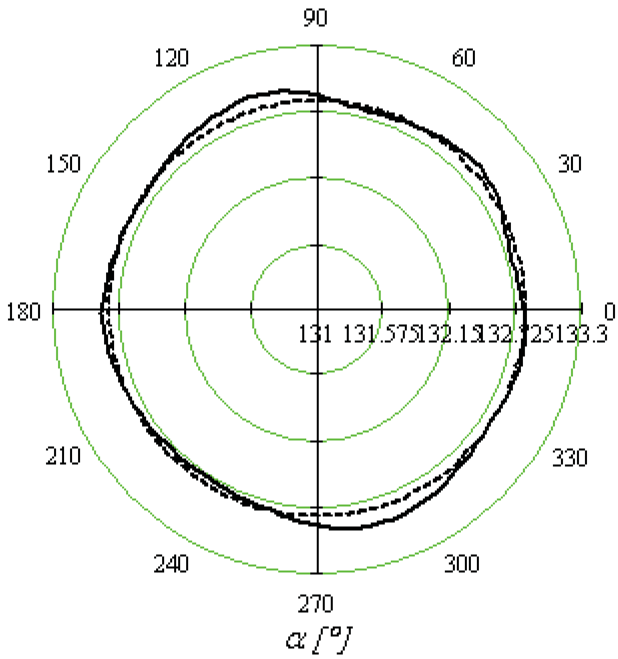

Figure 5.5. Average and ring diameter curves.

The minimum - O_{min} and the maximum - O_{max} difference between these two curves is used for calculating the roundness of the ring - O_v (J. W. Zhao and G. Q. Chen, 2005).

$$O_{\min}(\alpha) = \min(R_{vi} - R\_avg)$$
$$O_{\max}(\alpha) = \max(R_{vi} - R\_avg) \tag{19}$$

$$Ov = |O_{\min}(\alpha)| + |O_{\max}(\alpha)| \tag{20}$$

Graphic explanation of the ring roundness is shown in Fig. 5.5. Roundness of the ring, depending on the rotation angle α is shown in the Fig. 5.6.

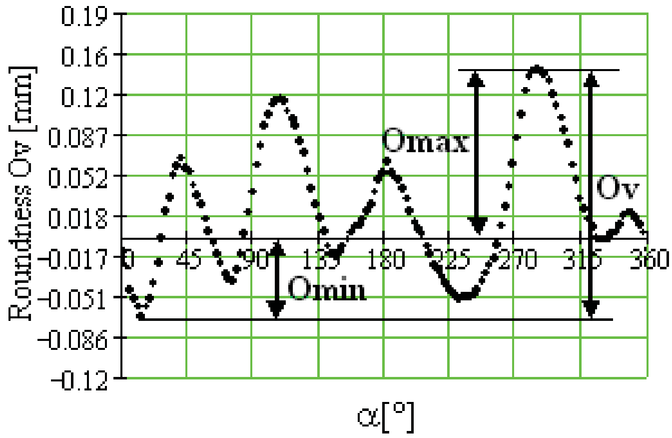

Figure 5.6. Roundness of ring depending on the rotation angle alfa α [°].

6 Experimental results

In our research the following experimental tests are used:
- the response of eccentric laser position,
- comparison of the results using regular and telecentric lens,
- repeatability of one part placed on a rotating table in different positions and the
- results comparison with other knowing parts.

Only the last two tests are presented in this paper's experimental results.

In this research the measuring results deviation of three systems, using the same basic mathematical algorithm, are compared. The first one is represented already as the theoretical system, where basic mathematical algorithm is used without any corrections. The MS Excel and MathCad programs are used for calculations and graphical analyzes.

Table 6.1: Results of the theoretical system

Measuring value [mm]	*Quality range [mm]*
Ring diameter	0.002 – 0.038 (0.02)
Ring roundness	0.018 – 0.053 (0.1)

The second system is represented as the experimental one, where basic mathematical algorithm is accomplished by necessary corrections for numerical program called Visual Basic for applications (Trdič F., 2000). The results, *quality range,* are given by Tab.6.1.

Corrections: Elimination of external vibrations by mechanical and numerical solution.

Table 6.2: Results of the experimental system

Measuring value [mm]	*Quality range [mm]*
Ring diameter	0.002 – 0.019 (0.02)
Ring roundness	0.005 – 0.045 (0.1)

The third system is represented as the industrial application, where all necessary corrections are used to improve the repeatability of results.

Table 6.3: Results of industrial application

Measuring value [mm]	*Quality range [mm]*
Ring diameter	0.005 – 0.01 (0.02)
Ring roundness	0.005 – 0.04 (0.1)

The graphical presentations of the results of the ring diameter and the ring roundness for all three systems are shown in Fig. 6.1 and Fig. 6.2.

The first graph in the Fig. 6.1 represents the repeatability of the ring diameter measurement and the second graph in the Fig. 6.2 represents the repeatability of the ring roundness measurement. The circular points show the measuring results for the theoretical system, the triangular points for the experimental system and the quadratic points for the final industrial system.

The hatched line in Fig. 6.1 and Fig. 6.2 shows the limit of good or bad, the suitable or unsuitable measuring system. A suitability criterion is given in the chapter 2.

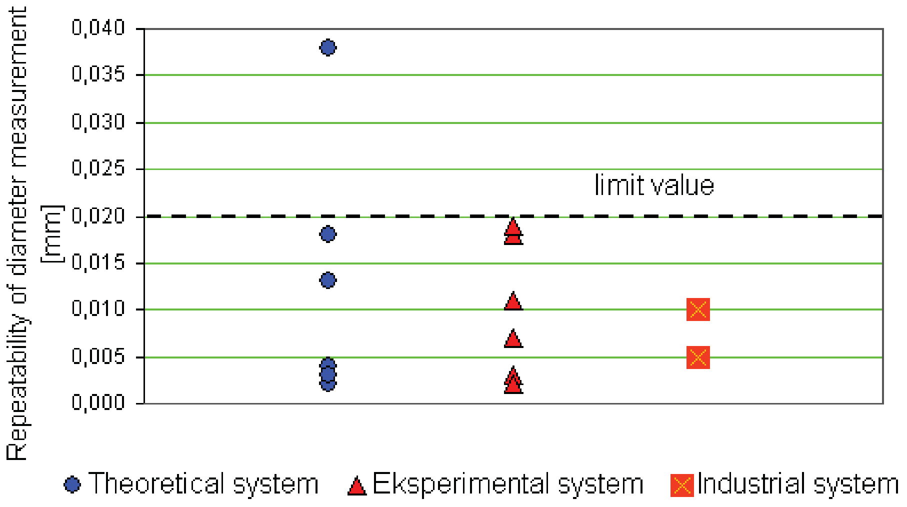

Figure 6.1. Repeatability of diameter measurement.

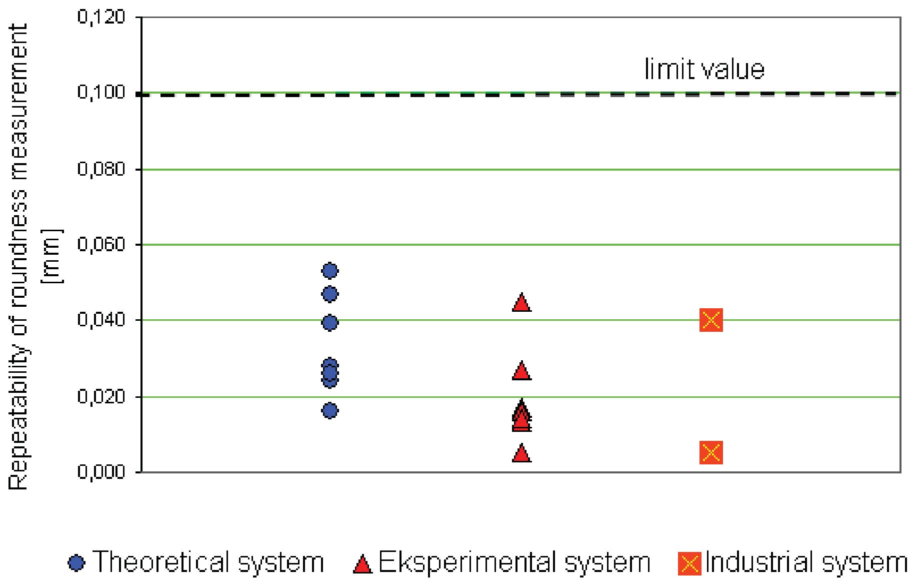

Figure 6.2. Repeatability of roundness measurement.

7 Conclusions

In the presented paper the research work is focused in the development of a mathematical - numerical algorithm, which is involved in modern robot vision measuring system. The machine vision experimental system for the ring diameter and ring roundness measurement was also developed.

The results enable a successful replacement of a manual (done by workers) quality control of welded rings by a machine vision control, which enables better efficiency and accuracy of the ring quality control process through the unlimited time period, independently of different subjective and objective disturbances. At the same time the machine vision control can help with the humanization of the pretentious labour filed, where the human work with the execution of the ring quality control would be much easier.

The experimental analysis of the results is presented for three systems. Their quality depends on the reliability of the repeatability of results. The theoretical system does not reach the customer’s request, so the system is not good enough for the direct industrial application. The experimental system comprises the improved theoretical algorithm, where the results of the repeatability are much better. This was the first step into introducing the reliable industrial system. The industrial system has better mechanical construction, its illumination has been proved and the measurement of outsides temperature is involved.

The experimental results prove that the quality control with introducing the machine vision into the measuring process of the welded ring depends on the right choice of the techniques and the type of mechanical components of the system, measurement algorithm and illumination of the object.

8 Acknowledgment

The experimental work was enabled by the company FSD Research (robot vision system producer) from Slovenia.

9 References

Borke, P., 1988; Calculatin The Area And Centroid Of A Polygon; July 1988

Braggins, D., 2006; Vision today for assembly automation, Assembly Automation 2, 6/2 (2006), p. 181 – 183.

Gruen A., 2001; Calibration and orientation of cameras in computer vision; Berlin, Springer, 2001

Hecht E., 1987; Optics; Addison-Wesley, 1987

Herakovič N., 2007; Computer and machine vision used in robotic assembly process, Journal of Mechanical Engineering, l. 53, 12/2007, str. 858-871

J. W. Zhao and G. Q. Chen, 2005; Roundness error assessment; Institute of physics Publishing, 13/2005

Marjetič A., Turk G., 2004; A geometric center of surface and body determination; Geodetski vestnik, 48/2004.

Pauli J., 2001; Learning – Based Robot Vision; Springer, 2001

Redford, Alan H., 1986:, Robots in assembly, Open University Press, 1986

Skvarč J., 2000; Solving an industrial problems using the machine vision as an universal applience, FDS Research

Smith G., Longley, 2006-2008; Polygon centroids and centres; Geospatial Analysis, 2006-2008

Trdič F., 2000; Vision Technologies and Neuro Inspectors Training Course, FDS Research

Trdič, F., 2006; Real industrial environment problems, http://www.fdsresearch.si

West P., 2006; A Roadmap for building a Machine Vision System; Automated Vision System, Inc.

Deformable and Rigid Objects Grasping

Mihai Stoica, Gabriela Andreea Calangiu and Francisc Sisak
Department of Automatics, “Transilvania” University of Brasov, Romania

Abstract
In this paper we consider the problem of real manipulation in a realistic environment – a flexible fabrication cell. In the first parts of the article are presented some methods for automatic grasp planning using a three-finger manipulator. Information presented here consist of a method for automatic grasp planning using shape primitives, a vision-based method used for grasping extruded objects and an algorithm used for grasping deformable objects. In the last section, is presented a general algorithm used for grasping deformable and rigid objects in flexible fabrication cells.

1 Introduction

Selecting a good grasp of an object using an articulated robotic hand is a difficult problem because of huge number of possibilities.

One way of limiting the large number of possible hand configurations is to use grasp pre-shapes. Before grasping an object, humans unconsciously simplify the task to selecting one of only a few different prehensile postures appropriate for the object and for the task to be performed. Medical literature has attempted to classify these postures into grasp taxonomies. Cutkosky and Wright (Cutkosky M.R., 1986) extended this classification to the types of grasps need in a manufacturing environment and examined how the talk and object geometry affect the choice of grasp.

A number of papers present contact-level grasp synthesis algorithms (Ding D., 2000; Ferrari C., 1992; Hester R.D., 1999; Itu A., 2007). These algorithms are concerned only with finding a fixed number of contact locations without taking into consideration the hand geometry.

Other systems built for use with a particular hand, restrict the problem to choosing precision fingertip grasps, where there is only one contact per finger (Hester R.D., 1999). These types of grasps are good for manipulating an object, but are not necessarily the most stable grasps because they do not use inner finger surfaces or the palm.

Most robotic systems currently in existence have been built under the assumption that manipulation of rigid objects remains the primary task. In reality though, many objects are non-rigid. Most are unsymmetrical, compliant, and have alterable shapes. Ayanna Howard and George Bekey developed an algorithm for handling of 3-D deformable objects. They defined a ‘3-D deformable object’ as an object whose three flexible degrees of freedom are characterized by viscoelastic interactions between molecules (Howard A.M., 2000).

Even for a simple three-fingered hand, such as the Barrett Hand, there are a total of 10 degrees of freedom: 6 degrees of freedom in placing the wrist relative to the object and 4 internal degrees of freedom which set the finger positions. More complex hands have even more possibilities. Of course, large portion of this 10 dimensional space are the worthless because the fingers are not in contact with the object, but even if the problem was re-parameterized, a brute force search would still be intractable (Itu A., 2008)

2 Shapes Primitives

An object can be approximated with a sphere, a cylinder, a cone or a box or with a sum of these. The names of these geometric forms are shapes primitives. By modeling an object as a set of shape primitives, we can use a set of rules to generate a set of grasp starting positions and pre-grasp shapes.

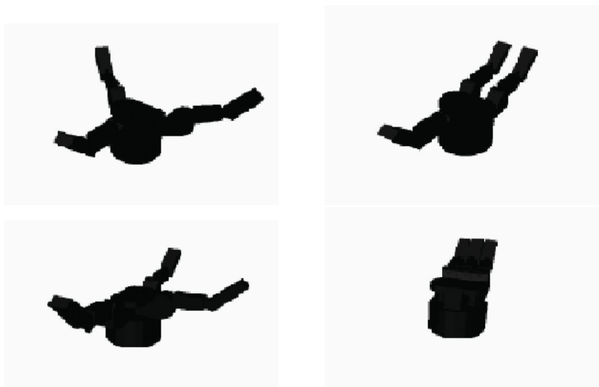

Fig. 2.1. Grasp pre-shapes for the Barrett hand: spherical, cylindrical, precision-tip, and hook grasps

Our service robot is outfitted with the relatively simple Barrett hand which has only 4 degrees of freedom. For this hand Miller et al. identified four distinct pre-shapes, shown in Fig. 1(Miller A., 2003).

The first step of the grasp planning processes is to generate a set of grasp starting positions. To generate a set of starting positions, the system requires a simplified version of the object's geometry that consists only of shape primitives such as spheres, cylinders, cones and boxes.

For each shape, they identified a set of grasping strategies to limit the huge number of possible grasps:

Spheres should be grasped with the spherical pre-grasp shape and the palm approach vector should pass through the center of the sphere.

Cylinders may be grasped from the side, or from either end. From the side grasp the cylindrical pre-grasp should be used. The grasp approach should be perpendicular to the side surface, and the thumb should either be perpendicular to the central axis of the cylinder, in order to wrap around it, or in the plane containing both the approach direction and the central axis, in order to pinch it at both ends. For the end grasp, the spherical pre-grasp should be used. The palm should be parallel to the end face and aligned with the central axis.

Cones can be grasped in the same ways as a cylinder. However, in the case of a cone with a large radius and small heath, the side grasps will be very similar to a grasp from the top. To handle this, we have added as set of grasps around the bottom rim of the cone, where the palm approach vector is aligned with the bisector of the angle between the bottom face and the side face.
Boxes should be grasped using the cylinder pre-grasp shape, such that the two fingers and the thumb will contact opposite faces. The palm should be parallel to a face that connects the two opposing faces, and the thumb direction should be perpendicular to the face it will contact.

3 Three-finger Grasp Synthesis of the planar objects using Vision

This chapter presents a practical approach for synthesizing three-finger grasps on planar unknown objects by means of vision. It is used visual perception to reduce the uncertainty and to obtain relevant information about the objects.

An important element of grasp synthesis is contact stability. *Contact stability* includes those aspects that involve the contact of a single finger against the surface of the object (Molares A., 2004).

First they need define a practical criterion that encompasses the contact stability constraints. This is the *finger adaptation criterion*. It evaluates the fitting of the gripper's finger against the object surface in terms of the estimated contact area. The criterion establishes that the object's surface curvature must not exceed a threshold $\hat{\alpha}$ (curvature threshold) for being considered stable. The contiguous regions on the contour that comply with the finger adaptation criterion are called *grasp regions*: those having curvature under $\hat{\alpha}$ for all their points. The grasp regions are determined by grouping consecutive points with absolute curvature below the curvature threshold $\hat{\alpha}$.

Finally, each grasp region is abstracted as a straight segment called *grasp region segment*. These segments are computed from the line defined by the minimal square fitting of the points of the region, bounded by the first and last points of the region. Ideally, it should be possible to approximate these regions as straight lines

The use of such an abstraction of grasp regions has important practical implications. First, the use of grasp regions discards those points with a high curvature, that is, with an unstable contact. And second, the use of grasp regions reduces the complexity of the problem of converting a contour composed, potentially, of hundreds of point, to a few grasp regions. This allows for the combinatorial techniques of the further stages to perform their computations in a reasonable amount of time.
For grasp synthesis Molares et al. defined the *force-closure criterion* with the goal of characterizing force-closure grasps using three fingers. The purpose of this criterion is to ensure that the gripper does not cause the object to slide due to a torque when it closes its fingers to grasp it. The evaluation of this criterion is based on the concept of *friction cone.*

A sufficient condition for reaching force-closure with three fingers is that the intersection of the friction cones of the three contact points is not empty, and that the unit normal vectors to the surface defined by the contact points *positively spans plane.* (Molares A., 2004).

Three vectors positively span the plane if any of them can be written as a positive combination of other two (see figure 3.1).

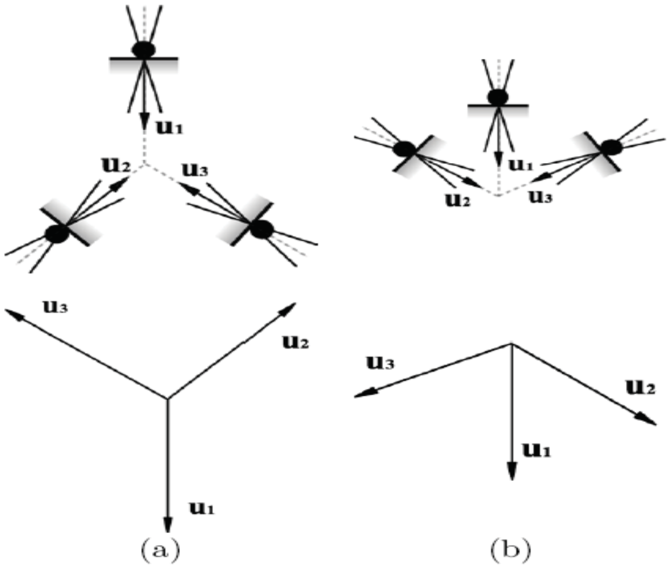

Fig. 3.1. The grasp (a) achieves force closure, whereas the grasp (b) does not

In a more formal way n vectors $u_i, i = 1...n$ span the plane if and only if:

$$\forall\, i, i = 1 \ldots n,\ \exists\ c_j > 0,\ u_i = \sum_{j=1, i \neq j}^{n} c_j u_j \qquad (3.1)$$

The goal when constraining a three-finger grasp is to find a configuration of the hand such that the positions of the three fingers is the same as in the original grasp, and the orientation of forces exerted by the fingers are similar. This problem can be very complex since the description of the configuration is composed by a lot of parameters that have to be determined. Antonio Morales and Pedro J. Sanz developed a procedure which consists of fixing the contact points of the hand configuration in the same location as the three-finger grasp. This, along with the constraints imposed with the hand kinematics, reduces the problem to a more tractable one.

4 Grasp Planning for Deformable Objects

For the problem of grasping for non-rigid objects, in the first step it must to calculate deformation characteristics for object and in the second step, it must calculate the minimum force required to successfully lift the object.

If F_w is the force required to lift a rigid object of weight W with frictional coefficient μ, we define the minimum deformable object lifting force L_f as $F_w + F_d$ where F_d is a minimum additional force term required to compensate for the deformation of the object.

At the sub-microscopic scale, all solid material is composed of atoms. Adjacent atoms in a solid exhibit both attractive and repulsive forces which keep the atoms at equilibrium distance from each other. Deformation of a material is caused at the microscopic level by visco-elastic interactions between atoms. This visco-elastic interaction can be modeled by the Kelvin Model which is characterized by a spring and damper in parallel. Zhao et al. have utilized this model and have characterized a deformable object as a set of particles locally interconnected by damped springs (Zhao X.C., 2008).

The mathematical model for deformable objects is presented in the following. Let $\overline{f}_n$ represent the external force applied to particle ψ_n. Let m_n represent the mass of the particle ψ_n. Let S_n represent the number of damped springs connected to particle ψ_n. Based on the mathematical equations defining the Kelvin Model, the forces acting on the nth particle are accumulation of external force, inertial force, damping force and spring force. Using Newton's law of motion, the partial differential equation of motion for the nth particle can be written as:

$$\sum_{i=1}^{S_n} m_n \frac{\partial^2 \Delta \overline{p}_{n,i}}{\partial t^2}(\overline{f}_n, t) + \sum_{i=1}^{S_n} \lambda_{n,i} \frac{\partial \Delta \overline{p}_{n,i}}{\partial t}(\overline{f}_n, t) + \sum_{i=1}^{S_n} D_{n,i} \Delta \overline{p}_{n,i}(\overline{f}_n, t) = \overline{f}_n \tag{4.1}$$

where D_n, the deformability coefficient, is a function of the force and the change in spring length, λ_n, the damping coefficient, is a function of the force and the instantaneous change in spring length, $\Delta\overline{p}_{n,i}$ represents the change in spring length in each Cartesian direction, and $\frac{\partial \Delta \overline{p}_{n,i}}{\partial t}(\overline{f}_n, t)$ represents the instantaneous change in spring length.

From equation 4.1, we see that the only parameters which are not directly defined as a function of time are the mass, deformability, and damping coefficients. If we assume that the mass of the object is given, then we can classify the overall deformation of the object in terms of the deformability function D and the damping function λ. For determining the deformability function are used the following steps:

1. Apply a force against the object's surface. At time $t_m = t_0, t_1, ..., t_n$, record the force $\overline{f}(t_m)$
2. Calculate the particle displacement vector $\overline{d}(\overline{f}(t_m), t_m)$ for all $t_m \in t$
3. The deformability function is $D(\overline{f}, \overline{d}) = \frac{\overline{f}(t_m)}{\overline{d}(\overline{f}(t_m), t_m)}$ for all $t_m \in t$

The damping function is determined in the same mode. The difference is that here is calculated the particle displacement velocity vector.

To learn the characteristics of an adequate grasp, we must determine the relationship between mass, deformation and force. The steps required to handle manipulation of 3-D deformable objects are as follows:

1. Record dimensions of a known object
2. Calculate the deformability and damping functions
3. Determine the minimum force necessary to grasp known object by iteratively lifting object
4. Links object attributes and grasping force into an index table.

5 Algorithm used for grasping deformable and rigid objects

5.1 General requirements for using efficiently the algorithm

This algorithm is used for grasping objects in a flexible cell, where should be placed a robot arm. This robot arm has attached a three-finger manipulator. Near this cell must be placed the conveyor. On the conveyor's pallets deformable and non-deformable objects must be placed. The robot must grasp these objects and place them, for example into storage. Each pallet must have a certain code; some of these codes are used for identifying deformable objects and the other are used for identifying the rigid ones. Using the codes of the pallets the robot knows that the object which must grasp is deformable or rigid. In this cell must be placed a vision system with two cameras and a laser sensor. The vision system helps robot to detect objects contour, locate it and extract some features to match with predefined grasping models.

5.2 The algorithm used for grasping

The algorithm has two important parts. The first one consists in learning an adequate grasp for deformable objects. The grasping for non-deformable objects does not need to be learned. The second part is, in fact, grasping of objects.

The steps for learning an adequate grasp for deformable objects are presented below:

1. Determine deformability and damping coefficient for the deformable object which must be grasped. These coefficients are computed in the mode presented in the 4th section.
2. Determine the minimum force necessary to grasp known object by iteratively lifting object.
3. Weight the object with a balance placed under the conveyor's belt.
4. Memorize, into an index table, the relationship between mass, deformability, damping and force required for lifting.
5. Resume the algorithm from the first step and learn this relationship for the objects made from the same material, but with the different weight. After that it can be determined a characteristic between mass and force (damping and deformability are known). Using the interpolation, we have to compute the lifting force, for a certain type of object after we know the mass of the object.
6. Resume the algorithm from the first step for all types of deformable objects.

If we learn to grasp all deformable objects we can pass to the last part of algorithm: the effective grasping. The grasping steps of the objects are presented below:

1. Read the code of pallet and establish what type of object is, deformable or non-deformable.
2. If the object is deformable then go to the next step. If the object is non-deformable one, then give to the force-closure of the gripper the maximal value and, after that, go to step 7.
3. Weight the object.
4. Use the mode presented in the 4th chapter for determine the deformability and damping coefficient.
5. For known mass, deformability and damping coefficients, extract the lifting force from the index table.
6. Give the force-closure this value.

7. Using the vision system to determine if the object is an extruded one or have a shape similarly with shapes primitives presented in the 2nd chapter.
8. If it is an extruded one go to the next step. If not, go to the step 13.
9. Measure the object's height with a laser sensor and establish the grasp height at 2/3 of object's height from for the object with them height less than a predefined value or to a predefined height value for the rest of the objects.
10. Determine grasp regions from the 2D image of the object.
11. Take a combination of three regions and verify if these regions offer a stable grasp. If this is a good one, grasp the object using the gripper kinematics and the computed lifting force. Then, go to the step 15. If is not stable go to the step 12.
12. Go to the step 10.
13. Determine which primitive shape can be used.
14. Grasp the object using the determined primitives shape on the step 13, compute lifting force and gripper kinematics. Go to the next step.
15. Finish.

6 Conclusions

Grasping has a great relevancy in the context of robotics field. The results of the actions performed depend of the accuracy and the precision of grasping. Objects have different forms and can be rigid or deformable. For the rigid objects the grasping problem is not so complicated, but for the deformable objects the problem of lifting force determination is not so simple. It requires that the deformability and the damping coefficients to be previously calculated.

The algorithm presented in the preview chapter is a general algorithm used for grasping objects. Until now, we have not tested this algorithm; its testing is for our future work. The algorithm gathers, in a simple logic scheme, the methods for different type of grasping. With this algorithm, the system (the equipment) can grasp many types of objects; the only constraint is that the robot must know if the object is deformable or non-deformable. For a deformable object, after the system learns an adequate grasp, it can compute, in a very simple mode, the lifting force. It must determine the deformability and damping coefficients and from the index table it must extract the lifting force. With the vision system the robot can extract the object features and can establish what type of grasp to use.

ACKNOWLEDGEMENT
This paper is partially supported by the Sectoral Operational Programme Human Resources Development (SOP HRD), financed from the European Social Fund and by the Romanian Government under the contact number POSDRU/6/1.5/S/6, and partially supported by CNCSIS ID-775 project.

7 References

Cutkosky M.R. and Wright P.K.. 1986. Modelling manufacture grips and correlation with the design and robotic hands , *Proceedings of the 1986 IEEE International Conference on Robotics and Automation*, pp.1533-1539.

Ding D., Liu Y.H. and Wang S..2000. Computing 3-D optimal form closure grasps, *Proceedings of the 2000 IEEE Conference on Robotics and Automation*, pp.3573-3578.

Ferrari C. and Canny J.. 1992. Planning optimal Grasps, *Proceedings of the 1992 IEEE International Conference on Robotics and Automation*, pp.2290-2295.

Howard A.M. and Bekey G.A... 2000. Intelligent Learning for Deformable Object Manipulation, *Journal: Autonomous Robots*, Springer Netherlands, Vol. **9,** pp.51-58.

Hester R.D., Cetin M., Kapoor C. and Tesar D.. 1999. A criteria-based approach to grasp synthesis, *Proceedings of the 1999 IEEE International Conference on Robotics and Automation*, pp.1255-1260.

Itu A., Beraru A. and Staretu I.. 2007. Developing Grasping Preshaping in Virtual Environment Based on Real Object Shape Analysis, *ISI Proceedings: Virtual Reality Applications and Tools for Intelligent Manufacturing Systems*.

Itu A., Staretu I. and Danciu G.. 2008. Automatic Grasp Planning Using Grasping Strategies, *Proceedings of 4th International Conference on Robotics*, Vol. 15(50), pp.407-412.

Miller A., Knoop S., Christensen H. and Allen P. 2003. Automatic Grasp Planning using Shape Primitives, *ICRA 2003*, pp.1824-1829.

Morales A., Sanz P., Pobil A. and Fagg A.. 2004. Vision-based three-finger grasp synthesis constrained by hand geometry.

Zhao X.-C., Lei Y. and Zhou J.-P.. 2008. Strain analysis of nonlocal viscoelastic Kelvin bar in tension, *Editorial Committee of Appl. Math. Mech. And Springer-Verlag*, Vol. **29(1)**, pp.67-74.

Popov Stability under Uncertainty Contours

Alexander Weinmann, OVE, Senior Member IEEE
Vienna University of Technology, Institute of Automation and Control
Gusshausstrasse 27-29/376, A-1040 Vienna / Austria
Phone: +43 1 58801 37611, Fax: +43 1 58801 37699
email: weinmann@acin.tuwien.ac.at

Manuscript received April 14, 2010

Abstract

The paper addresses an extension of the classical Popov absolute stability criterion in the presence of a two-parameter structured uncertainty in the linear part of the control system. A general two-dimensional contour bound in the plane of uncertain parameters is taken into consideration.

Keywords: Popov sector, absolute stability, SISO systems, two-parameter uncertainty

1 Introduction. Classical Popov Criterion for Nominal Systems

The stability criterion of Popov is a sufficient criterion to detect absolute stability (*Popov, V.M., 1973*). There is an extensive bibliography of this topic (*Aiserman, M.A., and Gantmacher, F.R., 1965; Vidal, P., 1969; Cremer, M., 1995; Hsu, J.C., and Meyer, A.U., 1986; Liao Xiaoxin, 1993; Föllinger, O., 1993; Unbehauen, H., 1983; Adamy, J., 2009*) with many extensions, back to early days, e.g. *Desoer, C.A., 1965*. Uncertainties are taken into consideration via a set of corner points of the interval family in the literature, e.g., *Bhattacharyya, S.P., Datta, A., and Keel, L.H., 2009*.

For a system in Fig. 1, a linear part with transfer function $L(s)$ and a nonlinear part with characteristics $u(e)$ in a sector $(0,\ K)$, $\varepsilon < \frac{u(e)}{e} < K$, are taken into consideration. Stability in the Popov sense is guaranteed in sufficient sense if for any positive number q

the inequality

$$\Re e\left[(1+q\ j\ \omega)L(j\omega)\right] > -\frac{1}{K} \qquad \forall\ \omega \geq 0 \tag{1}$$

holds.

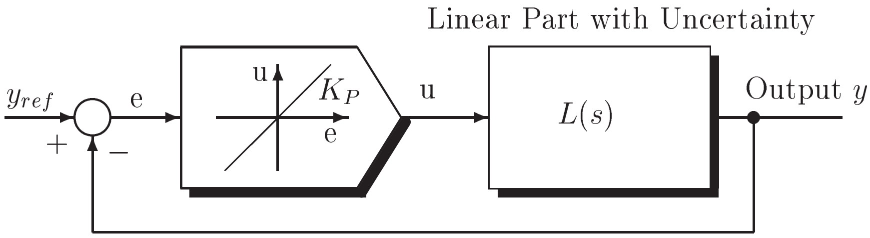

Figure 1: Nonlinear element with a sector-oriented nonlinear characteristic and a linear part of the control system with contour-oriented uncertainty. K_P is the critical gain K.

From Eq.(1),

$$p_P(\omega) \stackrel{\triangle}{=} \underbrace{\Re e\ L(j\omega)}_{\xi} - q\,\underbrace{\omega \Im m\ L(j\omega)}_{\eta} + \frac{1}{K} > 0\ . \tag{2}$$

Further definitions are the

$$\text{Popov line} \qquad \xi - q\eta + \frac{1}{K} = 0 \tag{3}$$

and the

$$\text{Popov polar plot} \qquad L_P(j\omega) \stackrel{\triangle}{=} \Re e\ L(j\omega) + j\omega \Im m\ L(j\omega)\ . \tag{4}$$

The Popov line intersects the real axis at $(-\frac{1}{K}, 0)$ with an ascent of $\tan\alpha = \frac{1}{q}$. The Popov polar plot $L_P(j\omega)$ results from the linear system frequency response polar plot $L(j\omega)$ with equal real part and an imaginary part stretched with a factor corresponding to the angular frequency ω. Any characteristic inside the sector is admissible, definite and continuous. All the poles of $L(s)$ are in the left s-half-plane. If a single pole is located at the imaginary axis, then $\varepsilon > 0$ is required.

If $\Re e\ L(j\omega) > -\frac{1}{K}$ is satisfied for all $\omega \geq 0$, this is sufficient to a higher extent: $q = 0$ corresponds to an infinite slope of the Popov line.

From Eqs.(3) and (4), the Popov criterion alternative is: The Popov polar plot $L_P(j\omega)$ must be located to the right of the Popov line. [Comparison of Popov function and Popov line, Eq.(2) and Eq.(3), leads to the following basic facts: (1) Equating $\eta = \Im m\ L_P$ in horizontal direction requires $\Re e\ L_P > \xi$ referring to "> 0" in the Popov condition.

(2) Equating $\xi = \Re e\ L_P$ in vertical direction requires $\Im m\ L_P < \eta$ referring to "> 0" in the Popov condition once more.]

For a linear system with integral behavior, the geometric figures are depicted in Fig. 2, namely in the case of critical stability bound. Correspondingly, the function $p_P(\omega)$ is portrayed in Fig. 3.

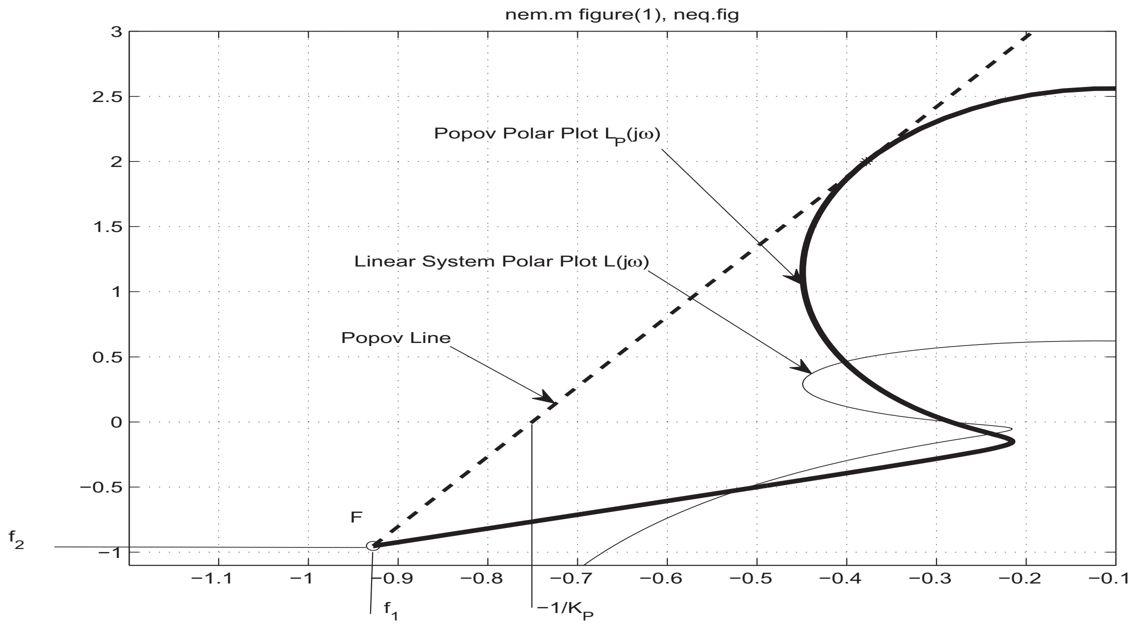

Figure 2: Complex plane with classical Popov figures with data from Example 1

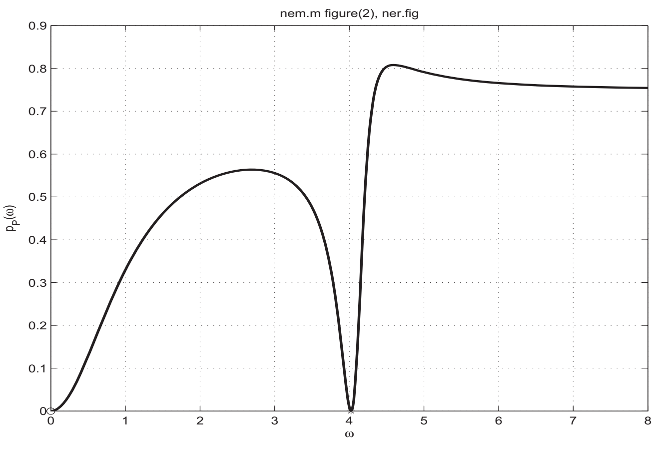

Figure 3: Real function $p_P(\omega)$ for data of Example 1

In general, the Popov line is characterized by two tangent points. In the critical stability point, the Popov line is tangential to $L_P(j\omega)$. In the case of integral linear part of Fig. 2, there are three points of interest: The initial point F at $(f_1,\ f_2)$, the tangent point

$(\Re e\ L_P(j\omega), \Im m\ L_P(j\omega)\ )$ and the slope $\frac{1}{q}$. Hence,

$$\frac{1}{q} = \frac{\dfrac{\partial \Im m\ L_P(j\omega)}{\partial \omega}}{\dfrac{\partial \Re e\ L_P(j\omega)}{\partial \omega}} = \frac{\Im m\ L(j\omega) + \omega \Im m\ L_d(j\omega)}{\Re e\ L_d(j\omega)} \stackrel{\triangle}{=} \frac{\Im m\ \{L_P(j\omega)\} - f_2}{\Re e\ \{L_P(j\omega)\} - f_1}\ , \tag{5}$$

where $L_d \stackrel{\triangle}{=} \frac{\partial L(j\omega)}{\partial \omega}$, $\Re e\ L_d(j\omega) = \frac{\partial \Re e\ L(j\omega)}{\partial \omega}$, $\Im m\ L_d(j\omega) = \frac{\partial \Im m\ L(j\omega)}{\partial \omega}$.

From Eq.(5),

$$v_P(\omega) \stackrel{\triangle}{=} [\omega \Im m\ L(j\omega) - f_2] \Re e\ L_d(j\omega) - [\Re e\ L(j\omega) - f_1][\Im m\ L(j\omega) + \omega \Im m\ L_d(j\omega)]\ . \tag{6}$$

Equating $v_P(\omega) = 0$ leads to ω_o. For pointwise use of the uncertainty contour c, see Section 2, the extreme slope is the solution.

For another type of linear proportional systems with two humps in the Popov polar plot, the Popov line can be modified. Two presumable lines L_{H1} and L_{H2} are used, see Fig. 4. Instead of F, select an arbitrary point H in the complex plane. Reuse Eq.(6) both for L_{H1} and L_{H2}. Modify H in order to reduce the angle κ. For $\kappa = 0$ one has $L_{H1} = L_{H2} = L_P$.

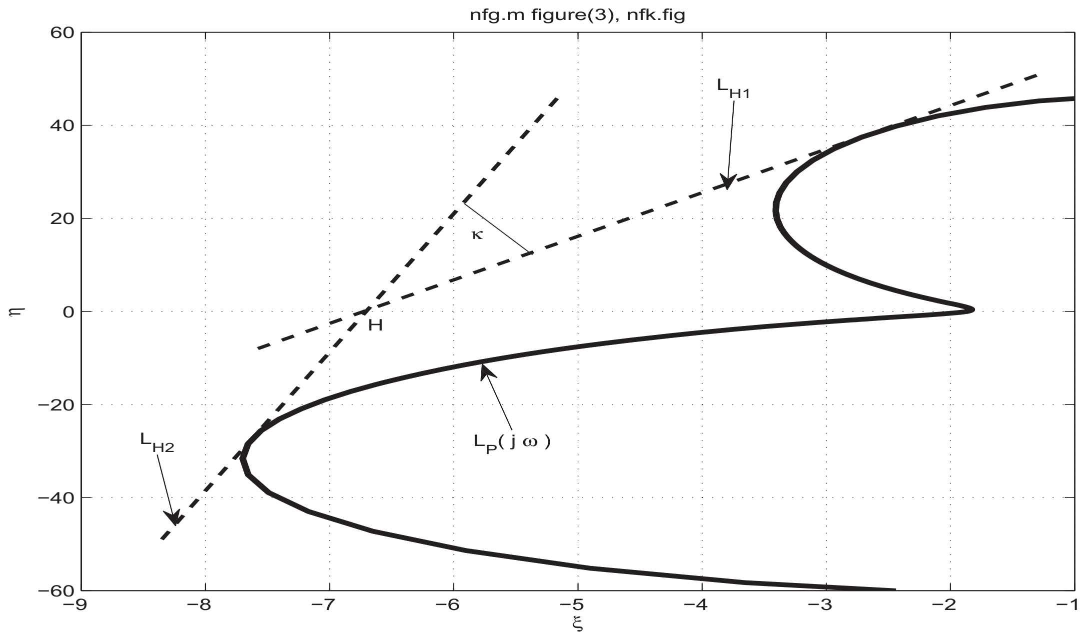

Figure 4: Approximation for a Popov polar plot with two humps

2 Linear System with Structured Uncertainty

For a perturbed linear system, we select a two-dimensional uncertainty contour. A vector norm $\|\binom{\gamma}{\delta}\|_{n_r} \triangleq [\gamma^{n_r} + \delta^{n_r}]^{1/n_r}$ is used with n_r an even integer; to cover an entire cycle, $0 \leq \alpha_c \leq 2\pi$ is considered (*Weinmann, A.; 2010*). In Fig. 9, the uncertainty contour in a tilted version is shown. The contour is the bound for all the uncertainties in the parameter plane. The uncertainty-driven contour c around the nominal $L_P(j\omega)$ is checked for each frequency ω. Using the revolution parameter α_c (within the contour c, Fig. 5), the touching condition requires

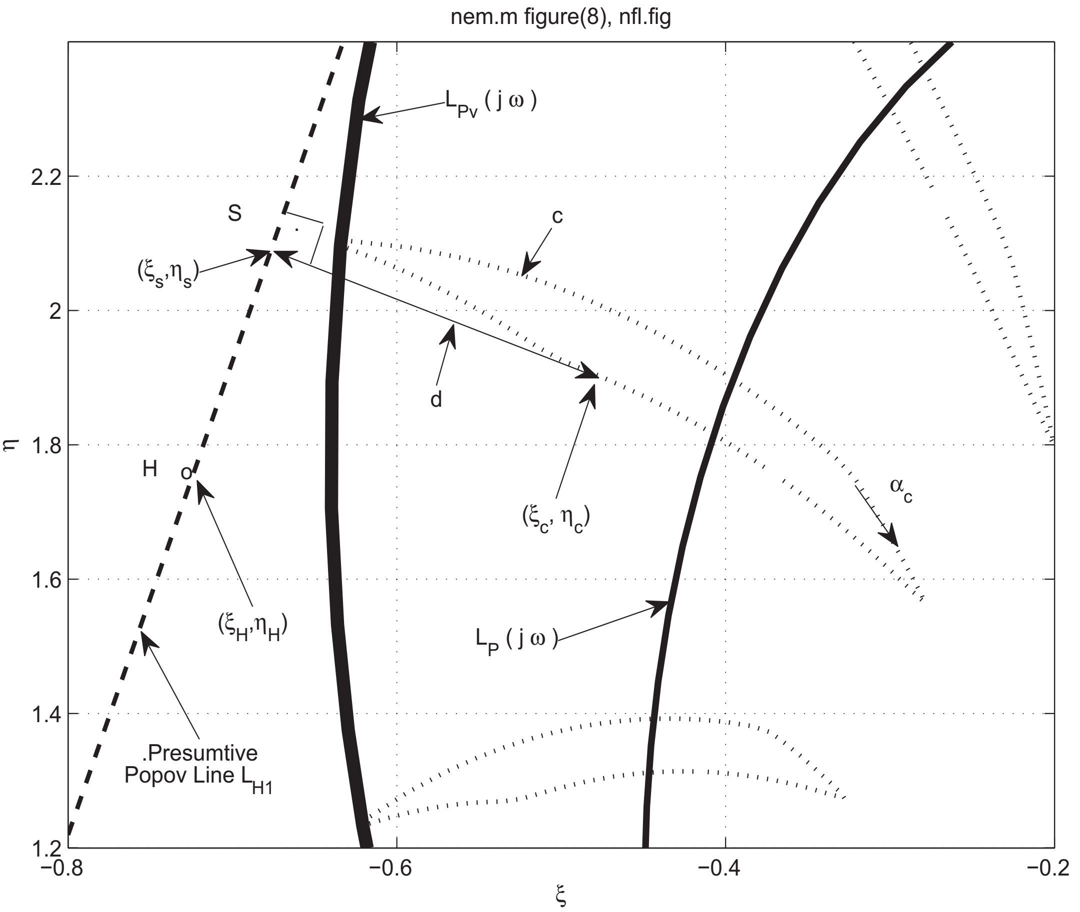

Figure 5: Minimum search versus Popov line

$$\lim_{d\to 0}\ \lim_{\kappa\to 0}\ \min_{\omega}\ \inf_{\alpha_c} d(\alpha_c,\ \omega), \tag{7}$$

where d is the distance perpendicular to the Popov line with slope $1/q_v$. The additive index v stands for the perturbation. The slope parameter q_v and the coordinates $(\xi_H,\ \eta_H)$

are unknown up to the final step of minimum search for $\kappa \doteq 0$, $d \doteq 0$. For a given uncertainty contour, Eq.(7) yields an analytic detection with zero differential quotients; if it is too complicated, numerical search is preferred (*Weinmann, A., 2010a*). The Eqs.(7) and (6) must be solved alternately. In between, $\kappa \to 0$ is executed. The process usually converges rapidly due to the geometric constellation. The perturbed Popov plot $L_{Pv}(j\omega)$ in Fig. 5 is

$$L_{Pv}(j\omega) \triangleq L_P(j\omega, c, \alpha^\star) \quad \forall \alpha_c^\star = \arg\min_{\alpha_c} \ d \ , \tag{8}$$

where d refers to Eq.(11).

The minimum search outline is as follows. Following Fig. 5, the presumptive Popov line L_{H1} and a perpendicular line obey

$$(\eta - \eta_H) = (\xi - \xi_H)\frac{1}{q} \qquad \text{and} \qquad (\eta - \eta_c) = -q(\xi - \xi_c) \ . \tag{9}$$

The intersection of these lines yields

$$\xi_s = \frac{(\eta_c + q\xi_c - \eta_H)q + \xi_H}{1+q^2} \qquad\qquad \eta_s = (\xi_s - \xi_H)\frac{1}{q} + \eta_H \tag{10}$$

$$\rightsquigarrow \quad d^2 \ = \ (\xi_s - \xi_c)^2 + (\eta_s - \eta_c)^2 \ \to \ 0 \ . \tag{11}$$

3 Example 1. IT$_{3s}$-Linear Part

Consider the linear part of the control system

$$L(s) = \frac{1}{s(s+a)(1 + \frac{2D}{\omega_N}s + \frac{1}{\omega_N^2}s^2)} \ . \tag{12}$$

For $s = j\omega$, note the following limes values

$$\lim_{\omega \to 0} \Re e \ L_P(j\omega) \ = \ \lim_{\omega \to 0} \Re e \ L(j\omega) = -\frac{2D}{a\omega_N} - \frac{1}{a^2} \triangleq f_1 \tag{13}$$

$$\lim_{\omega \to 0} \Im m \ L_P(j\omega) \ = \ -\frac{1}{a} \triangleq f_2 \ . \tag{14}$$

In Fig. 2, the intersection of the Popov line with the negative real axis is at $(-\frac{1}{K_P}, \ 0)$ where $K_P = -\frac{1}{f_1 + q/a}$. Hence, the complex Popov polar plot $L_P(j\omega)$ starts at an ultimate point F with coordinates $(f_1, \ f_2) = (-\frac{2D}{a\omega_N} - \frac{1}{a^2}, \ -\frac{1}{a})$ and just touches $L_P(j\omega)$ for $K = K_P$. The Popov line is $(\eta - f_2) = (\xi - f_1)\frac{1}{q}$.

In Fig. 6, zeroing Eq.(6) is illustrated.

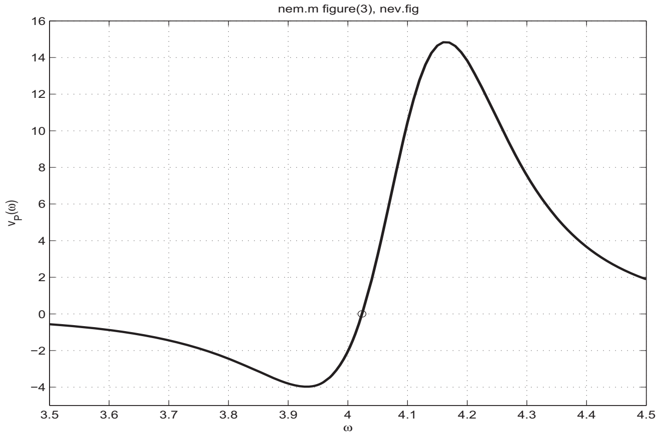

Figure 6: Illustrating the tangent condition of the zeros of Eq.(6)

Now, perturbations of a and D are considered, a by γ and D by δ. In Fig. 7, the Popov polar plot including uncertainty contours c is depicted. The corresponding $p_P(\omega)$ is given in Fig. 8.

In Fig. 10 the uncertainty contours of Fig. 9 in superposition to the nominal $p_P(\omega)$ are uncoiled versus parameter α_c. The uncertainty contours for the critical stability point are enlarged in width.

The slope of the Popov polar plot at an arbitrary ω results from

$$g \triangleq \frac{\dfrac{\partial \Im m\ L_P(j\omega)}{\partial \omega}}{\dfrac{\partial \Re e\ L_P(j\omega)}{\partial \omega}} = \frac{\Im m\ L + \omega \Im m\ L_d(j\omega)}{\Re e\ L_d(j\omega)} \ . \tag{15}$$

The ascent of the real Popov function

$$\frac{\partial p_P(\omega)}{\partial \omega} = \Re e\ L_d - q \Im m\ L - q\omega \Im m\ L_d \tag{16}$$

is zero both at 0 and ω_o.

All the parameters involved in Example 1 are concatenated in the sequel:

$D = 0.045$; $a = 1.05$; $\omega_N = 4.1$; $\omega_o = 4.0238$; $n_r = 20$; $K_P = 1.3323$; $q = 0.1862$; $K_{Pv} = 1.0309$; $q_v = 0.1418$; $f_1 = -0.9279$; $f_2 = -1/a = -0.9524$; $g(\omega = 0) = 1.05$; $g(\omega_o) = 5.37$.

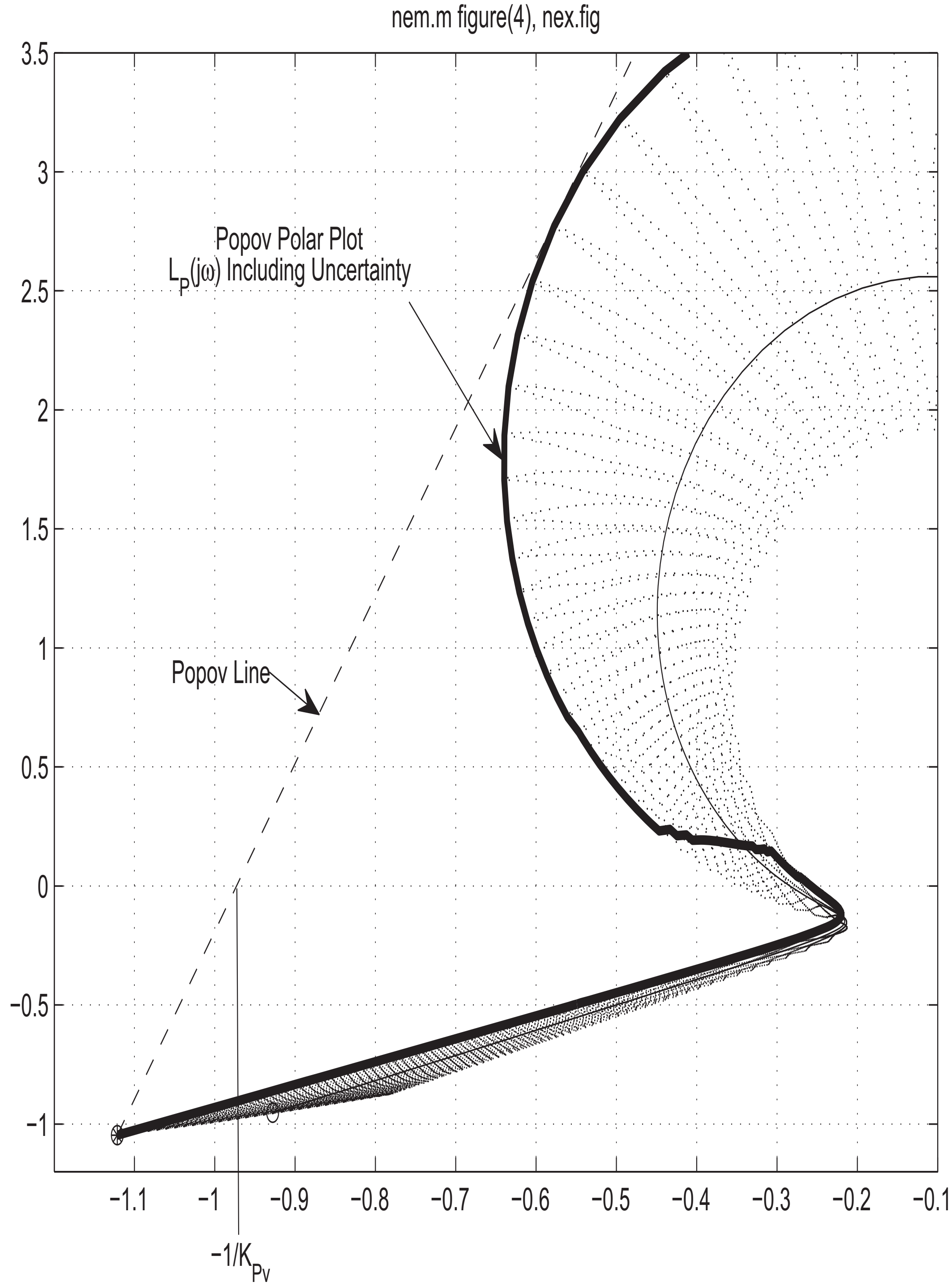

Figure 7: Popov polar plot including uncertainty

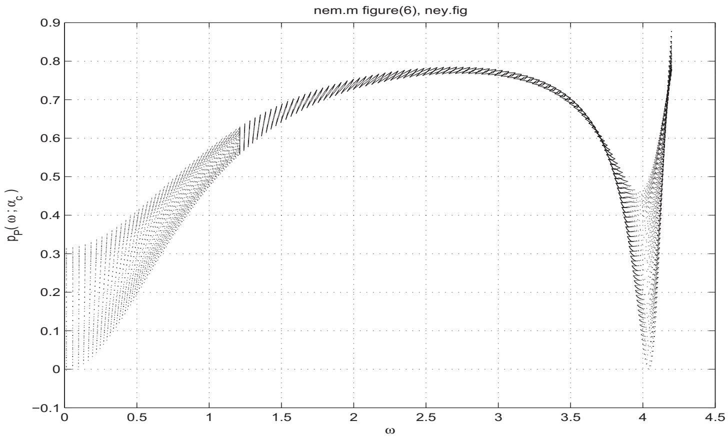

Figure 8: Function $p_{Pv}(\omega)$ including uncertainty

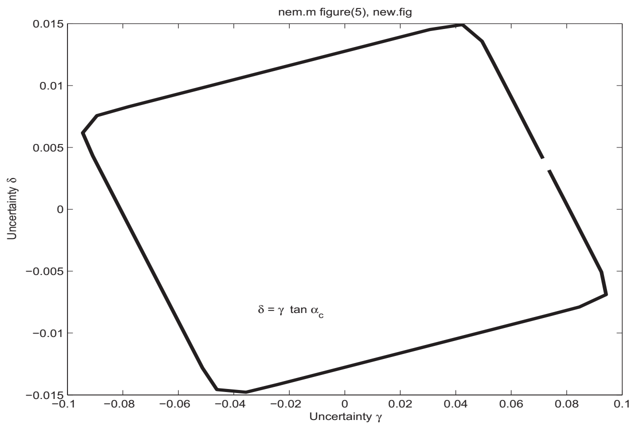

Figure 9: Uncertainty contour

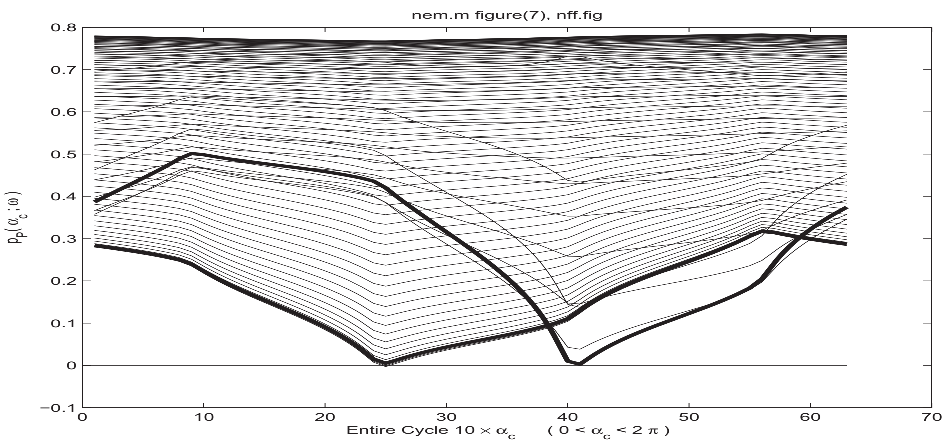

Figure 10: Uncoiled uncertainty contours

4 Example 2. PT$_{4s}$ Linear System

Now, consider the linear part of the control system

$$L(s) = \frac{1}{1 + \dfrac{2D_1}{\omega_{N_1}}s + \dfrac{1}{\omega_{N1}^2}s^2} \quad \frac{1}{1 + \dfrac{2D_2}{\omega_{N2}}s + \dfrac{1}{\omega_{N2}^2}s^2}\ . \tag{17}$$

In Fig. 11, the nominal Popov polar plot $L_P(j\omega)$ is given. In Fig. 13 the corresponding $p_P(\omega)$ is shown. The parameters D_1 and D_2 are additively perturbed by δ, and ω_{N1} and ω_{N2} by γ, following Fig. 9. The perturbed Popov polar plot is portrayed in Fig. 12.

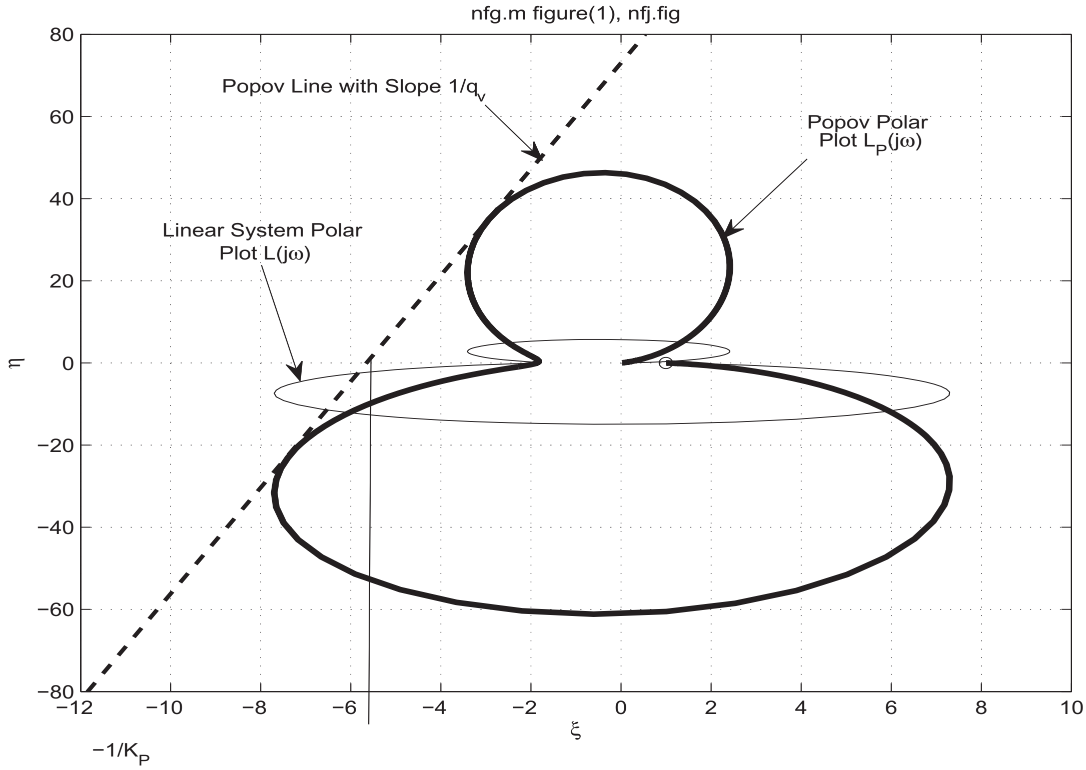

Figure 11: Nominal Popov polar plots for Example 2

The parameters involved in Example 2 are $D_1 = 0.045$; $D_2 = 0.03$; $\omega_{N1} = 4.1$; $\omega_{N2} = 8.1$; $q = 0.077$; $q_v = 0.0545$; the critical slopes without and with uncertainty are $K_P = 0.1786$; $K_{Pv} = 0.1111$.

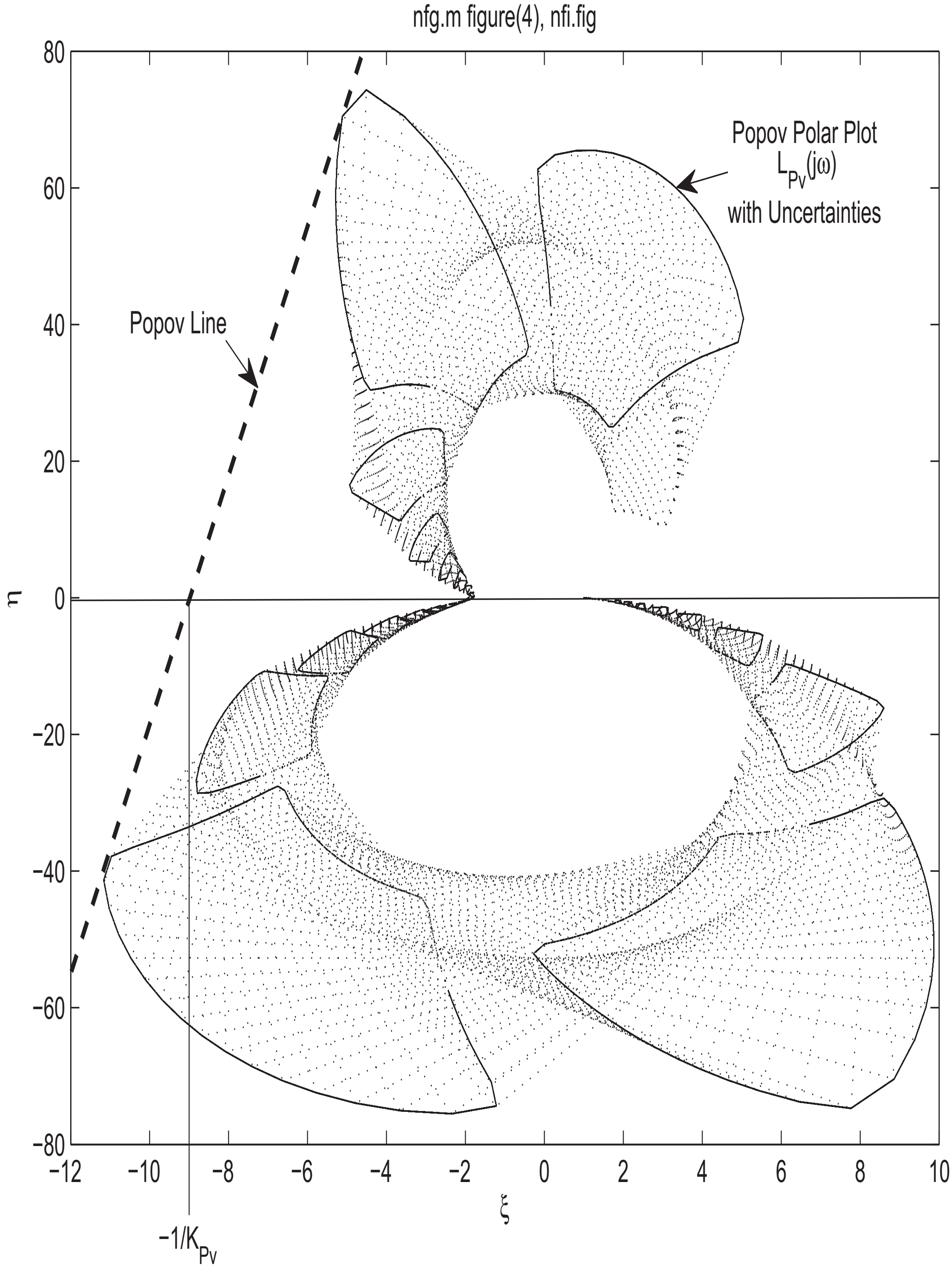

Figure 12: Popov polar plot including uncertainty contours for Example 2

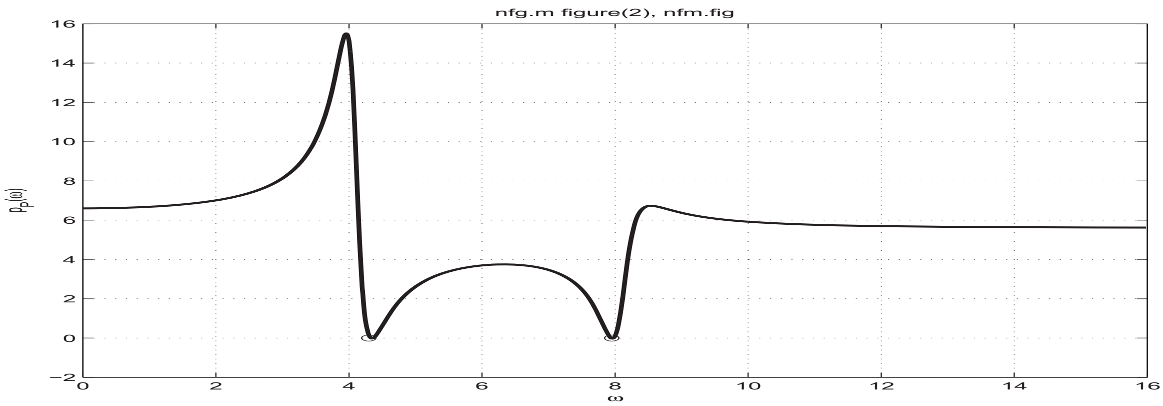

Figure 13: Nominal $p_P(\omega)$ for Example 2

5 Conclusion

The Popov polar plot with envelope-perturbed linear part of the control system is studied. It is suitable for robust absolute stability analysis in order to balance the uncertainty norm and stability requirements. Two examples are selected for extensive illustration.

References

Adamy, J., 2009, Nichtlineare Regelungen, Heidelberg: Springer

Aiserman, M.A., and Gantmacher, F.R., 1965, Die absolute Stabilität von Regelsystemen, München Wien: Oldenbourg

Bhattacharyya, S.P., Datta, A., and Keel, L.H., 2009, Linear control theory, Structure, Robustness, and Optimization, CRC-Press (Taylor and Francis)

Cremer, M., 1995, Regelungstechnik, 2. Auflage, Berlin: Springer

Desoer, C.A., 1965, A generalization of the Popov criterion, *IEEE-Trans.***AC-10**, pp. 182-185

Hsu, J.C., and Meyer, A.U., 1986, Modern control principles and applications, New York: McGraw Hill

Liao Xiaoxin, 1993, Absolute stability of nonlinear control systems, Dordrecht: Kluwer

Popov, V.M., 1973, Hyperstability of control systems, Springer

Föllinger, O., 1993, Nichtlinear Regelungen II, 7. Auflage, München Wien: Oldenbourg

Unbehauen, H., 1983, Regelungstechnik II, Braunschweig: Vieweg

Vidal, P., 1969, Non-linear sampled-data systems, New York: Gordon and Breach

Weinmann, A., Eigenvalue cycles for robust control systems, *e & i, Elektrotechnik und Informationstechnik*, to appear

Weinmann, A., 2010, Stability region robustness, *Cybernetics and Systems* **41**, to appear

Weinmann, A., 2010a, Robust circle criterion based on an uncertainty norm, *Int. J. Automation Austria* **18**, this issue

Robust Circle Criterion Based on an Uncertainty Envelope

Alexander Weinmann, OVE, Senior Member IEEE
Vienna University of Technology, Institute of Automation and Control
Gusshausstrasse 27-29/376, A-1040 Vienna / Austria
Phone: +43 1 58801 37611, Fax: +43 1 58801 37699
email: weinmann@acin.tuwien.ac.at

Manuscript received April 19, 2010

Abstract

Based on a general vector norm of the uncertainties in the linear part of a nonlinear system and the analytic properties of the envelope of the uncertainties, an extension of the Circle Criterion for absolute stability is addressed. In this context, the c-perturbed frequency locus is an appropriate object for the assessment of stability degree. Results of the numerical minimum search and the analytic derivations are presented.

Keywords: Stability degree, robustification, conus margin

1 Introduction

The Circle Criterion is a well-known criterion for the absolute stability with the same assertion as the Popov version. However, there is the advantage that, in contrast to the Popov characteristic, the regular frequency locus of the linear part of the nonlinear control system can be utilized. This is the reason for the broad acceptance in control engineering, even though the stability criterion remains a sufficient one. An additive approach referring to the Circle Theorem is presented in this paper. Unlike the common methods based on interval systems, the uncertainties are considered by means of their envelope and general vector norm bound. Varying an exponential parameter n_r enables the design from deltoid, spherical, up to rectangular of various precision. This type of uncertain systems is termed c-perturbed. Taking a stability degree into consideration (not the stability at all), one is permitted to tolerate a slight violation of the uncertainty bounds. Only if two or more uncertainties should happen to stay at their extreme interval values, the stability falls insignificantly under the limits in the magnitude of neglected high-frequency dynamics. This does not mean that stability at all is violated. The advantage results from the fact that the envelope is an analytic function and can be considered as a walk around the set of uncertain parameters. Due to the analyticity of the uncerainty bound, differentiation is possible even close to the parameter constellations corresponding to the corners of an interval system.

Recalling the Circle Theorem (*Hsu, J.C., and Meyer, A.U., 1986; Liao Xiaoxin, 1993; Föllinger, O., 1993; Unbehauen, H., 1983; Adamy, J., 2009*) one has: For a positive gain sector (e.g., Fig. 1), the circle, termed p_c-circle, must be excluded. For a zero lower bound, the circle tends to infinity and a half-plane must not be entered. For a gain sector in all the quadrants, i.e., the lower bound negative, the gain circle must be excluded, i.e., the polar locus must be located inside the gain circle.

Uncertainties are taken into consideration in most cases by using the plant as an interval system (*Chapellat, H., et al., 1991; Marquez, H.J., and Diduch, C.P., 1994; Bhattacharyya, S.P., et al., 2009*) or after having been transformed from Nyquist to gain plane and using off-axis circles (*Atherton, D.P., and Nusret Tan, 2002*).

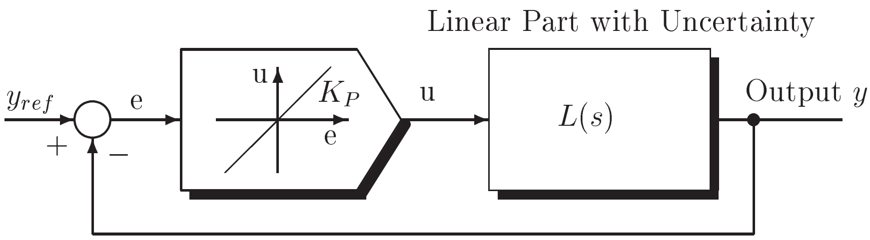

Figure 1: Nonlinear element with a sector-oriented nonlinear characteristic $K_{P1} \leq K_P \leq K_{P2}$ and a linear part of the control system with contour-oriented uncertainty

2 Perturbed Linear System

We consider the system of Fig. 1 with the transfer function $L(s)$ of the linear part. Referring to the presumptive centre of the p_c-circle, a frequential characteristic $L_c(j\omega, p_c)$

of the c-perturbed linear system is defined. Among the set of uncertainties inside the envelope

$$\mathbf{q} \triangleq \begin{pmatrix} \gamma \\ \delta \end{pmatrix}, \quad \|\mathbf{q}\|_r \triangleq (\gamma^{n_r} + \delta^{n_r})^{1/n_r} = q_0 \ , \tag{1}$$

the quantity $\mathbf{q}_s$ yields the shortest distance

$$\arg\min_{\mathbf{q}} |L(j\omega, \mathbf{q}) - p_c|\Big|_{\|\mathbf{q}\|_r = q_0} \triangleq \mathbf{q}_s(\omega) \ . \tag{2}$$

Alternatively, with the uncertainty assumption

$$\mathbf{q} \triangleq \begin{pmatrix} \gamma \\ \delta \end{pmatrix}, \quad \gamma = \gamma_0[1 - (\cos\alpha_c)^{n_r}], \quad \delta = \delta_0[1 - (\sin\alpha_c)^{n_r}], \tag{3}$$

the c-perturbed linear system obeys

$$\arg\min_{c} |L(j\omega, c) - p_c| = \arg\min_{\alpha_c} | \underbrace{L[j\omega, c(\alpha_c)] - p_c}_{h(\alpha_c)} | \triangleq \alpha_c^\star \tag{4}$$

$$h(\alpha_c^\star) \triangleq L_c(j\omega, p_c) \ . \tag{5}$$

The absolute value of the complex-valued distance is

$$L_f(\omega) \triangleq |L_c(j\omega) - p_c| \tag{6}$$

and the minimum distance itself

$$f \triangleq \inf_{\omega} L_f(\omega) \ , \tag{7}$$

see Fig. 2. The parameter f corresponds to a robust conus margin.

Referring to the sector (K_{P1}, K_{P2}), where $K_{P1} \leq K_{P2}$, and the well-known correspondences

$$-\frac{1}{K_{P1}} = p_c - f \quad , \quad -\frac{1}{K_{P2}} = p_c + f \quad , \tag{8}$$

one has

$$K_{P2} - K_{P1} = \frac{2f}{p_c^2 - f^2} \tag{9}$$

and a tradeoff between the slope sector and the upper or lower extreme slope. In order to obtain a large sector, i.e., K_1 large and K_2 small, one should try to provide $f \to \max$.

3 Satifying the Conditions and Robustification

Based on MATLAB `fmincon`, $L_c(j\omega, p_c)$ of Eq.(5) is determined. The result is depicted in Fig. 2. In parallel, the c-envelope $c(\mathbf{q})$ of the uncertainties is shown.

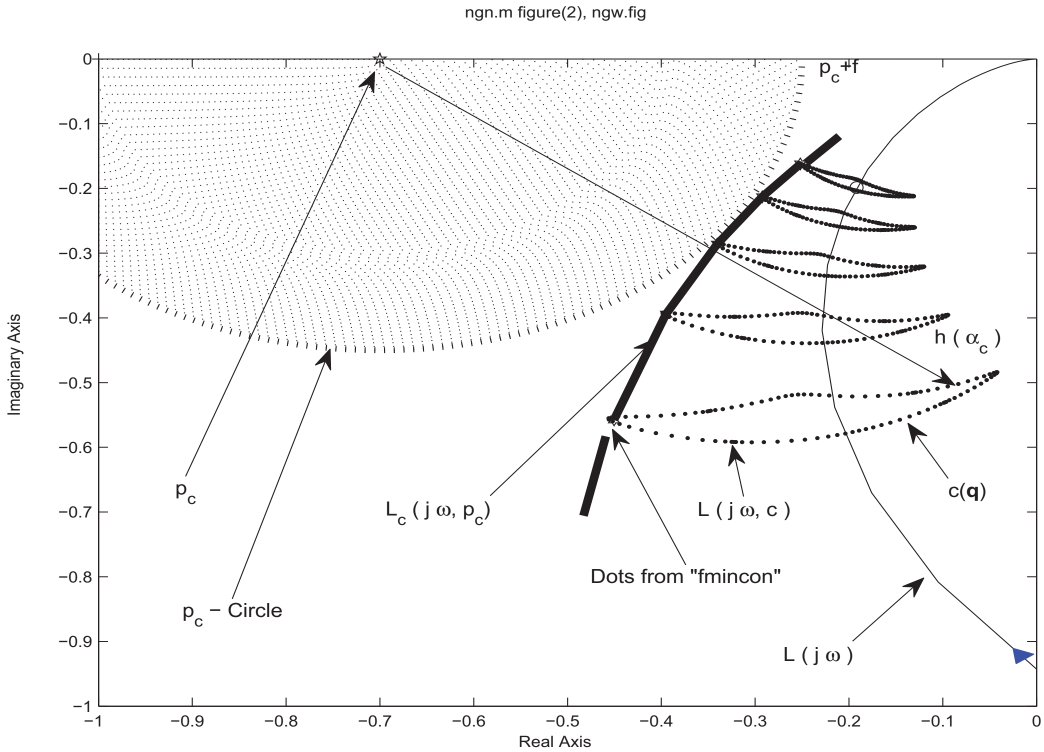

Figure 2: $L_c(j\omega, p_c)$ and c-envelopes (Example 1 with $p_c = -0.7;\ f = 0.24$)

If there are two (or more) uncertainty groups, referring, e.g., to pressure, temperature etc., these groups are not concatenated. Then, in each group an uncertainty can arrive at an extreme value. For groups of uncertainties, they are considered by separate Lagrange multipliers μ_k. One has to state a resulting function

$$|L(j\omega, \mathbf{q}_k) - p_c| + \sum_k \mu_k[\|\mathbf{q}_k\|_r - q_{0k}] \ \rightarrow\ \min_{\mathbf{q}_k} \tag{10}$$

and to follow MATLAB

```
solve('fun', mu_init)
function [f1,f1,f3]=fun(mu)
     f1=\| \q_1 \|_r-q_{0 1};
     f2=\| \q_2 \|_r-q_{0 2};
     f3=\| \q_3 \|_r-q_{0 3};
```

The robust p_c-based conus margin c_R is defined as

$$c_R \triangleq \|\frac{1}{L_c(j\omega, p_c)}\|_\infty = \|[L_c(j\omega, p_c)]^{-1}\|_\infty = \sup_\omega \frac{1}{L_f(\omega)} = \frac{1}{f}, \tag{11}$$

see Fig. 6.

Robustification can be achieved as follows: For a given cone $K_{P2} - K_{P1}$, i.e., given p_c-circle, varying a linear system parameter a, preferably a controller parameter, leads to the maximum q_0. Alternatively, by varying a the maximum gain sector can be obtained (see Fig. 10 in Example 1).

4 Example 1. Linear IT$_{3s}$-System

The Example 1 of *Weinmann, A., 2010,* is repeated based on the circle theorem,

$$L(s) = \frac{1}{s(s+a)(1+\dfrac{2D}{\omega_N}s+\dfrac{1}{\omega_N^2}s^2)} \tag{12}$$

with $n_r = 8$; $D = 0.045$; $a = 1.05$; $\omega_N = 4.1$; $p_c = -0.8$.

The parameters a and D perturbed by $\beta_a\gamma$, $\beta_d\delta$, where $\beta_a = 0.1$, $\beta_d = 0.015$. The minimum distance in Fig. 3 is $f = 0.2890$ at $\omega_s = 3.91$.

The Fig. 3 depicts the uncertainty envelope coordinates. In Figs. 4 and 5, the c-perturbed characteristic $L_c(j\omega, p_c)$ and the p_c-circle are shown. For better distinctness and in order to put emphasis on this graph, the c-perturbed graph $L_c(j\omega, p_c)$ is exclusively presented in Fig. 5, omitting the c-envelopes. The inverse of L_f is given in Fig. 6.

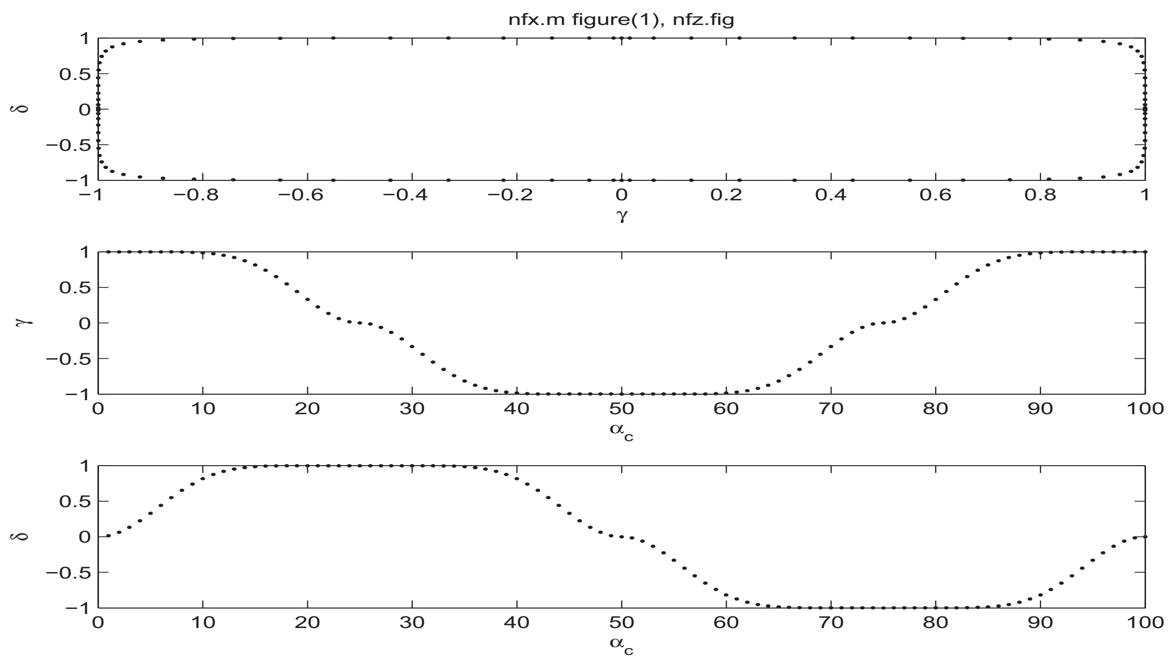

Figure 3: Uncertainty in 100 points

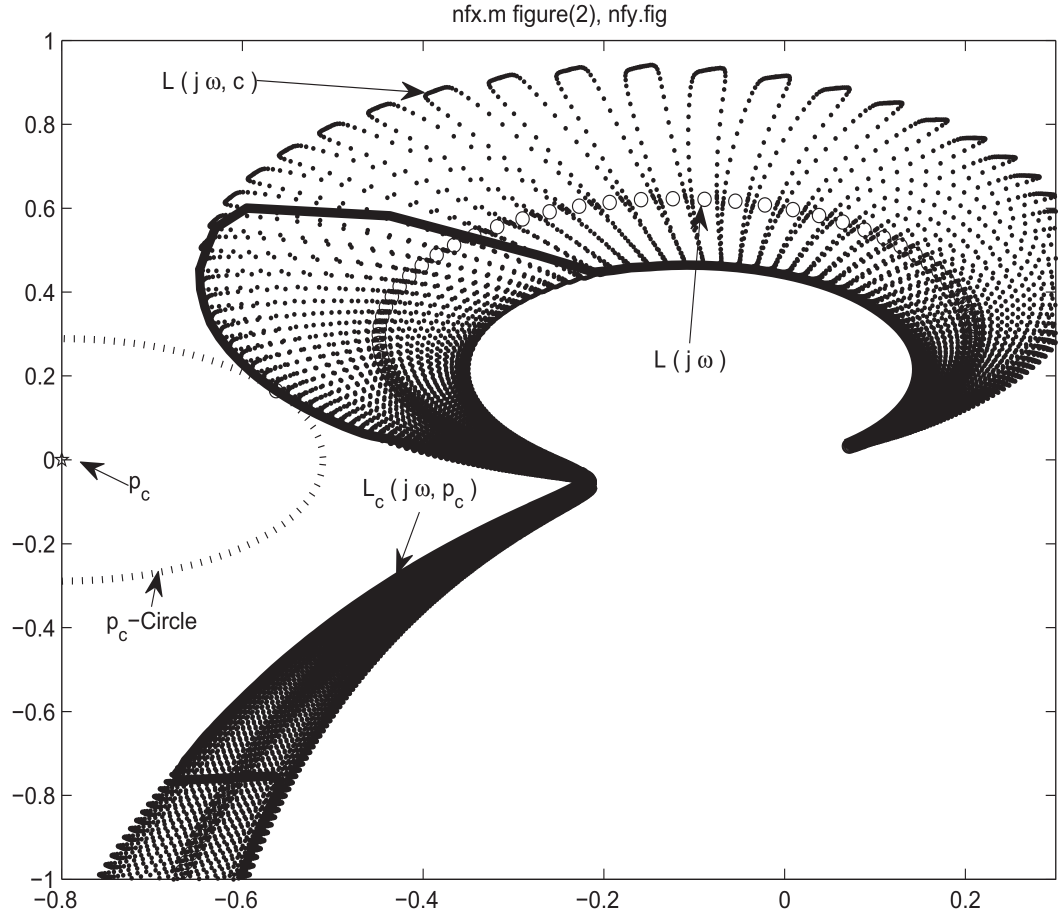

Figure 4: Characteristic $L(j\omega, c)$ and perturbed characteristic $L_c(\omega, p_c)$ and p_c-circle

Fig. 7 shows a set of eight p_c-circles for $p_c = \{-0.4, -1.1\}$. In Fig. 8 the admissible cone $(K_{P2} - K_{P1})$ is depicted.

Consider the parameter a as the controller parameter. Varying a causes a change in touching the p_c-circle. In Fig. 9, small a leads to the minimum f at low frequencies close to 1, large a are responsible for the minimum close to frequency 4. For $a = 0.68$ the extrema are equal. This parameter represents the optimally robustified system, see Fig. 10.

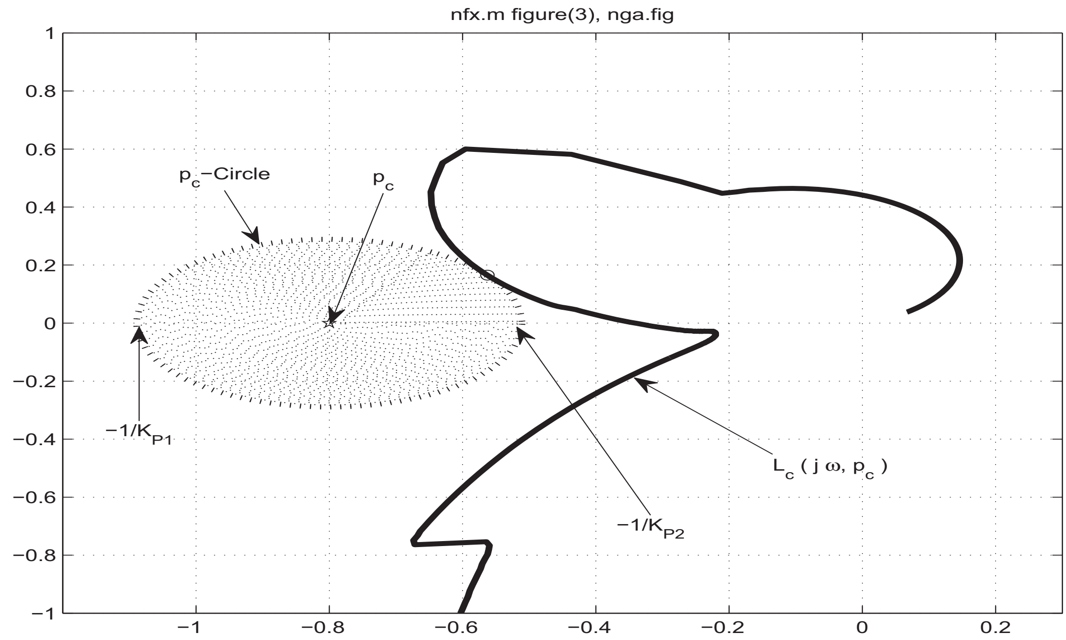

Figure 5: Perturbed characteristic $L_c(j\omega, p_c)$ and p_c-circle

Figure 6: Inverse $L_f(\omega)$ and robust conus margin c_R equal to the peak height $1/f$

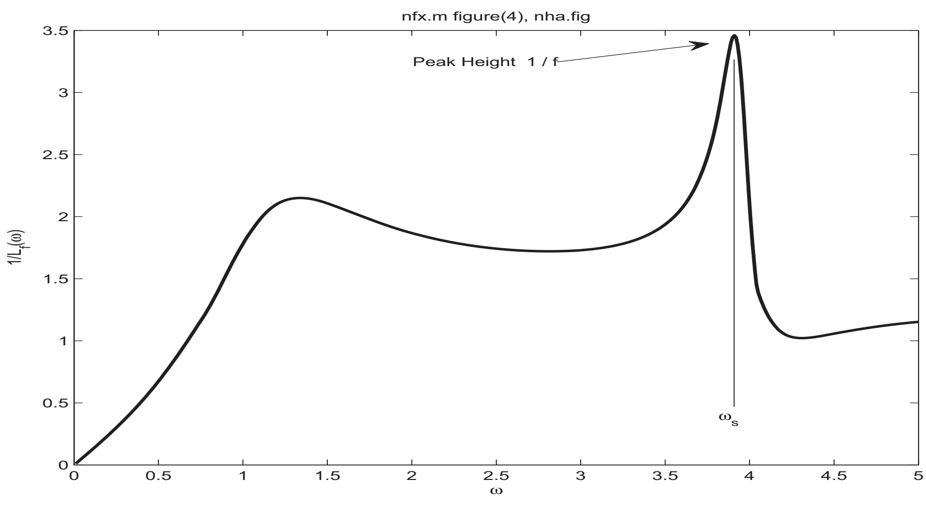

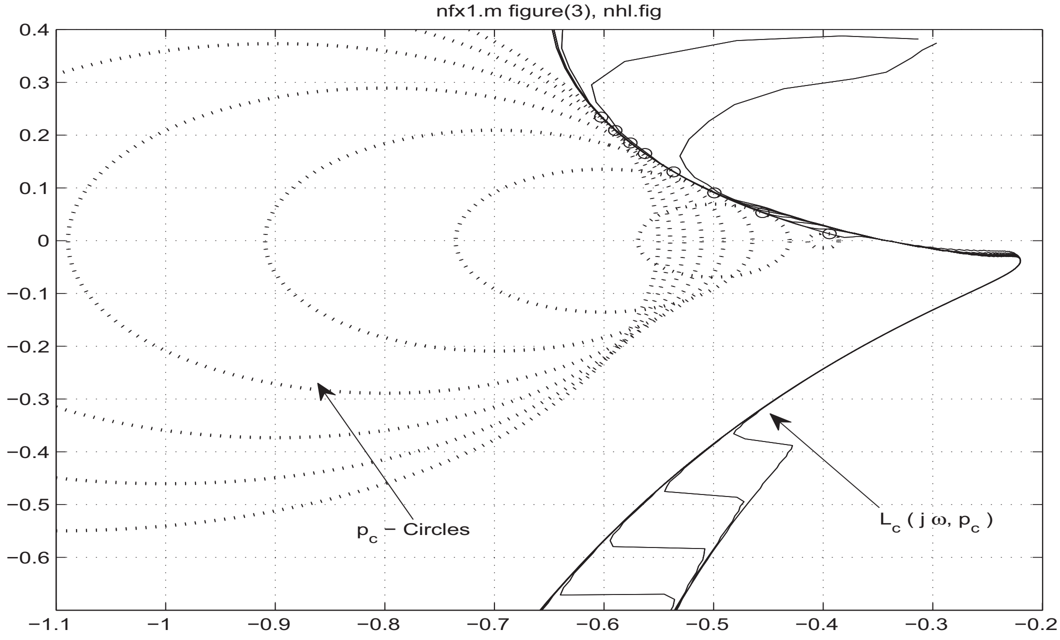

Figure 7: Set of eight p_c-circles for $p_c = \{-0.4, -1.1\}$

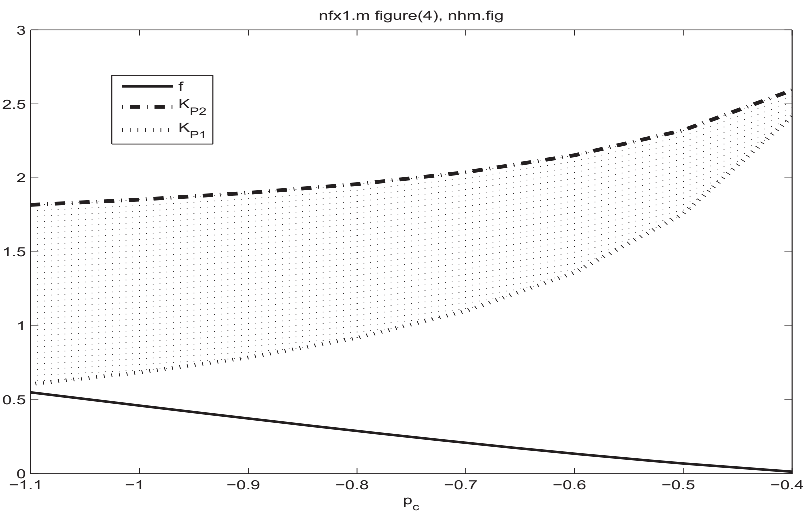

Figure 8: Admissible slope sector $(K_{P2} - K_{P1})$

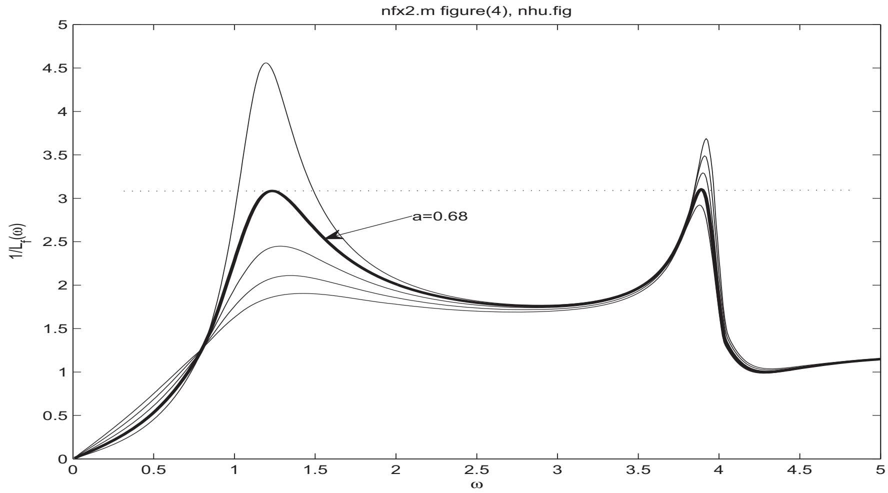

Figure 9: Inverse L_f versus ω

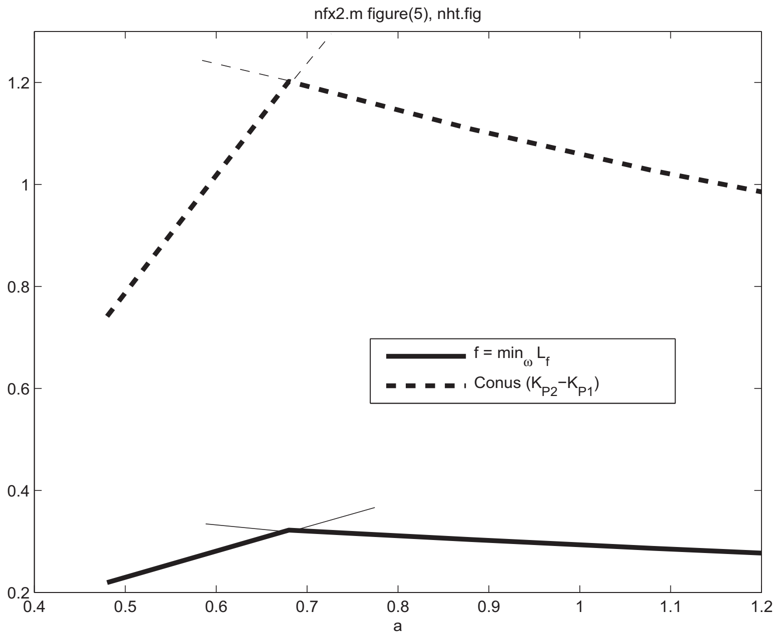

Figure 10: Influence of the controller paramter a on robustifying the control system

5 Example 2. Linear System with Conditioned Stability

The transfer function set up of the linear part is

$$L(s) = V\frac{-0.2s^3 + 1.14s^2 - 1.62s + 0.9}{0.1s^4 + s^3 - 1.2s^2 + 9s} \tag{13}$$

with poles and zeros at $\{0; -11.6859; 0.8430 \pm 2.6440j\}$ and $\{3.9305; 0.8848 \pm 0.6017j\}$, respectively.

For $V = 4$, the linear closed-loop system poles are located at $\{-0.6228 \pm 5.5794j; -0.3772 \pm 1.0000j\}$. Hurwitz stability is given for the following supplemental factors of $V = 4$: approximately from 1/1.9=0.52 to 1/0.7=1.41 (see Fig. 12).

The parameter -1.62 in the numerator of Eq.(13) is perturbed by $\beta_a\gamma$ and the parameter 9 in the denominator by $\beta_d\delta$, where $\beta_a = 0.2; \beta_D = 0.4; p_c = -1.4$.

The Hurwitz based stability sector is 0.52 to 1.41. Following the circle theorem without uncertainty, the stability sector is $K_{P1} = 0.59$ to $K_{P2} = 0.9$, slightly smaller than the Hurwith sector. The stability range result with uncertainty, i.e., the admissible sector for the perturbed system, is $K_{P1} = 0.6204$ to $K_{P2} = 0.8417$ (see Fig. 12). The minimum distance is $f = 0.2119$ at $\omega_s = 4.01$.

Figure 11: Root locus for $L(s) = V\frac{-0.2s^3+1.14s^2-1.62s+0.9}{0.1s^4+s^3-1.2s^2+9s}$

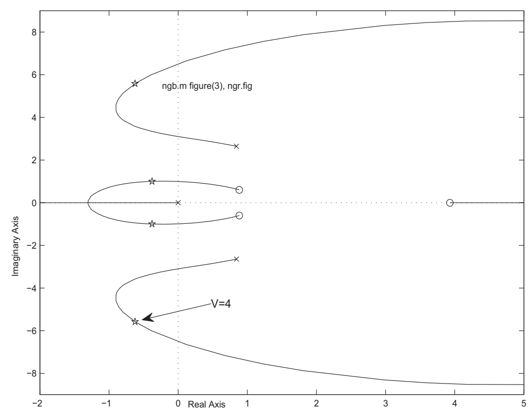

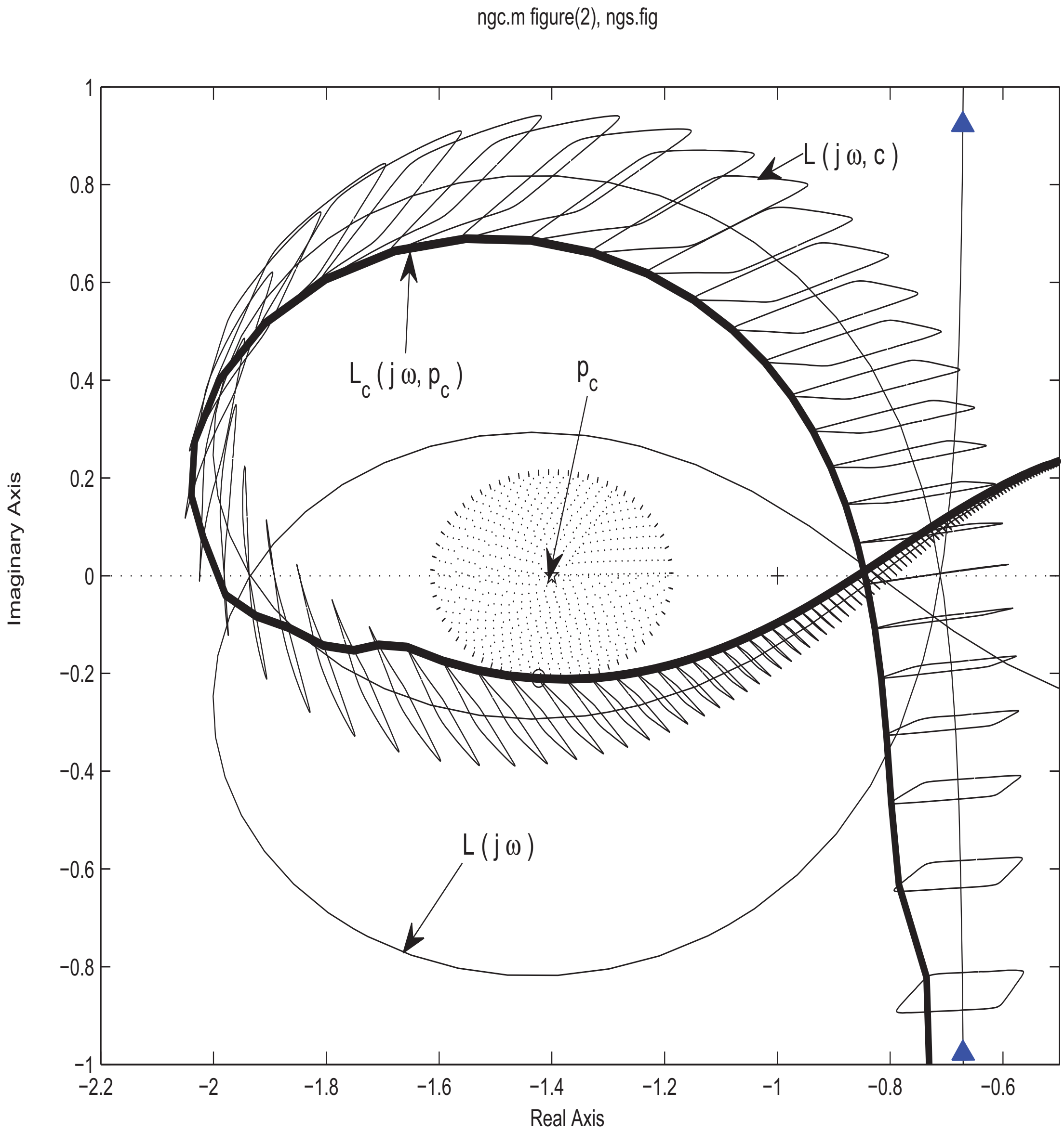

Figure 12: Frequency response polar plot for $V = 4$ with uncertainty and $n_r = 8$

6 Example 3. Linear PT_2-System

The linear part is

$$L(s) = \frac{10^5}{(s+a)(s+b)}. \tag{14}$$

The parameters a and b are perturbed by $\beta_a\gamma$ and $\beta_d\delta$, respectively. The set up is $a = 500$; $b = 300$; $n_r = 8$; $\beta_a = 70$; $\beta_e = 60$; $p_c = 0.4$.

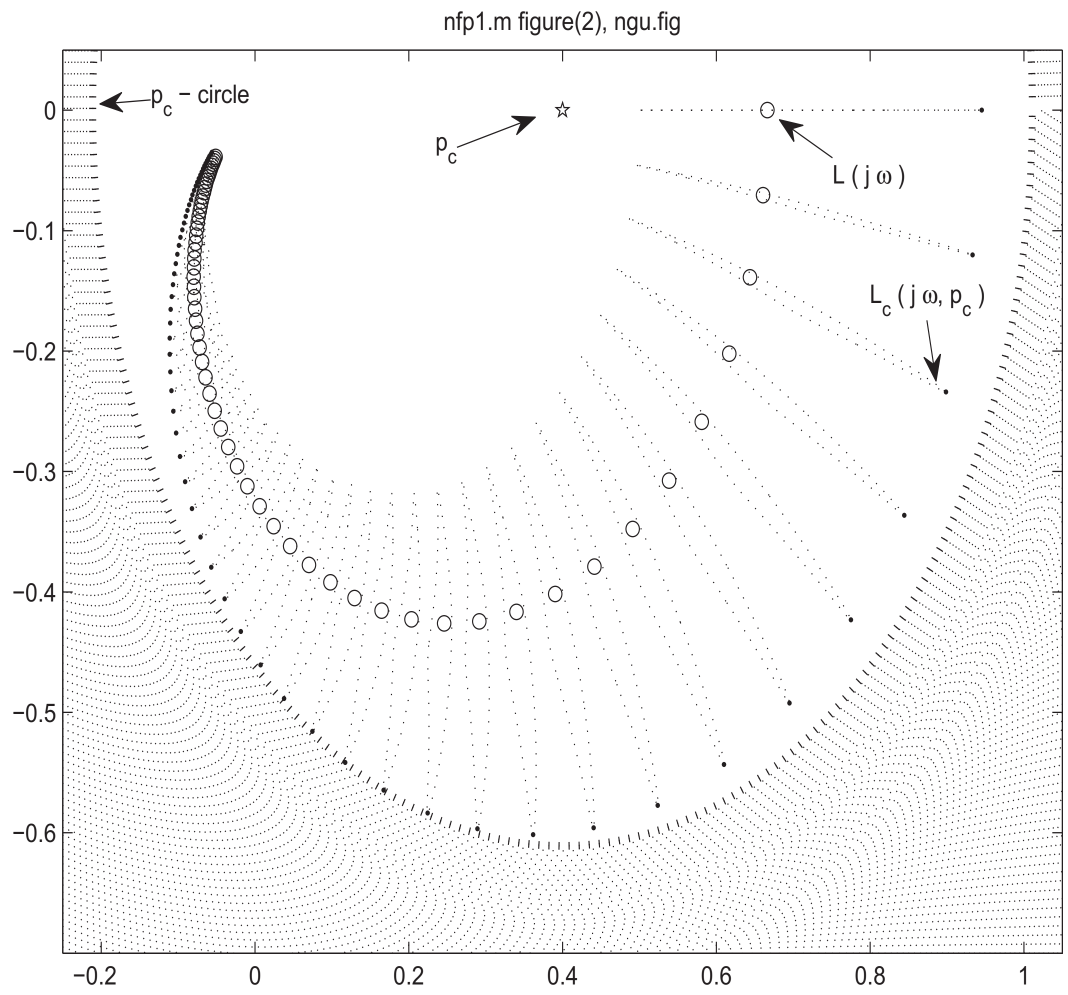

Figure 13: Polar loci for Example 3

From Fig. 13 one finds the p_c-circle radius $f = 0.6109$; $\omega_s = 260$; $L_c(j\omega_s, p_c) = 0.117 - j0.542$; $K_{P2} = 4.7412$; $K_{P1} = -0.9892$.

7 Example 4. Linear PT_1-System and Algebraic Differentiation

Consider a PT_1 linear part of the control system and its perturbations

$$L(s) = \frac{(V+\gamma)}{s+(b+\delta)} \ , \quad |\gamma| \leq 1, \quad |\delta| \leq 1 \ , \tag{15}$$

where

$$\gamma \triangleq 1 - (\cos\alpha_c)^{n_r} \quad 0 \leq \gamma \leq 1 \tag{16}$$
$$\delta \triangleq 1 - (\sin\alpha_c)^{n_r} \quad 0 \leq \delta \leq 1 \ . \tag{17}$$

Referring to Eq.(4) and Fig. 2,

$$|h(\alpha_c)|^2 = (\Re e\ [L(j\omega) - p_c])^2 + (\Im m\ [L(j\omega)])^2 \ . \tag{18}$$

Numerical data are $V = 18;\ b = 2;\ p_c = -0.97;\ \omega = 4$.

Even though this is a very simple example, the function $|h(\alpha_c)|^2$ is characterized by several in-between-extrema and points of inflection; thus, the derivative $\frac{\partial |h(\alpha_c)|^2}{\partial \alpha_c}$ has a curious shape, see Figs. 15, 17, 19.

For three different $n_r = \{4,\ 8\ 16\}$, typical shapes are shown in the sequel.

Several different and appropriate initial values are required for solving $\frac{\partial |h(\alpha_c)|^2}{\partial \alpha_c} = 0$.

For negative values of $\gamma,\ \delta$, see Eq.(19). Finally, the details of h^2 and $\frac{\partial h^2}{\partial \alpha_c}$ are displayed.

The flags $u,\ v,\ x,\ y$ are ± 1 factors in order to achieve an monotonous display of the uncertainties $\gamma,\ \delta$ versus α_c. The function is analytic and differentiable whenever needed

$$\gamma = u - x(\cos\alpha_c)^{n_r}, \qquad \delta = v - y(\sin\alpha_c)^{n_r}. \tag{19}$$

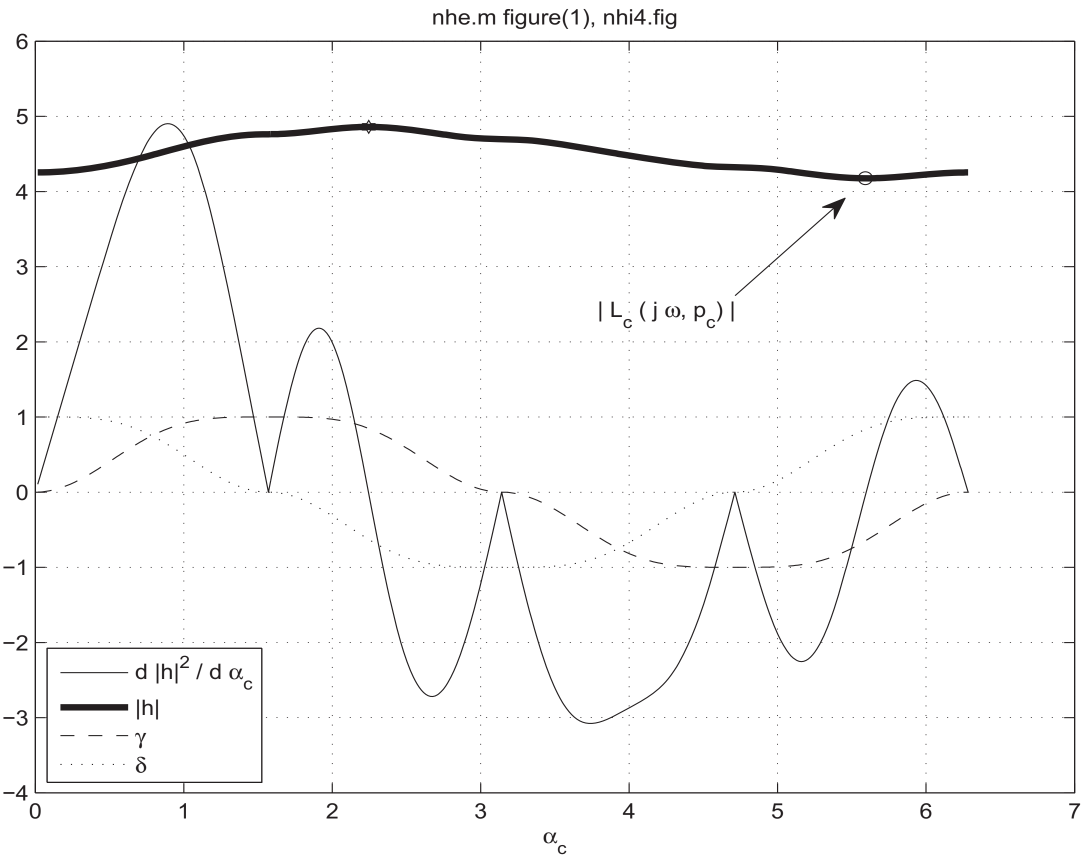

Figure 14: Envelope distance $|h(\alpha_c)|$ and the derivative of its square with respect to α_c for $\omega = 4 =$ constant and $n_r = 4$

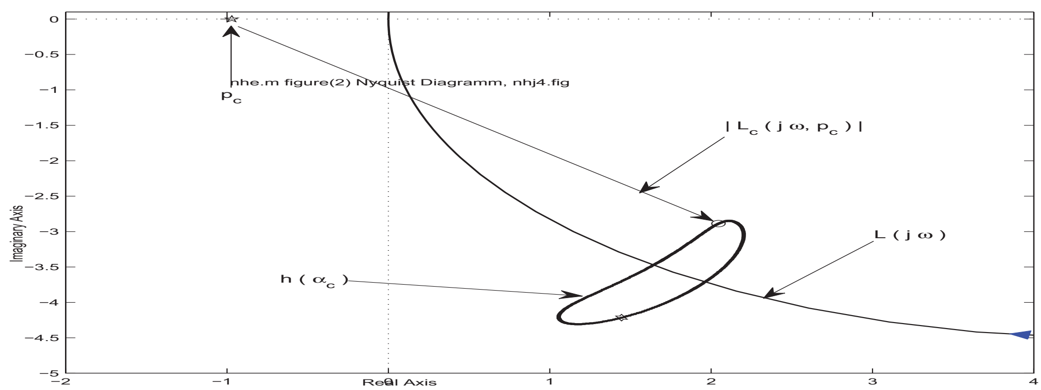

Figure 15: Corresponding Nyqist diagramm and uncertainty walk for $n_r = 4$

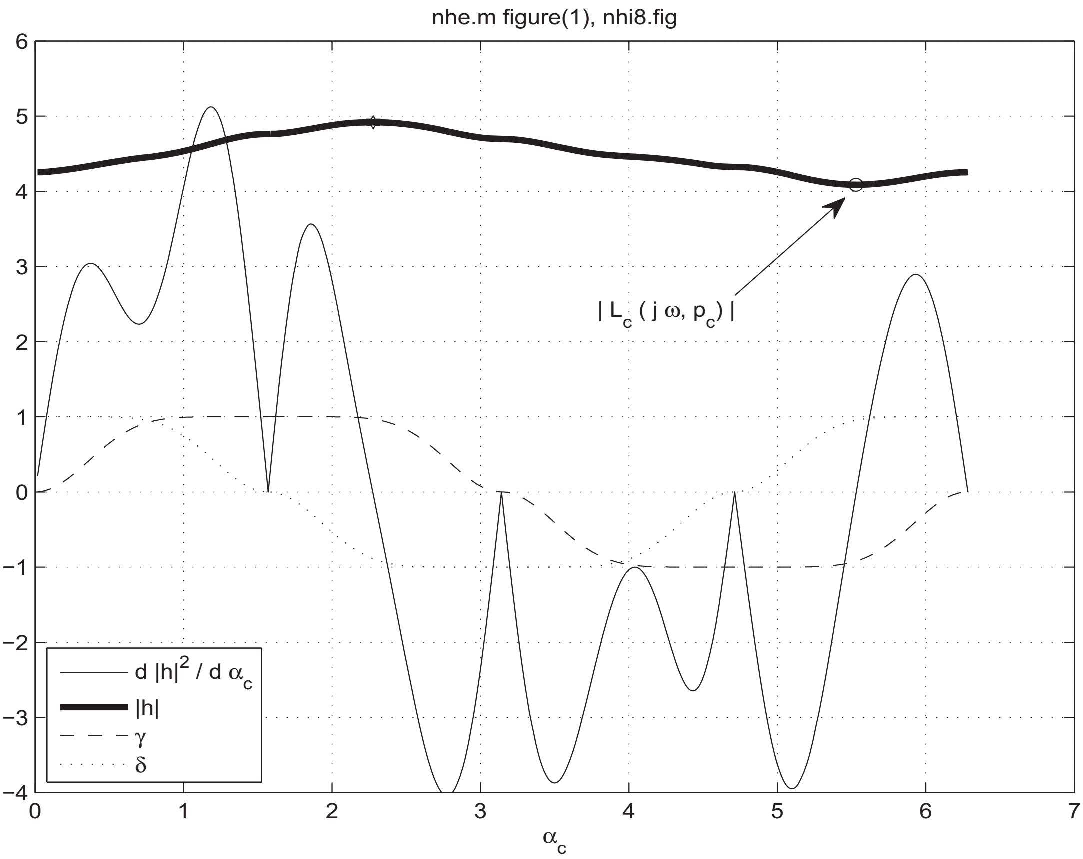

Figure 16: Envelope distance $|h(\alpha_c)|$ and the derivative of its square with respect to α_c for $\omega = 4 =$ constant and for $n_r = 8$

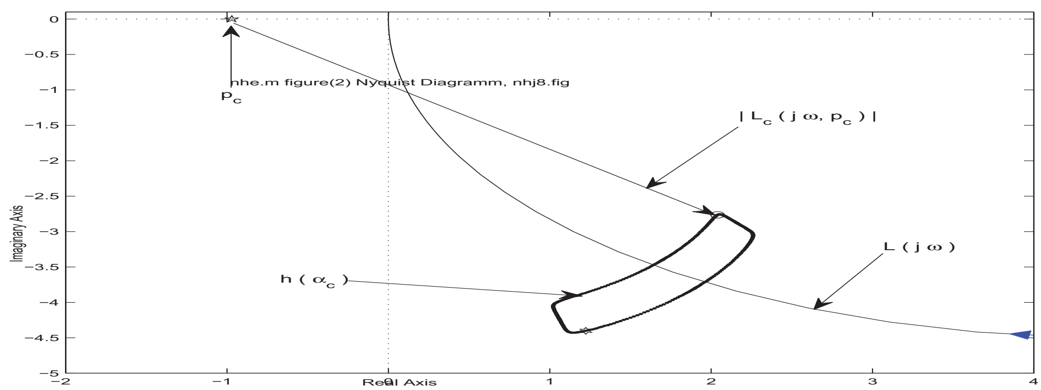

Figure 17: Corresponding Nyqist diagramm and uncertainty walk for $n_r = 8$

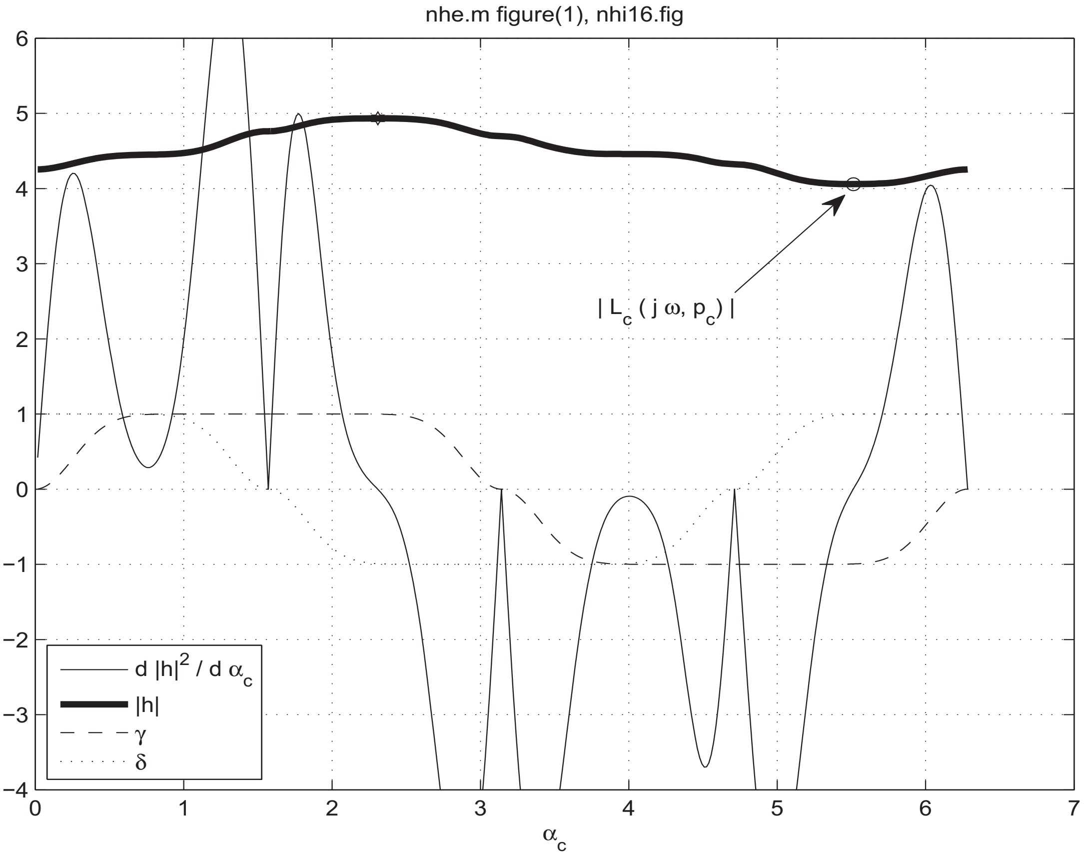

Figure 18: Envelope distance $|h(\alpha_c)|$ and the derivative of its square with respect to α_c for $\omega = 4 =$ constant and $n_r = 16$

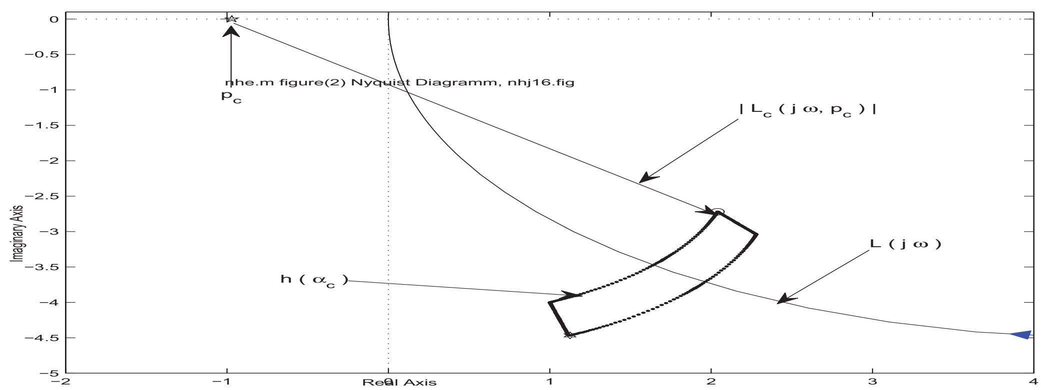

Figure 19: Corresponding Nyqist diagramm and uncertainty walk for $n_r = 16$

```
|h|^2 [== t3] =
(pc - ((V + u - x*cos(alphac)^nr)*(b + v - y*sin(alphac)^nr))
/((b + v - y*sin(alphac)^nr)^2 + om^2))^2
+ (om^2*(V + u - x*cos(alphac)^nr)^2)/((b + v - y*sin(alphac)^nr)^2 + om^2)^2

d |h|^2/d alphac [== t5 == g] =
(2*nr*om^2*x*cos(alphac)^(nr - 1)*sin(alphac)*(V + u - x*cos(alphac)^nr))
/((b + v - y*sin(alphac)^nr)^2 + om^2)^2
- 2*(pc - ((V + u - x*cos(alphac)^nr)*(b + v - y*sin(alphac)^nr))
/((b + v - y*sin(alphac)^nr)^2 + om^2))
*((nr*x*cos(alphac)^(nr - 1)*sin(alphac)*(b + v - y*sin(alphac)^nr))
/((b + v - y*sin(alphac)^nr)^2 + om^2)
- (nr*y*cos(alphac)*sin(alphac)^(nr - 1)*(V + u - x*cos(alphac)^nr))
/((b + v - y*sin(alphac)^nr)^2 + om^2)
+ (2*nr*y*cos(alphac)*sin(alphac)^(nr - 1)*(V + u - x*cos(alphac)^nr)
*(b + v - y*sin(alphac)^nr)^2) /((b + v - y*sin(alphac)^nr)^2 + om^2)^2)
+ (4*nr*om^2*y*cos(alphac)*sin(alphac)^(nr - 1)*(V + u - x*cos(alphac)^nr)^2
*(b + v - y*sin(alphac)^nr)) /((b + v - y*sin(alphac)^nr)^2 + om^2)^3
```

8 Conclusion

The c-perturbed frequency polar plot and the robust conus margin have been introduced. They are suitable measures for absolute stability discussion. Algebraic differentiation for the uncertainty envelope was carried out in detail. The c-perturbed frequency polar plot itself can also be used to determine the robust stability of the linear system with c-envelope perturbation. Four comprehensive examples are chosen for illustrating the results.

References

Adamy, J., 2009, Nichtlineare Regelungen, Heidelberg: Springer

Atherton, D.P., and Nusret Tan, 2002, The absolute stability of uncertaint nonlinear systems using new formulations of the circle criteria, *Proc. 41st IEEE CDC,* pp. 2284-2285

Bhattacharyya, S.P., Datta, A., and Keel, L.H., 2009, Linear control theory, Structure, Robustness, and Optimization, CRC-Press (Taylor and Francis)

Chapellat, H., Dahleh, M., and Bhattacharyya, S.P., 1991, On robust nonlinear stability of interval control systems, *IEEE-Trans.* **AC-36**, pp. 59-67

Cremer, M., 1995, Regelungstechnik, 2. Auflage, Berlin: Springer

Hsu, J.C., and Meyer, A.U., 1986, Modern control principles and applications, McGraw Hill

Marquez, H.J., and Diduch, C.P., 1994, Absolute stability of systems with parametric uncertainty and nonlinear feedback, *IEEE-Trans.* **AC-39**, pp. 664-668

Weinmann, A., 2010, Popov stability under uncertainty contours, *Int. J. Automation Austria* **18**, this issue

Report IFAC Workshop Supplemental Ways for Improving International Stability Bucharest, Romania October 28 – 30, 2009

Supplemental Ways for Improving International Stability - SWIIS - has a long tradition in IFAC. According to the triennial cycle after Prishtina (Kosovo) 2006 the Workshop was organised this year by the Faculty of "Control and Computers" of the "University Politechnica of Bucharest" from October 28 to 30, 2009 in Bucharest, Romania.

The program included 3 plenary papers, 18 technical papers and 2 panel discussions. The plenary papers dealt with a new approach for simulation of sociotechnical systems, international stability issues and globalisation. According to the scope of SWIIS the topics of the technical papers were heterogenous. One block of papers dealt with complex - adaptive - systems. Such systems are more and more introduced not only for modelling and control of socioeconomic systems. Another session was about software piracy, existing laws and the impact to economy. Cooperative networks offer the possibility to design an umbrella for different applications. Further topics adressed were fuzzy methods, ethics in IT, collaborative software platforms, …….

The two survey papers by F. Kile "Improving Policy Choices through Simulation" and G. Dimirovski " International Stability Issues: Individual vs. Collaborative behaviours in Complex Dynamical Networks by Controlled Synchronisation" gave an excellent overview on these subjects.

In the panel discussion " Impact of the crisis on Social Stability" was mentioned that in terms of SWIIS the problem could be seen as a stability problem of a very complex system. To solve this problem new theoretical approaches are necessary. The other panel discussion "Education and Research in a Global Society" was naturally concentrated to Universities.
42 participants attended the very well organised event.

The next Workshop will take place in Prishtina, Kosovo, October 27 – 29, 2010 and is organised by the local IFAC NMO.

P. Kopacek

Kooperationsworkshop über menschenähnliche Roboter

TU Wien, 26 Jänner 2010

Im Rahmen der Kooperationsabkommen der TU Wien mit der University of Manitoba (Kanada) und der National Kaohsiung First University of Science and Technology (NKFUST),Taiwan, R.O.C, fand am 26. Jänner 2010 an der TU Wien eines der ersten internationalen, wissenschaftlichen Workshops über humanoide Roboter in Österreich statt.

Wie in der, vor kurzen fertiggstellten, BMVIT Studie „ Robtics in Austria“ ausgeführt liegen in Österreich, von der theoretischen Seite, Potenziale brach welche unmittelbar auf diese moderne Technologie angewandt werden können. Hauptzweck dieser Veranstaltung war es daher österreichischen Universitäts- und Forschungsinstituten sowie der einschlägigen Industrie einen tieferen Einblick in die theoretischen Hintergründe dieses rapid wachsenden Marktes zu geben. Der Schwerpunkt lag dabei auf, menschenähnlichen, intelligenten, mobilen Robotern sowie auf dreidimensionalen „ Sehen“.

P. Kopacek berichtete über den Stand der Robotertechnik in Österreich und ergänzte seine Ausführungen. durch Beispiele ausgeführter Projekte. Sodann stellten B. McKinnon, J. Baltes und J. Anderson von der Universität Manitoba ein neues Verfahren für dreidimensionales Sehen basierend auf der Liniensegmenterkennung vor. Fuzzy Methoden haben an der NKFUST eine lange Tradition. K.Y. Tu beschäftigte sich in seinem Vortrag mit der Anwendung dieser Methode zum „Robusten Gehen“ humanoider Roboter. Anschließend gab P. Kopacek einen Überblick über Forschungsarbeiten auf dem Gebiet der autonomen, mobilen Roboter an der TU Wien. Wettkämpfe humanoider Roboter werden immer beliebter. J. Baltes und J. Anderson gaben daher im nächsten Vortrag einen Überblick über diese „Sportdisziplinen“. Ein neuer an der NKFUST entwickelter Roboter (NeiDau) mit Kraft- und Momenten Sensoren wurde von K. Y Tu vorgestellt. Über das Gemeinschaftsprojekt „Humanioder Roboter Archie“ referierten J. Baltes und P. Kopacek. Den Abschluss bildete ein Vortrag von Y. T. Yang von der Tamkang Universität in Taiwan über das emotionelle Verhalten von Spielzeugrobotern.

Laut übereinstimmender Meinung der ungefähr 50 Teilnehmer erfüllte diese Veranstaltung ihren Zweck einen Einblick in Arbeiten aus Österreich, Kanada und Taiwan zu geben um zukünftige, kooperative Forschungsprojekte zu initialisieren. und der Roboterforschung in Österreich weitere Impulse zu verleihen.

Die Bedeutung der Veranstaltung wurde dadurch unterstrichen, daß diese vom Botschafter Taiwans, dem Handelsrat Kanadas und seitens der TU Wien, von Vizerektor H. Kaiser eröffnet wurde.

P.Kopacek

Bausteine mechatronischer Systeme

W. Bolton

3. Auflage, Pearson Studium, 2006
ISBN 3-8273-7098-1

Die Integration der verschiedenen Ingenieurwissenschaften in Studium und Beruf wird immer wichtiger. Dieses interdisziplinär ausgerichtete Lehrbuch zu den Bausteinen mechatronischer Systeme vermittelt daher die wichtigsten Kenntnisse aus der Elektrotechnik, des Maschinenbaus und der Informatik, um mechatronische Systeme in der Theorie und in der späteren Berufspraxis zu verstehen.
Der Leser lernt an vielen Beispielen mit Übungsaufgaben und Lösungen, wie sich die Verzahnung der Teilgebiete in der Mechatronik gestaltet. Zugleich ermöglicht dieser Blick über den Tellerrand, dass Mechatronik-Studenten mit Kollegen aus den anderen Fachgebieten problemlos kommunizieren können. Diese ganzheitliche Sichtweise hilft Studierenden, mechatronische Systeme, wie sie in der Industriepraxis üblich sind, zu verstehen und eigenständig zu entwerfen. Es werden sowohl grundlegende Systemelemente, Antriebssysteme, Systemmodelle, Microprozessorsysteme behandelt. Den Abschluss bilden zeitgemäße Beispiele mechatronischer Systeme

Das Buch kann sowohl Studenten der Ingenieurwissenschaften als auch den in der Praxis stehenden wärmstens empfohlen werden.

P. Kopacek

Moderne Regelungssysteme

Richard C. Dorf und Robert H. Bishop,

10. überarbeitete Auflage, Pearson Studium, 2007
ISBN 3-8273-7162-7

Einer der Klassiker unter den Lehrbüchern über Einführung in die Regelungstechnik liegt nun in der 10. überarbeiteten deutschen Auflage vor. Wie bereits die vorghehenden englischen und deutschen Auflagen bietet es den Lesern in anschaulicher Form einen ersten Einblick in die moderne Regelungstechnik. Dies wird dadurch erreicht, dass die Verfahren und Methoden durch anschauliche Beispiele erläutert werden. Dadurch erkennt der Leser sehr schnell die kaum überschaubare Vielfalt moderner regelungstechnischer Anwendungen, wodurch sein Interesse am Fach Regelungstechnik geweckt wird.

Ziel des Buches ist es, die Grundlagen des Entwurfs von Regelungssystemen im Zeit- und Frequenzbereich in klarer und anschaulicher Weise darzustellen. Der Bogen erstreckt sich dabei über Verfahren der klassischen Regelungstechnik bis hin zu Zustandsraumverfahren. Darüber hinaus werden auch die neuesten Entwicklungen der Regelungstechnik, wie beispielsweise robuste Regelungssysteme, Anwendung computerunterstützter digitaler Regelungssysteme, … behandelt. Am Ende jedes Kapitels befindet sich ein Abschnitt über MAT-LAB in dem der Lernende mit den Grundlagen der rechnergestützen Synthese und Analyse von Regelungssystemen vertraut gemacht werden soll.

Das Buch kann sowohl Studenten der Ingenieurwissenschaften als auch den in der Praxis stehenden wärmstens empfohlen werden.

P. Kopacek

Instruction to authors – presented as a pattern paper (18 pt)

A. Maier, F. Huber (12 pt)
Department ....., Vienna, Austria

Received April 8, 1999

Abstract
This paper shows …… (italics, 12 pt)

1 General (14 pt)

Authors should prepare their manuscript camera ready, format A 4, 12 typeface and must present their manuscript in good quality. At the left/right edge 2.5 cm, at the to/bottom edge 3 cm. Authors are invited to use papers of this journal as a sample. Please do not use an eraser or erasing fluid. Footnotes should be avoided if possible. Authors are expected to submit their paper to one of the publishers (O.Univ.Prof.Dr. Peter Kopacek, Intelligent Handling Devices and Robotics, Vienna University of Technology, Favoritenstrasse 9-11, A-1040 Vienna, Austria, Fax: +43 1 58801-31899 or O.Univ.Prof.Dr. Alexander Weinmann, Institute of Automation and Control, Vienna University of Technology, Gusshausstr. 27-29, A-1040 Vienna, Austria, Fax: +43 1 58801 37699).

Email address for submitting pdf-manuscripts: weinmann@acin.tuwien.ac.at

2 References (14 pt)

Within the paper references should appear in the following form:
(Mayer, H., 1990) or (*Mayer, H., 1990)* (12 pt);
Mayer, H., 1990, discovered that....

3 Figures and Tables (14 pt)

Figures and Tables should be integrated in the paper and have to be referred to as Fig. 4.1 or Tab. 5.2.

4 References

References are to be listed alphabetically according to first author. (11 pt)

5 Word Processing System/Editor

Microsoft Word for Windows 1.1 or higher; Microsoft Word 5.0; TeX or LaTeX.

Wenn unzustellbar, retour an:

IFAC-Beirat Österreich (E318 / E376)
Favoritenstraße 9-11, A-1040 Wien /
Gußhausstraße 27-29, A-1040 Wien